

A controlled one and two atom-cavity system

Dissertation

zur

Erlangung des Doktorgrades (Dr. rer. nat.)

der

Mathematisch-Naturwissenschaftlichen Fakultät

der

Rheinischen Friedrich-Wilhelms-Universität Bonn

vorgelegt von

Mkrtych Khudaverdyan

aus

Moscow (Russia)

Bonn 2009

Angefertigt mit Genehmigung der Mathematisch-Naturwissenschaftlichen Fakultät
der Rheinischen Friedrich-Wilhelms-Universität Bonn

1. Referent: Prof. Dr. Dieter Meschede
2. Referent: Prof. Dr. Martin Weitz

Tag der Promotion: 15.09.2009

Abstract

In this thesis I present an experimental realization of controlled systems consisting of trapped neutral atoms strongly coupled to a high-finesse optical resonator. These systems enable the exploration of atom-light interaction at the most fundamental level, and have a potential application in quantum information processing.

Experimental tools for preparation, detection and transport of individual Caesium atoms into the cavity mode are presented. In addition, the setup and properties of the resonator are discussed.

I investigate two different methods to detect the atom-cavity interaction. The first approach relies on the observation of the cavity transmission, which allows us to continuously monitor the interaction dynamics of a single atom coupled to the resonator mode for several seconds. Using this approach I characterize the system and investigate the dependence of the coupling strength on the number of atoms and their position inside the cavity mode. An alternative method, providing information on the atom-field interaction, is based on the detection of the atomic state. We use this method to record the spectrum of the interacting single-atom-cavity system, which reveals the vacuum Rabi splitting - a clear signature of coherent atom-field interaction in the strong coupling regime. Exploiting the strong interaction in combination with the large energy separation between the spin states of Caesium atoms, a projective quantum nondemolition measurement of the atomic spin state is performed. Continuous monitoring of the atomic state reveals quantum jumps between the states. By extending the experiment to the case of two atoms simultaneously coupled to the cavity mode, conditional dynamics of the spin states is observed. By further advancing this method, generation and detection of entangled states might be feasible.

Parts of this thesis have been published in the following journal articles:

1. M. Khudaverdyan, W. Alt, I. Dotsenko, T. Kampschulte, K. Lenhard, A. Rauschenbeutel, S. Reick, K. Schörner, A. Widera and D. Meschede *Controlled insertion and retrieval of atoms coupled to a high-finesse optical resonator*, New J. Phys. **10**, 073023 (2008)
2. M. Khudaverdyan, W. Alt, T. Kampschulte, S. Reick, A. Thobe, A. Widera and D. Meschede *Quantum jumps and conditional spin dynamics in a strongly coupled atom-cavity system*, Phys. Rev. Lett. **103**, 123006 (2009)

Contents

Abstract	V
Introduction	1
1 Experimental setup	3
1.1 Introduction	3
1.2 Cooling and trapping single atoms	3
1.2.1 Magneto-optical trap – a source of single neutral atoms	3
1.2.2 Optical dipole trap – a conveyor belt for atoms	6
1.2.3 Fluorescence detection and imaging of single atoms	18
1.2.4 Transportation and position control	20
1.3 A high-finesse optical resonator	21
1.3.1 Mechanical setup	21
1.3.2 Stabilizing the resonance frequency of the cavity	25
1.3.3 Transmission detection	28
2 Atom-cavity system in the strong coupling regime	31
2.1 The Jaynes-Cummings model	32
2.2 The master equation approach	34
2.3 Detection of atom-cavity coupling via cavity transmission	37
2.3.1 Detection of a single atom inside the cavity	37
2.3.2 Simple model	39
2.3.3 Dynamics of the atom-cavity coupling strength	41
2.3.4 Controlling the coupling strength	45
2.3.5 Atom-number dependent coupling strength	45
2.4 Detection of atom-cavity coupling via the atomic state	48
2.5 Conclusion	50
3 Quantum jumps and normal mode splitting	51
3.1 Introduction	51
3.2 Quantum jumps	52
3.2.1 Intra-cavity quantum nondemolition (QND) detection of the atomic state	52
3.2.2 A random telegraph signal of quantum jumps	54
3.2.3 Characterization of quantum jumps	55
3.2.4 Towards quantum jumps with more than one atom	61
3.3 Measuring the normal mode splitting via the atomic state	65
3.3.1 Experimental sequence	65
3.3.2 Stability of the coupling strength	67
3.3.3 Measurement of the normal-mode splitting via the atomic state	72
3.4 Conclusion	75

Conclusion and Outlook	76
Bibliography	81
Acknowledgements	89

List of Figures

1.1	Principle of Doppler cooling	4
1.2	Principle of the MOT	5
1.3	Relevant energy levels of Cs atom	7
1.4	Standing wave dipole potential	9
1.5	Microscope image of the step-index fiber	10
1.6	Measurement of the polarization properties of the fiber	12
1.7	Quality of the laser beam of the fiber-based DT	14
1.8	Position fluctuation of the DT laser beam	16
1.9	Measurement of the atomic oscillation frequencies inside the DT	17
1.10	Experimental setup and detection optics	19
1.11	Fluorescence CCD image of a single atom stored inside the DT	20
1.12	Schematic of the cavity mirror	21
1.13	Geometrical configuration of cavity, MOT, and DT.	23
1.14	Schematics of the cavity holder	24
1.15	Frequency stabilization of the high-finesse cavity	26
1.16	Lifetime of atoms inside the cavity mode	27
1.17	Sketch of the detection setup	29
2.1	Energy levels in the Jaynes-Cummings model	32
2.2	Energy map in the Jaynes-Cummings model	34
2.3	Dressed states of the atom-cavity system in master equation approach	36
2.4	Continuous strong coupling of a single atom to the cavity field	38
2.5	Probe and lock laser intra-cavity standing waves	40
2.6	Dynamics of a single atom coupling to the cavity field	42
2.7	Dynamics and equilibrium of a single atom-field coupling	43
2.8	Sisyphus-type intra-cavity cooling	44
2.9	Controlling the atom-cavity coupling	46
2.10	Atom-number dependent coupling strength	47
2.11	Detecting the atom-cavity coupling via the final atomic state	48
3.1	Nondemolition intracavity detection of the atomic state	53
3.2	Demonstration of quantum jumps	55
3.3	Histogram of transmission counts for quantum jumps	56
3.4	Schematic representation of the algorithm	57

3.5	Digitization of quantum jumps	58
3.6	Second-order correlation function	59
3.7	Histogram of dwell times	60
3.8	Antibunching of quantum jumps	61
3.9	Quantum jumps of one and two atoms at the cavity edge.	62
3.10	Model for two atoms quantum jumps	63
3.11	Quantum jumps of two atoms: Analysis	64
3.12	The measurement sequence of normal-mode splitting	66
3.13	Scanning the atom cavity coupling strength along the cavity axis	68
3.14	Coupling strength stability after switching off the probe laser	69
3.15	Stability of the coupling strength during the cavity frequency chirp	70
3.16	Dynamics of the coupling strength	71
3.17	Atom-cavity coupling strength during the measurement of the normal-mode splitting	73
3.18	Normal-mode splitting of a single atom	74
3.19	Atomic population transfer by the $F = 4 \rightarrow F = 4'$ probe laser	75
3.20	Providing a better localization of atoms by an additional trapping potential	79

Introduction

Technological advances in the 20th century have made possible the experimental study of quantum-mechanical systems of improving purity and with ever tighter control. A theoretical proposal by David Deutsch in 1985 pointed to a promising application of quantum-mechanical systems: He discovered that processing information according to the laws of quantum mechanics is inherently faster for certain computational problems than classical computing [1]. In 1994 P. Shor developed a quantum algorithm capable of factorizing integer numbers exponentially faster than the fastest known classical algorithm [2, 3]. Shortly after, L. Grover showed that a significant speed-up in searching of a target data in an unstructured database can be achieved using a quantum computer [4].

Seven physical systems aiming at the implementation of basic steps of quantum information processing are being pursued [5]. Neutral atoms are promising candidates for the purpose of quantum information processing. Their weak interaction with the environment results in potentially long coherence times. The challenge which comes along with this potential advantage is the difficulty to induce controlled interaction between individual atoms. Nowadays, three different approaches to induce coupling between atoms are being pursued: By means of controlled cold collisions individual atoms are placed into the same potential well of an optical lattice, where they undergo short-range ground-state interaction [6]. A different approach, exploring the excited state dipole-dipole interaction of closely spaced Rydberg atoms, has been recently employed to demonstrate a considerable progress towards the generation of entangled states [7].

The third approach utilizes the interaction between an atom and a quantized field of an optical resonator, treated in the framework of cavity quantum electrodynamics. There the coupling between individual atoms is realized by placing them inside the mode of a high-finesse resonator, tuned in or near resonance with the atomic transition. In this system atoms interact through the exchange of photons, mediated by the mode of the cavity [8]. This approach has been successfully implemented in the microwave regime, where flying Rydberg atoms interact with the mode of superconducting cavity. In this experiment, multi-atom entangled states have been generated [9, 10].

In this thesis I will present the realization of physical systems composed of one or two atoms strongly interacting with the mode of a high-finesse optical resonator.

A single or two cold caesium atoms are loaded from a magneto-optical trap into the standing wave potential of a far-detuned dipole trap. Using this dipole trap as a conveyor belt, the atoms are placed inside the cavity mode at a predetermined position along the standing wave [11, 12].

The atom-cavity interaction is detected in two different ways: As a first possibility we detect the final internal state of the atom after it has interacted with the cavity mode. By performing an ensemble average, the atom-cavity interaction is detected. Using this technique, spectroscopy of the bound system of a cavity and a single atom is performed, which reveals the normal-mode splitting [13, 14] – a clear evidence of a strong atom-cavity coupling.

As a consequence of the strong coupling, the transmission of a weak probe laser beam, injected into the cavity, is suppressed under insertion of an atom into the mode. This effect is used in an alternative method to continuously measure the atom-cavity coupling via detection of the probe laser transmission. Moreover, the transmission signal reveals the dynamics of external and internal atomic degrees of freedom: On the one hand a variation of the atomic position inside the cavity influences the atom-cavity coupling strength, visible as variations of the transmitted probe laser power. This position-transmission relation could be used to track single-atom dynamics and find application in single-atom microscopy [15]. Moreover, this technique can assist in understanding of cavity-induced cooling processes.

On the other hand, at a stable position, the transmission reveals the atomic spin state: Since the two hyperfine ground states of a Caesium atom are separated by 9.2 GHz, tuning the cavity in resonance with the transition from one of these spin states to the electronically excited state leaves the other spin state uncoupled from the cavity field. In this manner, the observation of the cavity transmission reveals the atomic state almost without affecting it, and therefore performs a so-called quantum nondemolition measurement of the spin state. Applying this measurement technique enables the observation of an intriguing phenomenon of quantum physics – quantum jumps, which are manifested as spontaneous and abrupt changes of the cavity transmission level. Extension of this technique to two atoms, simultaneously coupled to the resonator field, enables the observations of conditional dynamics of the spin states.

Apart from being interesting from the perspective of fundamental quantum physics studies, such controlled and strongly interacting atom-cavity system can be used for the purpose of quantum communication [16], which requires transferring the state of a flying qubit, usually encoded on the polarization of a photon, on the state of a stationary qubit and vice versa.

A quantum register of neutral atoms has been demonstrated in the thesis of D. Schrader [17, 18]. With the achieved progress in controlling the atom-cavity systems, the entanglement of two atoms appears to become possible, which will serve as a basis for two-qubit quantum gates [19, 20, 21]. Thus, we are now approaching the fulfillment of all five DiVincenzo requirements essential for the implementation of a quantum computer with neutral atoms [22].

Chapter 1

Experimental setup

1.1 Introduction

In this chapter I will present the building blocks for our single atom – cavity QED experiment. The experimental setup has evolved to its present state within the last nine years and involves the contributions of a progression of doctoral theses. Therefore I will discuss only the essential parts of the experimental setup, i.e. how we trap, image, and control the position of a well-defined number of isolated cold caesium (Cs) atoms¹, and focus on the latest improvements. Moreover I will review the assembly and essential characteristics of our resonator.

1.2 Cooling and trapping single atoms

1.2.1 Magneto-optical trap – a source of single neutral atoms

The idea of using laser radiation for cooling of neutral atoms has been proposed by Hänsch and Schawlow in 1975 and has been experimentally realized by Steven Chu in 1985 with three-dimensional optical molasses. Two years later, by superimposing an inhomogeneous magnetic field with an optical molasses, trapping of neutral sodium atoms was demonstrated in the group of D. Pritchard [26].

Since then the magneto-optical trap (MOT) became the standard and the most popular tool to cool atoms from room temperature to sub-millikelvin, and subsequently keep atoms trapped at this temperature for a long time. In our experiment we use a MOT as a source of a few or a single atom only, which is enabled by applying a high magnetic field gradient in the presence of a low Cs partial pressure. Since the operation of a MOT is based on radiation pressure, atoms stored in this trap continuously scatter photons, which allows us to monitor their number and determine their position.

¹The details of are described in [23, 24, 18, 25].

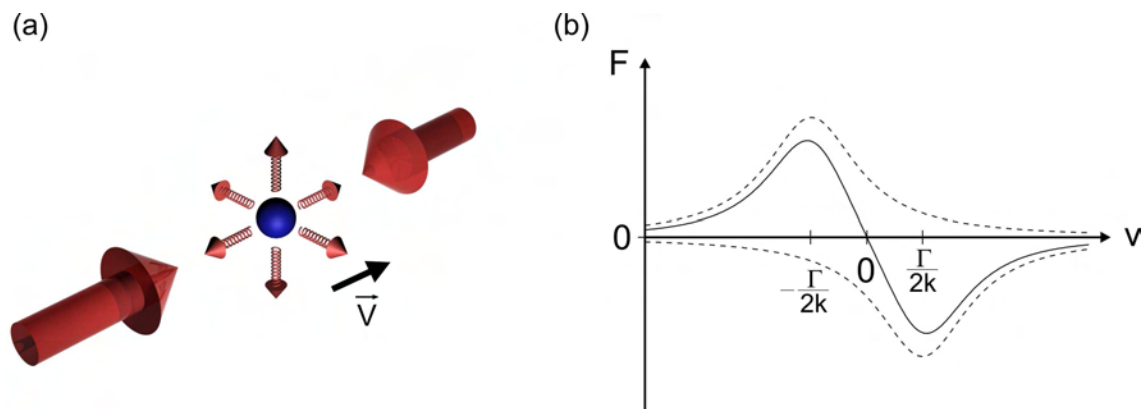


Figure 1.1: Principle of Doppler cooling. (a) An atom, moving between two counter-propagating red-detuned laser beams, preferentially absorbs a photon from the laser beam opposing its motion and emits photons isotropically. (b) Velocity-dependence of the radiation pressure force, imposed by the one-dimensional optical molasses. The dashed lines indicate the forces, exerted by each of the laser beams separately. The solid line indicates their sum.

Principle of operation

The operation of a MOT is based on the velocity and position-dependent radiation pressure force exerted by the photons of the laser radiation [27, 28]. Cooling of atoms in all directions is provided by three pairs of orthogonal red detuned laser beams, forming a so-called 3D optical molasses. Trapping of atoms is provided by adding an inhomogeneous magnetic field which induces position-dependence of the light-pressure force.

Cooling the atoms Figure 1.1 illustrates the principle of the Doppler cooling for the one-dimensional case, easily extendable to three dimensions. Due to the Doppler effect, an atom moving to the right sees the frequency of the laser beam opposing its motion shifted to the blue, i.e. closer to the atomic transition frequency. Therefore, the atom absorbs more photons from the opposing laser beam. Because of the isotropy of spontaneous emission, the momentum transfer due to the emitted photons averages out to zero. Therefore, the atom experiences a net force opposing its motion direction.

Due to the random and discrete nature of the momentum transfer from the scattered photons, the atomic momentum will fluctuate around zero. This fluctuation heats the atom to an equilibrium “Doppler temperature” of

$$T_D = \frac{\hbar \Gamma}{2k_B},$$

where k_B is the Boltzmann constant and Γ is the excited state decay rate [29, 30, 31]. In case of Cs atoms $\Gamma = 2\pi \times 5.2$ MHz and the resulting Doppler temperature is $T_D = 125 \mu\text{K}$.

Trapping the atoms An atom cooled in the optical molasses undergoes diffusive motion and will eventually escape from the molasses within some tens of milliseconds. For our

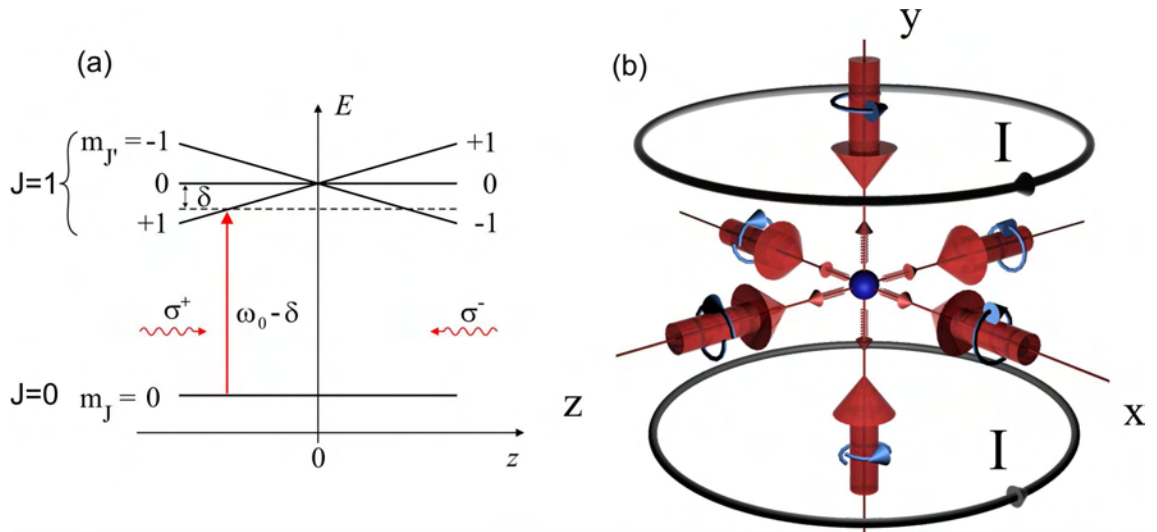


Figure 1.2: Principle of the MOT. (a) Energy-level diagram of an atom with $J = 0$ ground state and $J = 1$ excited state, placed in a magnetic field gradient. The frequencies and polarizations of the counter-propagating laser beams are designed such that they impose cooling and restoring forces at the same time. (b) Schematic view of the MOT. A pair of anti-Helmholtz coils produce a magnetic field gradient in all three dimensions superimposed with the three-dimensional optical molasses.

applications we need to trap atoms, and hence the presence of a position-dependent force localizing the atoms is required. It can be attained by the interplay of an inhomogeneous magnetic field with molasses beams of appropriate polarization, such that whenever an atom moves away from the trap center a restoring force will bring it back to the center.

In Figure 1.2 the principle of this restoring force is illustrated. A hypothetical atom with $J = 0$ ground state and $J = 1$ excited state is placed between a pair of slightly red-detuned counter-propagating laser beams of opposite circular polarizations. In addition, a magnetic field gradient is applied along the direction of laser beams. Due to the Zeeman effect an atom displaced to the left from the center is pushed back to the right since the light coming from the left is tuned closer to the frequency of the allowed σ^+ transition. Similarly, if the atom is displaced to the right it is pushed again towards the trap center. One can extend this arrangement to three dimensions by superimposing a quadrupole magnetic field produced by a pair of coils in anti-Helmholtz configuration, to a three-dimensional optical molasses, see Figure 1.2(b).

Experimental setup

Here I will describe the details of the MOT experimental setup relevant to experiments described in this thesis.

Vacuum system The requirement to perform the experiments on the single atom level poses certain constraints on our experimental setup.

Our MOT resides inside a glass cell providing good optical access. It is attached to a stainless steel cube, which is in turn connected to a Cesium reservoir and to vacuum pumps. A continuously operating ion getter pump maintains an ultra-high vacuum on the order of 10^{-10} mbar, providing a low collision rate with the background gas, which yields a lifetime of atoms in the trap of about one minute.

Magnetic coils Since the purpose of our MOT is to prepare several or single atoms only, it is essential to keep the spontaneous loading rate as low as possible. It has been shown, that the capture cross section σ of a MOT decreases dramatically with the magnetic field gradient [32].

Therefore, for a single atom MOT we use the high magnetic field gradient of $\partial B/\partial z = 300$ G/cm, which is produced by water-cooled magnetic coils in anti-Helmholtz configuration.

In order to load a desired number of atoms into the MOT, we shortly decrease the magnetic field gradient by a factor of 10. This increases the capture cross section of the MOT by more than 4 orders of magnitude and allows us to load a desired average number of atoms within several milliseconds [24, 23].

In order to compensate stray and earth magnetic fields, three pairs of additional coils in Helmholtz configuration are installed outside the glass cell. Moreover, these coils are utilized to produce a guiding magnetic field along a desired direction.

Laser system As sources of laser radiation for the optical molasses we use home-made diode lasers in Littrow configuration. They are stabilized on Cs vapor cells using polarization spectroscopy [33, 23]. Atoms inside the MOT are cooled by laser radiation about one Γ detuned to the red side of the $F = 4 \rightarrow F' = 5$ transition, see Figure 1.3.

During the cooling process there is a finite probability to excite an atom to the state $F' = 4$, from where the atom can then decay to the ground state $F = 3$. In order to bring the atom back into the cooling cycle an additional repumping laser, which is stabilized onto the $F = 3 \rightarrow F' = 4$ transition, is continuously applied during the MOT operation.

1.2.2 Optical dipole trap – a conveyor belt for atoms

The MOT operates as an excellent tool for the preparation of a small number of cold atoms. However, since it is based on dissipative light pressure force, it cannot be used to store and manipulate the qubit states, which we encode on the hyperfine ground states of a Cs atom [18]. Therefore, we implement a different type of trap, a so-called dipole trap, which serves as a conservative potential for the atoms, preserving their internal states [34, 35].

The dipole force as a confining mechanism was first considered by Askaryan in 1962 [36], then in 1968 Letokhov proposed to use the dipole force to trap neutral atoms [37], and finally in 1986 in the group of S. Chu the first dipole trap (DT) for neutral atoms was realized [38].

In our experiment we employ a DT in the form of a one-dimensional optical lattice, which we use as a conveyor belt for neutral atoms. Using this conveyor belt we transport

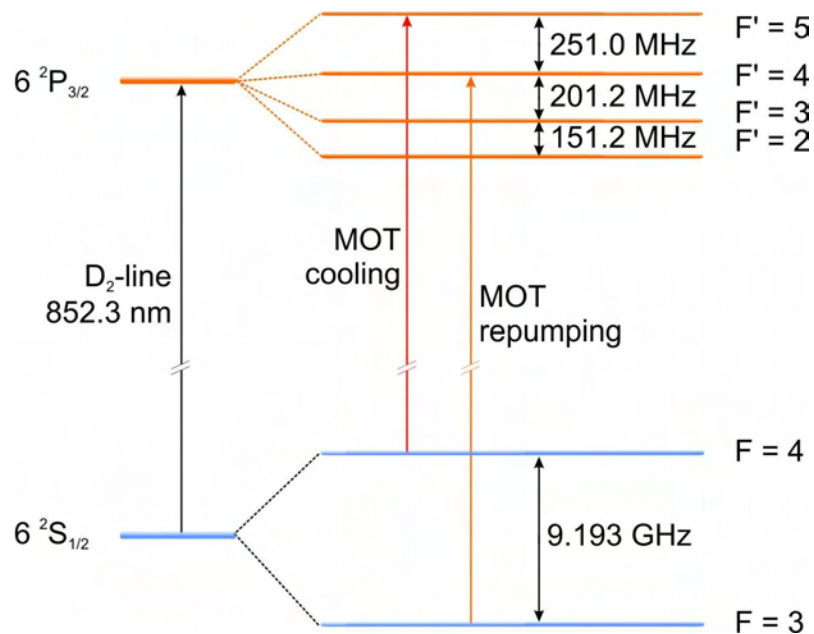


Figure 1.3: Simplified level scheme of Cs atom with relevant transitions for the laser cooling.

atoms over macroscopic distances to a predetermined position with submicrometer precision [12, 25]. Specifically, we use it to shuttle atoms from the MOT into the mode of the resonator, see Chapter 2.

Dipole potential

The principle of dipole potential is widely covered in the literature and discussed in some former theses of our group to a great extent, see References [34, 23] and references therein. Here only the results of the simplest classical treatment of the dipole potential will be presented. In the classical description the dipole potential and photon scattering rate can be approximated by

$$U_0 = \frac{3\pi c^2 I}{2 \omega_0^3} \left(\frac{\Gamma}{\Delta} \right), \quad (1.1a)$$

$$R_s = \frac{3\pi c^2 I}{2\hbar\omega_0^3} \left(\frac{\Gamma}{\Delta} \right)^2, \quad (1.1b)$$

where ω_0 and ω are the angular frequencies of the atomic transition and laser radiation, respectively, I is the light intensity, c is the speed of light, and the atom-laser detuning $\Delta = \omega_0 - \omega$. This approximation agrees well with the quantum-mechanical results. For a typical total optical power of few Watts and the $1/e^2$ radius of the DT laser beam in focus of about $w_0 \approx 34 \mu\text{m}$: The potential depth $U_0 \approx k_B \times 1 \text{ mK}$ (here k_B is the Boltzmann constant), which is larger than the temperature of the atoms in the MOT enabling the

close to loss-free transfer from the MOT into the DT, and the scattering rate is R_s is less than 10 s^{-1} , which is much smaller than our typical single qubit rotation time of $16 \mu\text{s}$, see References [17, 18].

Standing wave trap

The very first dipole trap for neutral atoms was simply a single focused laser beam, sufficiently detuned from the atomic resonance [38]. Since then a variety of different trap configurations have been proposed and implemented, which have been used for different applications, see References [39, 40, 41].

Trap geometry Our DT is formed by two counter-propagating laser beams with a wavelength of $\lambda_{\text{DT}} = 1030 \text{ nm}$ and a typical total power of about $P \approx 4 \text{ W}$. The resulting interference pattern is a chain of equidistant spatially-modulated potential wells with the intensity and the potential shape, given below

$$\begin{aligned} I(y, \rho) &= I_P \frac{w^2(y)}{w_0^2} e^{-\frac{2\rho^2}{w^2(y)}} \cos^2(ky), \\ U &= U_0 \frac{I(y, \rho)}{I_P}, \end{aligned} \tag{1.2a}$$

where w_0 is the beam waist ($1/e^2$ beam radius in the focal plane), $w(y)$ is the $1/e^2$ beam radius, $k = 2\pi/\lambda_{\text{DT}}$ is a wave vector, I_P is the peak intensity, and U_0 is given in Equation 1.1a. Here cylindrical coordinates are used and ρ is the distance from the DT axis (y -axis). The expressions for the beam radius, Rayleigh range and the peak intensity are

$$\begin{aligned} w^2(y) &= w_0^2 (1 + y^2/y_0^2), \\ y_0 &= \pi w_0^2 / \lambda_{\text{DT}}, \\ I_P &= \frac{4P}{\pi w_0^2}, \end{aligned}$$

respectively. Here P is the total optical power of the laser beams. An illustration of the standing wave dipole potential is presented in Figure 1.4. Note that for illustrative purposes the wavelength of the laser beam has been elongated by a factor of 5200.

Generation of aberration-free dipole trap laser beams

For the experiments which involve the manipulation of the internal and external states of the atoms, it is preferential to trap atoms in a potential free of spatial distortions and fluctuations.

So far, the standing wave potential of our dipole trap was formed by laser beams, guided by free-beam optics from the Yb:YAG disk laser to the vacuum chamber. Each beam was reflected by about a dozen mirrors, resulting in an optical path length of several meters. The unavoidable drawback of such a configuration is that the acoustical vibrations and temperature drifts in the laboratory induce significant fluctuations and drifts of the

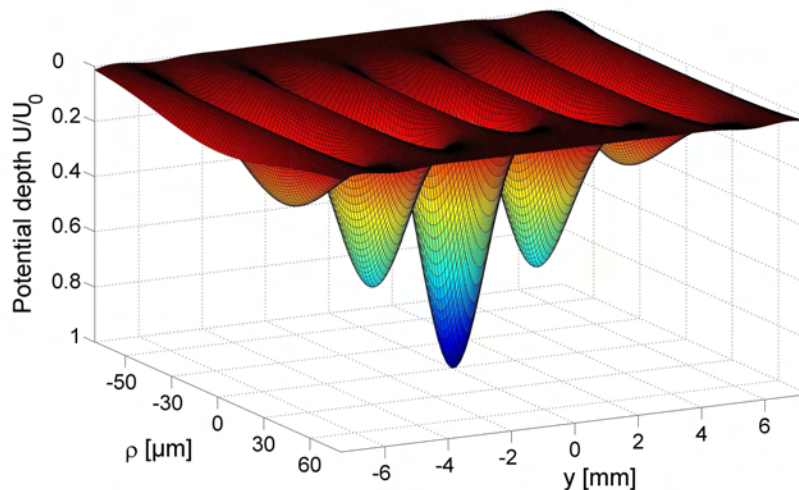


Figure 1.4: Visualization of a standing wave dipole trap potential. The wavelength of the laser beam is stretched by a factor of 5200.

beam position. In our current experiments, we transport atoms into the microscopic cavity mode with spatially varying strength of the coupling strength. Hence, any displacements of the trapping potential result in a non-reproducible coupling strength and degrade the experimental data, where typically ensemble averaging is required.

In order to improve the pointing stability of the DT, we have installed high-power polarization-maintaining optical fibers close to the vacuum chamber. In this way, the geometry of the DT is decoupled from the fluctuations of the DT laser beams along the optical path before the fiber. These fluctuations now only translate into a slightly varying coupling efficiency of the beam into the fiber. In the following I will describe the investigation and properties of our optical fibers.

An optical fiber for the DT stabilization For an appropriate shape of the DT the following requirements for an optical fiber should be fulfilled:

1. High transmission at the level of several Watts of optical power, which we typically use for the DT in the experiment.
2. Minimal distortion of the polarization purity of the laser beam by the fiber.
3. Gaussian beam profile at the fiber output.

We have investigated several types of optical fibers, including polarization-preserving step refractive index fibers and photonic crystal fiber. The most suitable fiber for our purposes appeared to be a step refractive index fiber (Passive-10/123-PM, LIEKKI). In Figure 1.5, the microscope image of the cleaved facet of the fiber is presented.

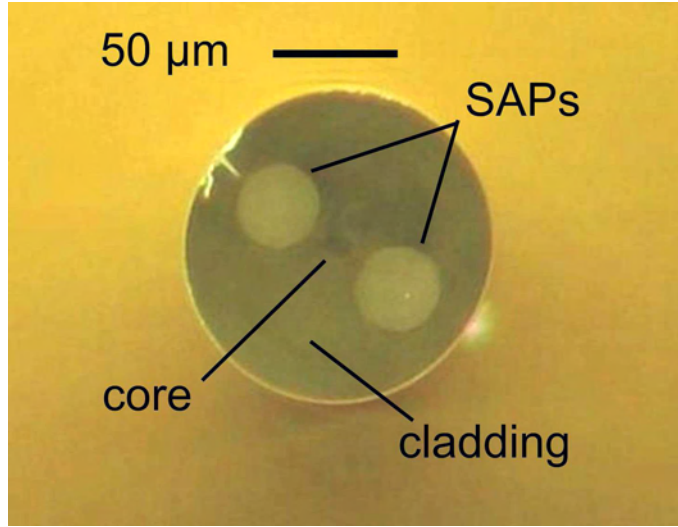


Figure 1.5: Microscope image of the step-index fiber facet. SAPs of PANDA-type induce stress on the fiber core causing birefringence.

This single mode fiber has a numerical aperture of $NA \approx 0.06$. This relatively low NA stamps from a large diameter of the fiber mode ($10 \mu\text{m}$). This results in a reduced light intensity and helps to avoid the nonlinear processes inside the fiber, e.g. the stimulated Brillouin scattering which limits the amount of light delivered at the fiber output [42]. The polarization preserving property of the fiber is induced by internally generated stress. It is applied to the core of the fiber by “stress-applying parts” or SAPs, which are incorporated into the fiber cladding.

The SAP in our case is a silica rod, which has a higher heat expansion coefficient than the cladding. At the end of the fiber manufacture process, during the cooling phase, it shrinks more than the cladding, generating mechanical pressure on the core [43]. Along the direction parallel to the field of tension, the fiber core has a higher refractive index. This axis is often referred to as the “slow axis”. Similarly, the axis perpendicular to the slow axis is thus called “fast axis”. Using this induced birefringence of the fiber, it is then possible to transmit light of linear polarization² so that it ideally remains linear at the fiber output.

Polishing the fiber In order to prevent backreflections into the light mode and associated interference effects, the fiber is polished under 8° angle at both ends, which are assembled to FC/APC connectors (Thorlabs), glued to the fiber with epoxy.

The polishing process is performed in four steps. In the first step the fiber end is polished with a $5 \mu\text{m}$ polishing film. The purpose of this step is to quickly remove excess epoxy from the tip of the connector. When only a thin layer of epoxy remains on the tip, the fiber is polished with a $3 \mu\text{m}$ film until the edges of the epoxy bead begins to break up. At the third step a $1 \mu\text{m}$ polishing film with few drops of water was used. In the final step

²When the light polarization is parallel to either the slow or to the fast axis of the fiber.

we use a wet $0.3\ \mu\text{m}$ film.

Measuring the polarization maintenance of the fiber As discussed in Reference [18], the purity and stability of the polarization of the DT laser is an essential prerequisite for the position-dependent manipulation of the qubit states, encoded in the hyperfine ground states of a Cs atom.

The polarization purity at the output of the optical fiber is defined by the amount of crosstalk between its orthogonal modes. This crosstalk causes the light with the linear polarization at the input of the fiber to leave the fiber with an alternating mixture of linear and circular polarizations, resulting in the time-dependent light shift of atomic state. This might disturb the position-dependent manipulation the atomic internal states and cause their decoherence [17, 18].

Here I will present a method to determine the amount of the crosstalk in the polarization-maintaining fiber [44]. This method is based on the very slight variation of the fiber birefringence with respect to the change of the fiber temperature. In Figure 1.6 (a) the test setup for the fiber characterization is presented. For technical reasons the tests were performed with a Nd:YAG laser supplying radiation at 1064 nm wavelength, only 34 nm away from the wavelength of the Yb:YAG laser, used to generate DT in our experiment. Since the cutoff wavelength of the fiber is 900 nm, the test results achieved with the wavelength of 1064 nm should yield almost the same outcome as with 1030 nm.

In order to minimize the polarization crosstalk at the fiber input, we first carefully match the beam polarization with one of the orthogonal polarization modes of the fiber. A linear polarized beam from the Nd:YAG laser is coupled into a 1 m long polarization-maintaining fiber. We monitor the state of the polarization at the fiber output while heating the fiber with a heat gun, see Figure 1.6 (a). The crosstalk between the polarization modes of the fiber and not perfectly matched polarization at the fiber input causes the change in the state of the output polarization, which is measured by observing the modulation of the output beam power, transmitted through the polarizing beam splitter PBS₂. In order to achieve the best sensitivity of the transmission signal to the polarization crosstalk, using HWP₂ we set the transmitted power P_{init} after PBS₂ to the level of 50% of the total power at the fiber output.

Figure 1.6(b) shows a typical transmission signal, measured for a HWP₁ angle of $\alpha_1 = 61.5^\circ$. After about one second the heat gun is turned on, inducing a phase difference between light propagating in the two polarization modes of the fiber. Since the polarization at the fiber output is given by the coherent superposition of light in the modes, the signal at the photodiode exhibits a periodic variation between its maximum P_{max} and minimum P_{min} during the phase changing process, see Figure 1.6 (b).

The amount of crosstalk between the fiber modes is determined by the the relative modulation of the transmission signal. Knowing the contrast of the transmission signal $C = (P_{\text{max}} - P_{\text{min}}) / (2P_{\text{init}}) = \delta P / (2P_{\text{init}})$, it is straightforward to calculate the extinction ratio of the fiber polarization $P_{\perp} / P_{\parallel}$, where P_{\parallel} and P_{\perp} are the optical powers propagating inside the orthogonal modes parallel and perpendicular to the laser beam polarization at the fiber input, respectively. This ratio equals to

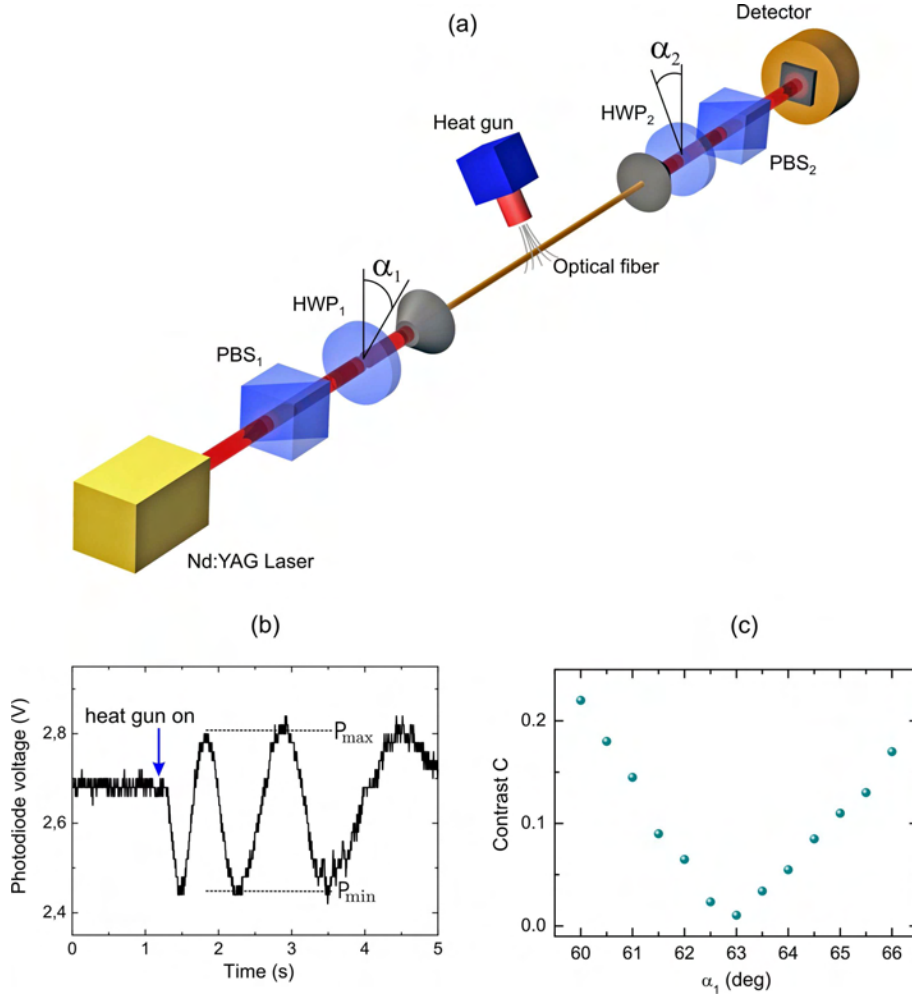


Figure 1.6: Measurement of the polarization properties of the fiber. (a) Schematic view of the fiber characterization setup. HWP denotes the half-wave plate, PBS stands for the polarization beam splitter. (b) A typical transmission signal after PBS₂ while changing the fiber temperature. (c) The contrast C of the transmission signal as a function of the tilting angle α_1 of the HWP₁. At the angle of 63° the polarization of the incoming beam has a best match with the polarization mode of the fiber and $C = 0.01$.

$$\frac{P_{\perp}}{P_{\parallel}} = \left(\frac{\delta P}{4P_{\text{mit}}} \right)^2 = \frac{C^2}{4}.$$

The minimal value of C in Figure 1.6(c) is equal to 0.01, which corresponds to an extinction ratio of the polarization modes of 1:40000 (46 dB). In an independent measurement we observe no variation of the total power at the fiber output while heating up the fiber, implying that the observed modulation is caused by the crosstalk between the modes of the fiber only.

The transmission of the fiber and the geometrical properties of the beam at the fiber

output were analyzed: The measured transmission equals to 85% which includes about 4% losses at each of uncoated fiber ends. The light from the fiber output shows no visible deviation from the Gaussian TEM₀₀ mode, and an independent measurement with a shear-plate interferometer shows no significant wavefront distortion.

Fiber collimator In order to generate a well-shaped DT, the laser light coupled out of the optical fiber should be collimated and focused without introducing aberrations and distortions to the beam. Moreover, we have to ensure that the geometry of the DT is compatible with the high-finesse resonator (see Section 1.3). The radial extension of the dipole trap laser beam should be smaller than the distance between the cavity mirrors, essentially preventing clipping by the cavity mirrors. Unless this is ensured, heating of the mirror’s edges would cause a substantial stress on the cavity resonance stabilization loop. The waist of the DT also should not be too small, which would otherwise result in a short Rayleigh length of the DT. Due to the separation between the MOT position and the cavity mode of about 5 mm, the DT trap depth at the MOT position would be reduced, resulting in an inefficient MOT-to-DT transfer. Therefore, we chose a geometry of the DT as a tradeoff between these two conflicting requirements.

Collimator performance In order to collimate the laser beam, delivered by the optical fiber, we use a triplet objective (06GLC006, Melles Griot). This diffraction limited objective consists of a combination of a doublet achromat and a meniscus lense, corrected for astigmatism and spherical aberrations, and it has a numerical aperture of NA= 0.2, more than factor 3 larger than the fiber NA. The collimated beam with a waist of about $w_0 \approx 3$ mm is then focused with a plano-convex lens ($f = 300$ mm) to a waist of about $w_0 \approx 34 \mu\text{m}$ between the position of the MOT and the center of the cavity mode. I have numerically simulated the performance of this optical system using “OSLO” – a software for optical design.

In Figure 1.7 the intensity distribution of the dipole trap laser beam is presented for the following cases:

- (a) Intensity distribution in the focal plane lying in between the MOT and cavity mode positions. The green dots stand for the measurement data. The measurement is performed by placing the beam-profile CCD-camera (model L230, Spiricon) in the attenuated laser beam of the DT, and subsequently binning the CCD-counts along the the z-axis³. The solid line is calculated with “OSLO” using the parameters of the lenses, assuming a Gaussian beam at the fiber output with $\theta \simeq 0.06$. The open triangles are calculated assuming ideal aberration-free lenses.
- (b) The same as in case (a), but here the intensity distribution is evaluated at the position of the MOT center, situated 2.3 mm before the focal plane.
- (c) In analogy to the cases (a) and (b), the data and calculations correspond to the position of the cavity mode, 2.3 mm behind the focal plane.

³Because the DT beam is cylindrically symmetric, the choice of the binning axis does not matter.

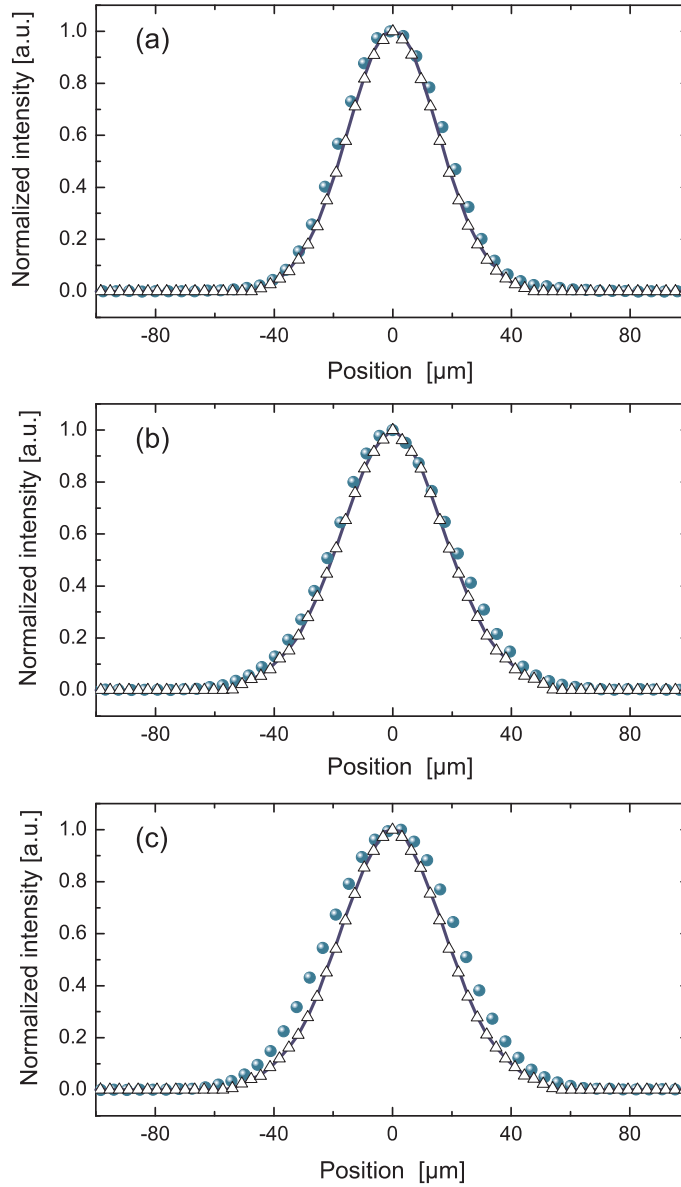


Figure 1.7: Simulated and measured intensity distribution of the laser beam forming the dipole trap. (a) Intensity distribution in the focal plane. The green circles are the result of a measurement with a beam-profile CCD camera, the solid line is calculated using “OSLO” for the parameters of our DT optics, and open triangles are calculated for an ideal optical system. (b) and (c): The same as in (a), but for the positions of the MOT and the cavity mode, respectively. All three cases show a very good agreement between the measurement and the calculations.

Figure 1.7 implies that the measured intensity distributions in the focus as well at the positions of the MOT and the cavity mode has no significant deviation from the intensity

distributions calculated either assuming our optical elements or an ideal optical system⁴. Therefore our imaging system design enables us to generate the standing wave DT with a beam quality close to the diffraction limit. This is underlined by the measurement of the oscillation frequencies of the atoms in the DT potential, see Section 1.2.2.

Pointing Stability In order to quantify the improvement of the spatial stability of the DT laser beams, we compare the pointing stability of the DT before and after installing the optical fibers. For this purpose the position fluctuations of the beam center in its focus is recorded outside the vacuum chamber using the beam-profile CCD-camera at a frame rate of about 50 fps.

Figure 1.8(a-d) shows the recorded relative position along two orthogonal axis, namely the x -axis and y -axis, of the laser beam center on the CCD-chip as a function of time for free-propagating and fiber-filtered laser beam, respectively. In case of the fiber-based DT, the fluctuations are significantly smaller than for free-propagating laser beams. In both cases the periodic broadening and shrinking of the fluctuations are caused by the temperature-controlled air conditioner: During operation, it produces a strong air flow causing turbulences which affect the refraction index of the air in the beam path of the DT laser beam, and therefore destabilize the DT.

Using the recorded data I have calculated the standard Allan deviation, which quantifies the beam fluctuations on different timescales [45]. For this purpose the recorded trace is subdivided into intervals of a duration τ . On each of these intervals m the average $\bar{x}_{\tau,m}$ is calculated. The resulting Allan deviation for the position x ⁵ on the CCD-chip as a function of τ is then given by

$$\sigma_A(\tau) = \sqrt{\sum_{m=1}^N \frac{(\bar{x}_{\tau,m+1} - \bar{x}_{\tau,m})^2}{2N}}.$$

Figure 1.8(e) and (f) shows the Allan deviation for the free-running and fiber-based DT, respectively. The spatial fluctuations of the fiber-based DT are suppressed by about a factor of three at almost the full range of the measured timescales.

Oscillation frequencies in the dipole trap

For experiments involving the manipulation of the internal and external degrees of freedom, precise knowledge of the DT parameters is essential. In principle, the knowledge about the optical power and the beam shape should be sufficient to determine the depth and the waist of the standing wave. However, due to imperfections of the Gaussian beam and aberrations introduced by the optical components, the resulting parameters can deviate significantly from the theoretical expectation.

In order to determine both the depth and the waist of the DT at the position of the MOT we have performed a measurement of the oscillation frequencies of the atoms inside

⁴At the cavity position slightly higher deviations between the calculation and the experimental data are observed. Since the focal plane is not known a priori, it might be caused by the offset of the position of the CCD-camera with respect to the focal plane. We estimate the value of this offset to be about 0.5 mm.

⁵In analogy the Allan deviation for y is calculated.

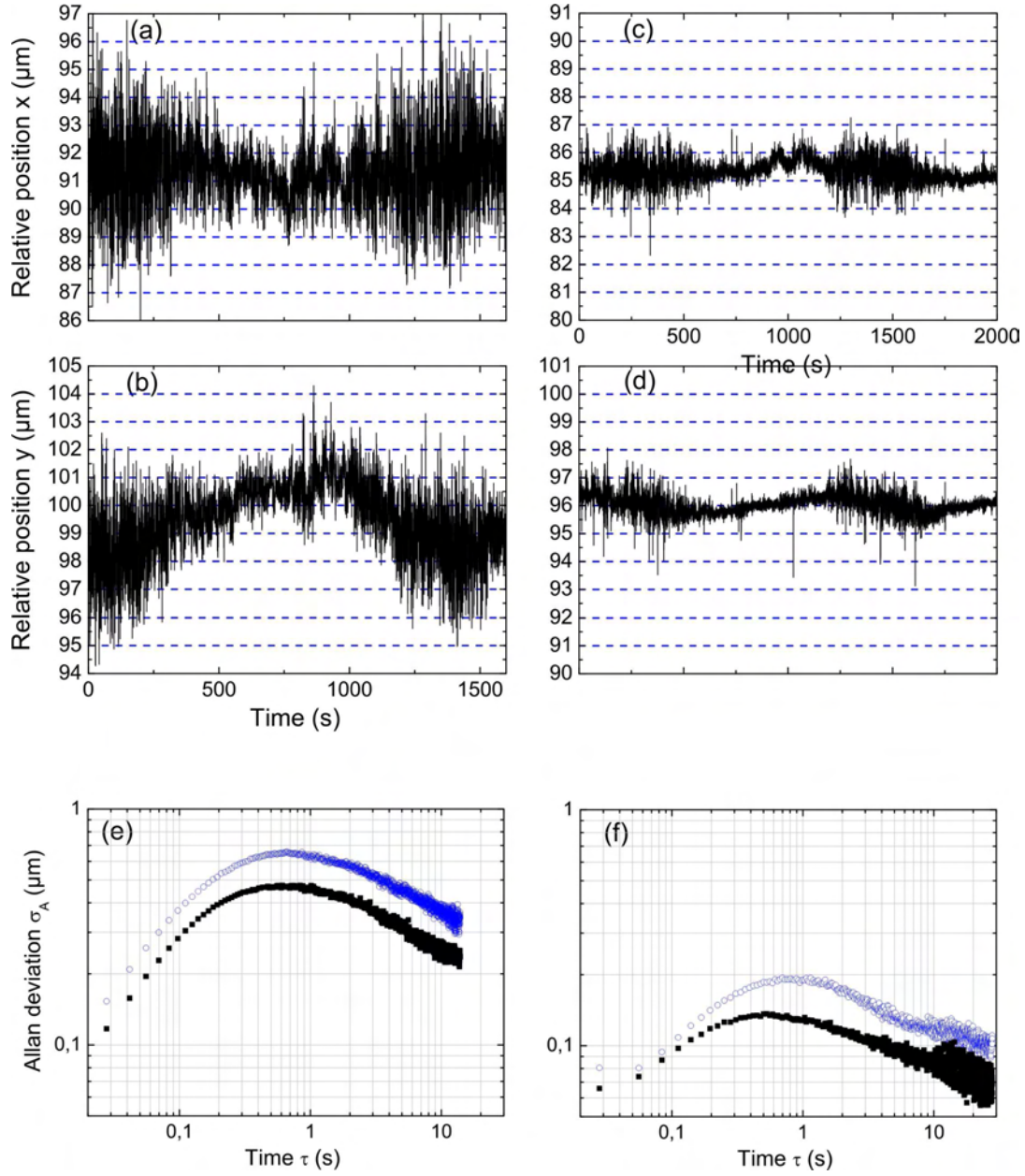


Figure 1.8: Position fluctuations of the DT laser beam in the focal plane, recorded for: (a) Free-propagating laser beam along x -axis, and (b) along the y -axis. (c) Fiber-based laser beam for the x -axis, and (d) for the y -axis. (e) Allan deviation for the free-beam DT (open circles corresponds to $\sigma_A(x(\tau))$, squares to $\sigma_A(y(\tau))$), and (f) for the fiber-based DT.

the dipole trap, following the procedure in Reference [23]. The oscillation frequencies along (Ω_{ax}) and transverse (Ω_{rad}) to the axis of the DT are given by

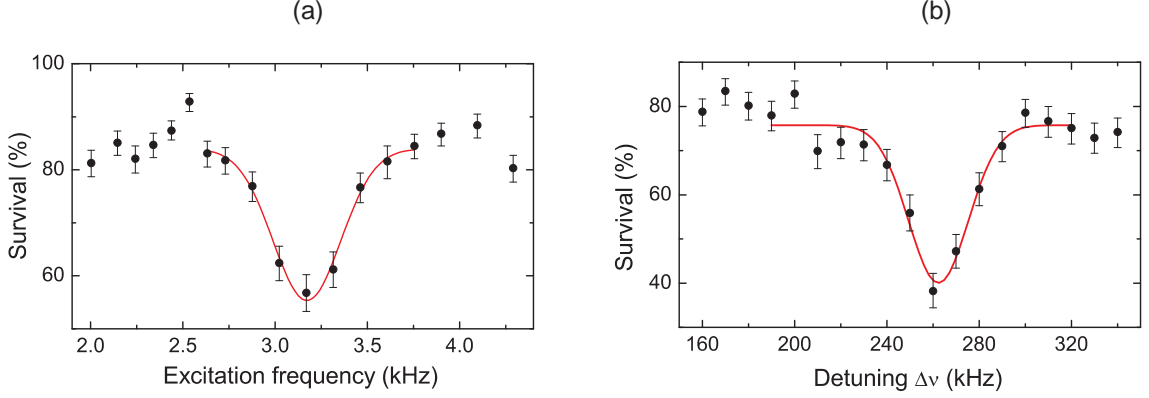


Figure 1.9: Measurement of the atomic oscillation frequencies in the DT. (a) Radial frequency: survival of the atoms after parametric heating as a function of excitation frequency is fitted with the Gaussian (solid line) and yields the radial frequency of $\Omega_{\text{rad}}/2\pi \approx 1.6$ kHz. (b) Axial frequency: survival as a function of the mutual detuning between the DT beams $\Delta\nu$ is fitted with the Gaussian, implying $\Omega_{\text{ax}}/2\pi \approx 260$ kHz.

$$\Omega_{\text{ax}} = 2\pi \sqrt{\frac{2U_0}{m_{\text{Cs}} \lambda_{\text{DT}}^2}},$$

$$\Omega_{\text{rad}} = \sqrt{\frac{4U_0}{m_{\text{Cs}} w_0^2}},$$

where $m_{\text{Cs}} = 2.206 \times 10^{-25}$ kg is the mass of a Cs atom, and U_0 is the depth of the DT. Therefore, by measuring both oscillation frequencies, the depth of the trap and its radial extension can be extracted.

The measurement of the radial frequency is performed by modulating the depth of the dipole trap and measuring the atomic survival probability. The oscillation of the atom is excited parametrically if the excitation frequency is twice the oscillation frequency. Since the harmonic approximation of the DT potential is valid only in the vicinity of its bottom, atoms with a temperature significantly exceeding 10% of the potential depth would oscillate with notably smaller frequencies. Therefore, we ensure the harmonic approximation by heating the atoms such that after the heating they are still confined close to the potential bottom. In order to measure the relative increase of atomic temperature, we lower the trap depth to a level slightly exceeding the average atomic temperature in the case of no heating. Under this condition, even a small increase of atomic temperature results in a loss of a significant fraction of heated atoms. We then transfer the atoms back into the MOT to measure the survival probability.

The measured survival probability as a function of excitation frequency is presented in Figure 1.9(a). A clear dip of the survival probability is observed at an excitation frequency of about 3.2 kHz, implying that the oscillation frequency in the radial direction is equal to $\Omega_{\text{rad}}/2\pi = \nu_{\text{ex}}/2 \approx 1.6$ kHz.

In order to measure the frequency of the atoms in the axial direction of the dipole trap, we used the procedure described in [23]. A partial reflection of one of the dipole trap laser beams from the glass cell window interferes with the standing wave pattern. If we bring the dipole trap into motion, this interference will result in a wobbling of the potential, both in phase and the amplitude. It is easy to show that the frequency of this wobbling is equal to the mutual detuning of the dipole trap laser beams $\Delta\nu$. Whereas the modulation of trap depth, as we pointed out above, results in parametric excitation of the atoms, the modulation of the phase induces resonant excitation, which in our case is the dominant heating mechanism [23].

We chose a transportation distance of 0.5 mm, much smaller than the Rayleigh length of 4.6 mm. The variation of the axial oscillation frequency at this transportation distance is about 0.6%, and therefore can be neglected. The survival rate as a function of the laser beam detuning is shown in Figure 1.9(b). The dip caused by resonant excitations implies an oscillation frequency in axial direction of $\Omega_{\text{ax}}/2\pi \approx 260$ kHz.

The measured oscillation frequencies agree within 5% with our theoretical expectation, yielding a significant improvement with respect to the free-beam setup of the DT⁶, and implying a negligible amount of aberrations in the present laser beams of the DT.

1.2.3 Fluorescence detection and imaging of single atoms

Spatial detection of atoms in the DT using fluorescence imaging in combination with the conveyor belt technique allows us to control the external degrees of freedom of the atoms with submicrometer precision [12, 25]. Furthermore, using two crossed conveyor belts we have generated strings of equidistant atoms and even merged two atoms into the same potential well of the DT [46, 47]. Moreover, imaging of atoms enabled the position-dependent manipulation of the internal atomic states and the realization of quantum register [17].

In our current experiments we need to couple atoms to a mode of high-finesse resonator, located 4.6 mm away from the MOT position. Knowing the initial position of the atom, we can place atom precisely at a desired location of the cavity mode, see Section 1.2.4.

In order to image the atoms we collect the fluorescence light emitted by the atoms, and collimate it by a home-made diffraction limited objective [48] (NA=0.29), covering 2.1% of the total solid angle. The collected light is then split by a polarizing beam splitter (PBS), see Figure 1.10(a). The transmitted part is spatially and spectrally filtered and is focused onto an avalanche photodiode (APD).

Figure 1.10(b) shows a typical fluorescence signal. A high signal-to-noise ratio of the signal and a relatively low background level allows us to determine exact number of atoms stored inside the MOT within several milliseconds with a certainty above 95% for 1-3 atoms. Moreover, we use this fluorescence signal to prepare a desired number of atoms into the DT for further experiments [49].

The fluorescence light from the atoms is partially imaged onto the photocathode of an ICCD camera. A single photon detected by the camera generates on average 350 counts at the CCD chip, distributed in a 3×3 pixel area with 50% of the counts concentrated

⁶In the free-running configuration of the DT the expectations for the oscillation frequencies are about 30% larger than the measured values.

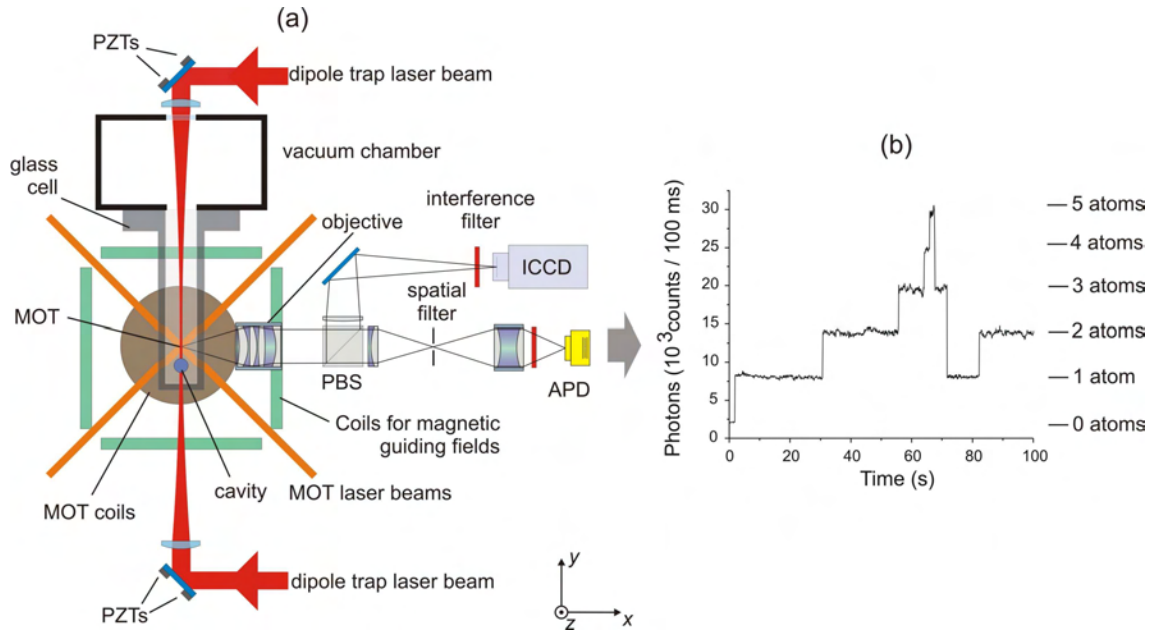


Figure 1.10: (a) Schematic view of the experimental setup. The laser beams of the MOT and the DT are overlapped inside the glass cell. The fluorescence from the atoms is collected by the imaging optics, split by the PBS and sent to the APD and the intensified CCD camera (ICCD). Using piezoelectric actuators (PZTs), the laser beams of the DT can be tilted in xy and yz planes. (b) The fluorescence signal of the atoms, trapped in the MOT allows us to count the atoms.

in the central pixel [50]. The optical magnification factor is equal to $26.1(\pm 0.1)$, yielding that one pixel of ICCD camera with a size of $13 \mu\text{m}$ corresponds to $0.449(\pm 0.02) \mu\text{m}$ at the focal plane of the objective, i.e. at MOT position.

Figure 1.11 shows a CCD-image of a single atom trapped inside the potential well of the fiber-based DT. During the exposure time of one second the three dimensional optical molasses is switched on. The molasses is generated by the cooling and repumping laser beams of the MOT. In order to ensure cooling of trapped atoms, an appropriate detuning and power of the cooling beams are carefully adjusted.

The equilibrium temperature of the atoms, stored in the DT and illuminated with the molasses, has been determined in the Reference [23]. However, since then a different Yb:YAG disk laser has been employed for the DT generation. In contrast to the old laser source (Nd:YAG), it lases at a single longitudinal mode, which forbids the anticipated three and four-photon heating processes, see Reference [18].

In order to determine the atomic temperature, I follow the procedure described in Reference [23]. There, the temperature is extracted from the radial oscillation frequency known from the DT parameters, and the radial extension of the atom during the molasses illumination which can be obtained from the fluorescence picture.

In the radial direction the extension of the potential well is determined by the waist of the DT at the MOT position, and the atomic temperature. The resulting histogram,

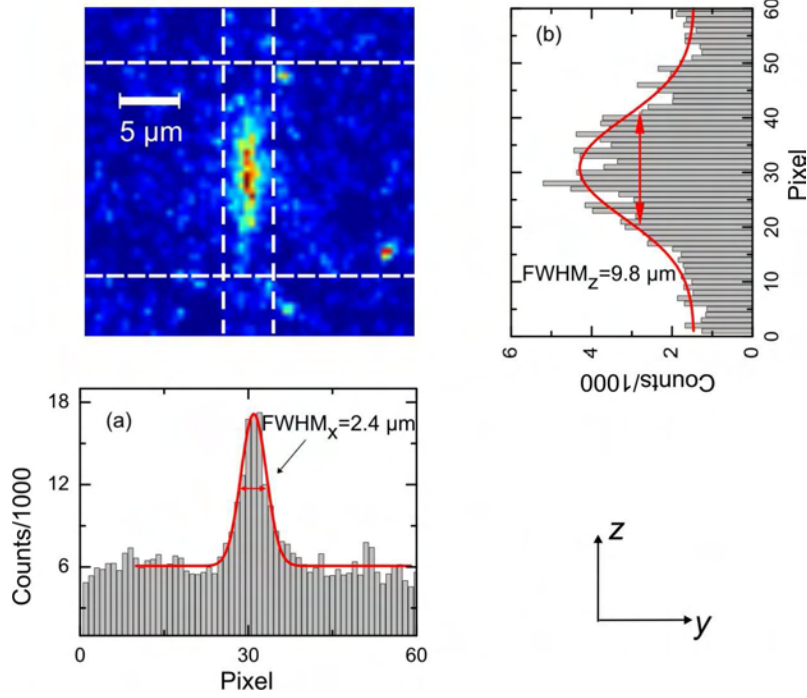


Figure 1.11: Fluorescence CCD image of a single atom inside the fiber-based DT. The atom is illuminated with an optical molasses for 1 sec. (a) The image counts are integrated along the horizontal direction and fitted with the line spread function of our imaging system, yielding the $\text{FWHM}_x = 2.4 \mu\text{m}$. The histogram in (b) is fitted with a Gaussian resulting in a $\text{FWHM}_z = 9.8 \mu\text{m}$.

obtained after integrating the CCD counts along the z -axis, is fitted with a Gaussian yielding the $1/\sqrt{e}$ radius of $\sigma_z = 4.2 \mu\text{m}$. Subtracting the broadening caused by the diffraction and blurring of our imaging system the radial extension of the atomic wave packet is extracted and equals to $\sigma = 4 \mu\text{m}$. Following Reference [23], the temperature of the atoms is equal to

$$T = \frac{m_{\text{Cs}} \Omega_{\text{rad}}^2 \sigma^2}{k_{\text{B}}} = (33 \pm 6) \mu\text{K}.$$

Here $\Omega_{\text{rad}}/2\pi = (1.8 \pm 0.2) \text{kHz}$ is somewhat larger than the value in Equation 1.9 due to slightly different DT parameters. This temperature is about factor of 2 lower than in the former free-beam DT, generated by Nd:YAG laser [23]. This decrease is most probably attributed to the single-frequency operation of Yb:YAG laser.

1.2.4 Transportation and position control

For the controlled manipulation of individual atoms the ability to control their position in space is usually required. In some experiments this transportation is achieved in an uncontrolled way, for instance, using the gravitational potential [51]. In the group of S. Haroche in Paris flying Rydberg atoms interact with the mode of the microwave cavity,

restricting the precise knowledge of the position of interacting atoms [52]. Our experiment is designed to induce deterministic coupling between individual atoms inside the resonator.

In order to bring the standing wave potential (with the form given in Equation 1.2a) into motion, we slightly detune the frequency of the one beam ν_1 with respect to that of the counter-propagating beam ν_2 . The resulting time-dependent standing wave potential then reads as follows

$$U(y, \rho) = U_0 \frac{w_0^2}{w^2(y)} e^{-\frac{2\rho^2}{w^2(y)}} \cos^2(ky - \pi\Delta\nu t),$$

where $\Delta\nu = \nu_1 - \nu_2$ is the mutual detuning of both laser beams. Changing the frequency $\Delta\nu$ sets the standing wave pattern in motion with velocity equal to $v = \lambda_{\text{DT}}\Delta\nu/2$, and atoms confined to the potential minima follow the motion of the interference pattern. In this way we are able to transport a single atom over mm-scale distance with submicrometer precision [12].

1.3 A high-finesse optical resonator

In this section I will discuss the mechanical setup, properties, and stabilization of our high-finesse optical resonator.

1.3.1 Mechanical setup

The realization of a coherent atom-atom interaction via the cavity field is one of the major goals of our experiment. As discussed in Chapter 2, the key requirement for this realization is that the coherent energy exchange rate g should exceed the dissipative decay rates: The photon leakage from the cavity and the spontaneous decay of the atomic state.

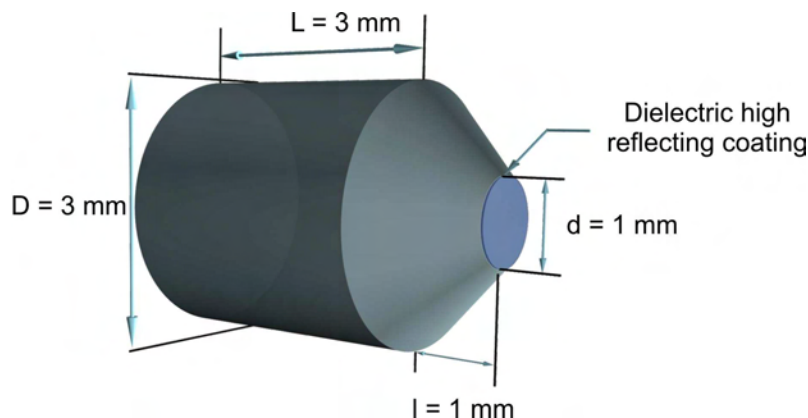


Figure 1.12: Schematic of the cavity mirror. The mirror has a coned shape with a diameter of the front surface of 1 mm. The front surface of the cavity is supplied with dielectric coating, providing a reflectivity of better than 99.9997 %.

According to Equation 2.3 the coupling strength $g \sim 1/\sqrt{V}$, where V is the volume of the cavity mode. Therefore the maximal coupling is attained by reducing V . This

requires a small distance and a small radius of curvature of the mirrors. In order to keep the photon loss rate as low as possible, mirrors of the highest possible reflectivity at the atomic wavelength are required.

Mirror design

Our high-finesse optical cavity is composed of two concave mirrors. Each mirror (Research Electro-Optics) has a diameter of 3 mm and is coned to 1 mm at the mirror surface, see Figure 1.12. This cavity geometry is necessary for two reasons: First, because of spatial orientation of the cavity with respect to the laser beams of the MOT (see Figure 1.13), the coned shape of the mirrors ensures a high clearance for the MOT beams and allows us to place the cavity relatively close to the MOT position. Second, for a fixed distance between the mirrors, a smaller mirror diameter provides a larger distance between edges of the mirrors, reducing the clipping of the DT laser beam. Making the mirror diameter too small would introduce additional losses of the Gaussian cavity mode due to diffraction on the finite mirror aperture. The chosen diameter of 1 mm is a tradeoff between these criteria.

The front surface of each mirror is superpolished to a curved concave surface with a radius of curvature of $R = 5$ cm. The surface is covered with a highly reflective coating consisting of $45 \lambda/4$ thick dielectrical layers (Ta_2O_5 and SiO_2) with alternating refractive indexes of $n_1 = 2.041$ and $n_2 = 1.455$ respectively.

The reflectivity of each mirror is about 99.9997% at the Cs D_2 line (852 nm), resulting in a cavity finesse of $\mathcal{F} \approx 1 \times 10^6$, see Section 1.3.1.

Cavity setup and its properties

The schematic view of the cavity, integrated with both the MOT and the DT is illustrated in Figure 1.13. The mirrors are glued onto shear piezoelectric actuators (PZTs) (PI Ceramic, $6 \times 6 \times 1$ mm) for tuning the cavity length and thereby the cavity resonance frequency over 1.5 free spectral ranges. The cavity is assembled on a specially designed cavity holder, which allows us to adjust the position of the cavity inside the glass cell with respect to the optical conveyor belt.

Cavity volume The cavity has a mirror separation of $L = 156 \mu\text{m}$, supporting the TEM_{00} Gaussian mode with the following distribution of the field amplitude

$$\psi(x, y, z) = \frac{w(z)}{w_0} \exp\left(-\frac{x^2 + y^2}{w_z^2}\right) \sin\left(\frac{2\pi z}{\lambda}\right), \quad (1.4)$$

where

$$\begin{aligned} w^2(z) &= w_0^2 \left(1 + z^2/z_0^2\right), \\ z_0 &= \pi w_0^2/\lambda. \end{aligned}$$

Here, w_0 is the waist of the field mode, x y and z are the spatial coordinates (see Figure 1.13), and λ is the wavelength of the cavity field. The volume of the cavity mode is ob-

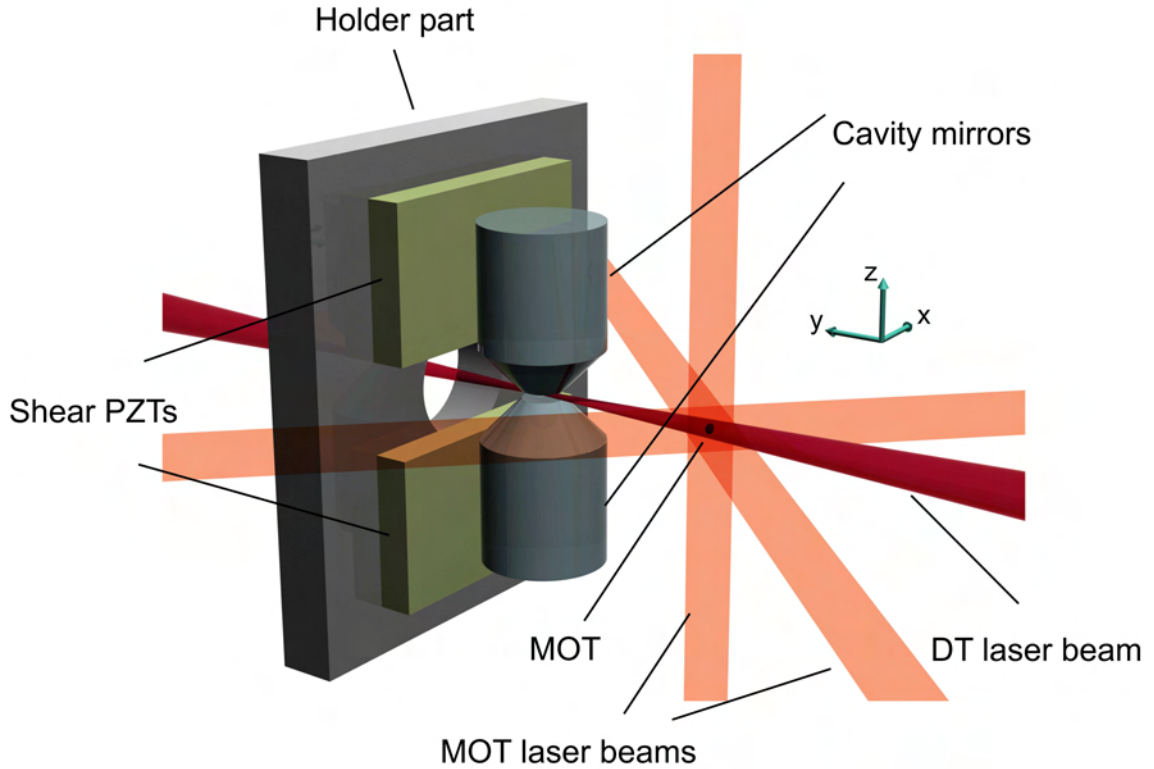


Figure 1.13: Geometrical configuration of cavity, MOT and DT. Atoms loaded into the MOT are transferred to the DT and delivered into the mode of the resonator, placed 4.6 mm away from the MOT centre. The coned form of the cavity mirrors insures better clearance for the MOT laser beams. The cavity is glued to the shear PZT, controlling the distance between mirrors.

tained by integrating $|\psi(x, y, z)|^2$ over the spatial coordinates and equals to $V = L \pi w_0^2/4$. Knowing the expression for the waist w_0 in terms of L and R

$$w_0 = \sqrt{\frac{\lambda}{\pi} \sqrt{\frac{L}{2} \left(R - \frac{L}{2} \right)}},$$

the resulting mode volume is equal to

$$V = \frac{\lambda}{8} \sqrt{L^3 (2R - L)} \approx 10^5 \times \lambda^3 \approx 66 \times 10^3 \mu\text{m}.$$

Cavity Finesse The cavity Finesse has been measured by the cavity ring down method [25] and equals $\mathcal{F} = (1.2 \pm 0.1) \times 10^6$. The finesse characterizes the quality of the resonator and indicates how many times a photon bounces on average between cavity mirrors until it gets lost: The 1/e lifetime of a photon is given by $\tau = \mathcal{F}L/(\pi c)$ and corresponds to the

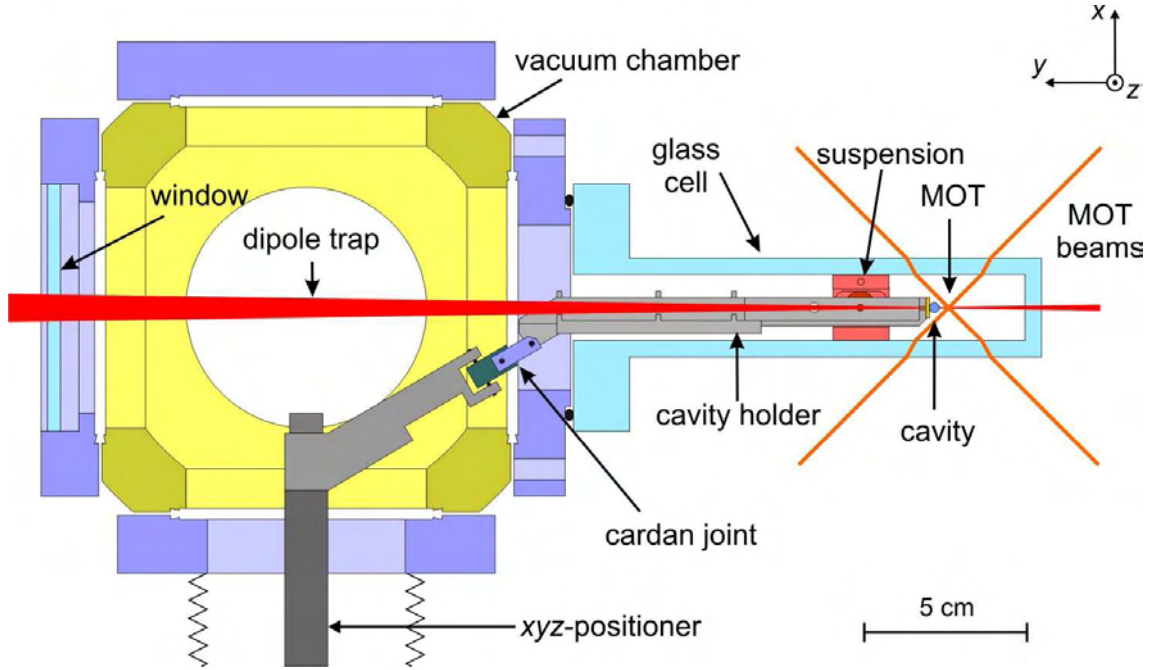


Figure 1.14: Schematics of the cavity holder inside the glass cell (top view). The adjustable cavity holder enables the alignment of the cavity position in the glass cell relative to the position of the MOT with the micrometer-scale precision. The resonator is placed about 4.6 mm away from the position of the MOT.

photon loss rate of 2κ , where $2\kappa/2\pi = 0.86$ MHz is the full width at half maximum of the cavity resonance.

A photon leaks from the cavity mode either through absorption and scattering off the mirror surface, or due to the finite mirror transmission. Our mirrors have a transmission of $T = (0.6 \pm 0.1)$ ppm, and the losses due to absorption and scattering are $A = (2 \pm 0.2)$ ppm⁷, which determine the value of the finesse ($\mathcal{F} = \pi/(A + T)$). The information about the atom-field interaction is carried by the transmitted photons only, constituting a fraction $T/A \approx 0.3$ of all photons leaving the cavity.

Cavity position The cavity is assembled on a specially designed cavity holder, placed inside the glass cell on a short bellows, see Figure 1.14. It is connected via a cardan joint to a 3D-positioner, consisting of a XY-manipulator (Thermionic Northwest, XY-B450/T275-1.39) and a Z-feedthrough (Thermionics Northwest, FLMM133). This combination allows us to adjust the cavity position with a precision of $5 \mu\text{m}$ relative to the DT axis.

In order to locate the cavity mode, we transport around 40 atoms having a broad position distribution along the DT axis towards the cavity mode by a distance corresponding to an initial guess of the separation between MOT and cavity mode. In the cavity mode we induce loss of atoms by heating them with the intra-cavity lock laser. Comparing CCD

⁷The method to measure T and A is described in [53, 54, 25].

pictures taken initially and after transporting back the atoms, we determine the position where atoms have been heated out. By tilting the DT horizontally, transverse to its axis, and looking for maximum atom loss, we can also locate the centre of the cavity mode along the x -axis [25].

1.3.2 Stabilizing the resonance frequency of the cavity

Cavity-QED experiments require precise control of the resonance frequency of the cavity relative to the atomic transition frequency. In order to keep the cavity resonance frequency stable within its linewidth, the cavity length must be controlled to better than $\delta L \leq \lambda/(2\mathcal{F}) = 0.4$ pm in our case. During the entire experimental procedure it is therefore necessary to actively stabilize the cavity length against acoustic vibrations and thermal drifts.

There are two major experimental issues to be considered: First, there is only marginal vibration isolation provided by the bellows. Second, switching the laser beams of the DT causes thermal expansion of the cavity mirror assembly due to residual absorption. As a consequence, the unstabilized cavity resonance frequency drifts with an initial rate of about 2×10^5 linewidths per second within the first 300 ms after the DT has been switched on or off. The corresponding servo loop therefore uses optimizations such as a double integrator, cross-feedback, and a notch filter compensating a mechanical resonance of the PZTs, and has a feedback bandwidth of about 10 kHz⁸.

Stabilizing laser

We use an auxiliary far blue-detuned laser (“lock laser”) at $\lambda_1 = 840$ nm for frequency stabilization of the resonator. The choice of this wavelength is determined by the interplay of two contradictory criteria: On the one hand, the presence of the lock laser light inside the cavity mode must not disturb the intended realization of the coherent interaction between a single atom and the cavity field. Since an atom would scatter the lock laser light with the rate proportional to $1/\Delta^2$, it is favorable to set Δ as large as possible (here Δ stands for the detuning of the lock laser frequency from the atomic transition). On the other hand, in order to ensure the mutual stability between the frequency of the probe laser and cavity resonance, the cavity finesse at the lock laser wavelength should not be significantly smaller than at the wavelength of the probe laser. At 840 nm, the typical lock laser power required for the cavity stabilization results in an intra-cavity scattering rate of about 40 s^{-1} – comparable with the DT scattering rate, and the finesse at this wavelength has been measured to be $\mathcal{F}_1 \approx 0.5 \times 10^6$ [25] – only a factor of two smaller than at 852 nm.

Our locking scheme for the stabilization of the high-finesse cavity [55, 25] is similar to the one presented in [56]. Its main elements are schematically depicted in Figure 1.15. Because of the absence of easily accessible atomic frequency references at $\lambda_1 = 840$ nm, the lock laser itself is stabilized onto an auxiliary cavity, which transfers the frequency stability of the probe laser to the lock laser. The error signals for all servo loops are based on the Pound-Drever-Hall (PDH) method [57].

⁸Details will be described in the thesis of T. Kampschulte.

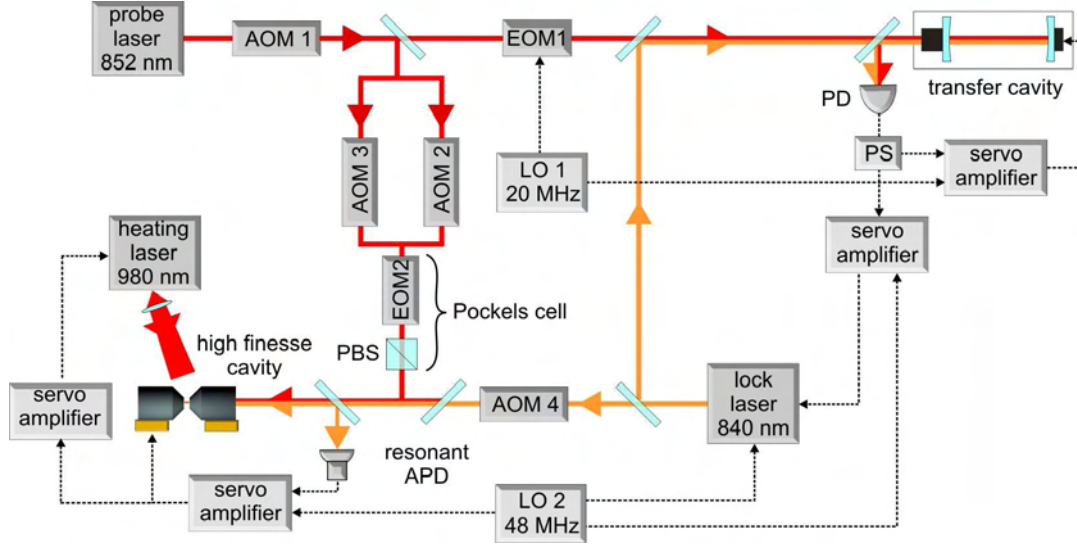


Figure 1.15: Frequency stabilization of the high-finesse cavity. Using a transfer cavity and a lock laser, the stability of the probe laser, which is stabilized to a caesium polarization spectroscopy, is transferred to the high-finesse cavity. AOM: acousto-optic modulator, EOM: electro-optic modulator, PD: photodiode, APD: avalanche photodiode, LO: local oscillator, PS: RF power splitter, and PBS: polarization beam splitter. The three servo loops are based on the PDH method.

The acousto-optic modulators (AOM 1-4 in Figure 1.15) allow independent control of the probe-cavity detuning and probe-atom detuning. In the measurement of normal-mode splitting, presented in Chapter 3, the probe laser is switched between the $F = 4 \rightarrow F' = 5$ transition and the $F = 4 \rightarrow F' = 4$ transition, which have a frequency separation of about 300 MHz. In order to enable such frequency change we split the probe laser beam into two parts, and send each beam through the AOM (AOM 2 and 3 in Figure 1.15) in a double pass configuration with an appropriate central frequency.

Moreover, in the normal-mode splitting measurement we also sweep the cavity resonance frequency continuously over about 300 MHz. Since the typical bandwidth of the AOM lies in the range of 40-80 MHz, this sweep cannot be done with an AOM in a double pass configuration. We therefore operate the AOM 4 in the quadruple pass configuration.

Although the cavity resonance at 840 nm is stabilized onto the lock laser, we still observe drifts of the cavity resonance frequency at 852 nm with respect to the probe laser frequency on a timescale of several seconds, see Reference [25]. This residual frequency deviation is caused by different temperature dependencies of the effective penetration depths of the two wavelengths into the mirror coatings. In order to compensate for this differential drift, we scan the cavity resonance over the probe laser frequency using AOM 2 and record a transmission spectrum of the cavity. Then, we determine the AOM control voltage which corresponds to the maximum transmission of the probe laser, and use this value during the following experimental cycle.

The optical path of the probe laser before it is injected into the cavity mode has a length of several meters. Temperature drifts inside the laboratory therefore cause a

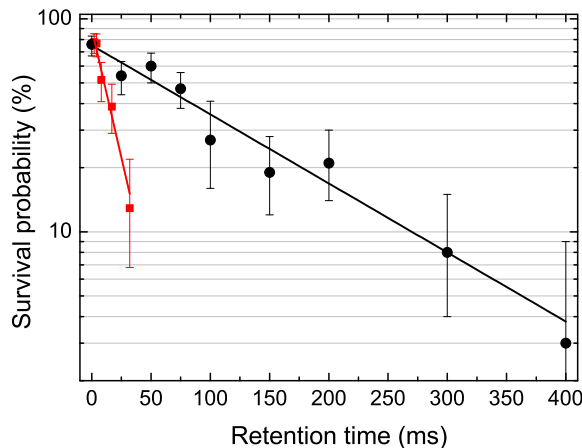


Figure 1.16: Atomic survival probability as a function of the intra-cavity retention time when the probe laser is switched off. The black circles indicate the measurement performed with the current improved design of the stabilization servo loop, resulting in a $1/e$ lifetime of 134 ms. The red squares are obtained with an old setup, yielding a lifetime of about 18 ms.

change of the coupling efficiency and the intra-cavity intensity of the probe laser light. In order to compensate for this change, we scan the control voltage of EOM 2 (which in combination with the consecutive PBS acts as a Pockels cell, see Figure 1.15) and record the corresponding transmission signal. We then determine the control voltage of the EOM 2, which corresponds to the desired transmission level, and set this voltage for the following experiment.

In order to compensate for large changes of the cavity length exceeding the tuning range of the piezoelectric actuators, caused by long term temperature variations, we heat the cavity using a multimode “heating laser” at 980 nm and a power of up to 400 mW. Since we cannot directly measure the temperature of the cavity mirrors, we use the voltage applied to the piezoelectric actuators as an error signal. This signal is fed back onto the power of the heating laser in a slow servo loop, thus keeping the PZT offset voltage close to zero.

A relevant test for the quality of the cavity frequency stabilization is the lifetime of the atoms, held by the DT inside the cavity mode, and exposed to the intra-cavity standing wave of the lock laser. The mutual fluctuations between the lock laser frequency and the resonance frequency of the cavity translate into intensity variations of the intra-cavity lock laser standing wave, which in turn causes parametric excitation and heats the atoms out of the DT.

The dots in Figure 1.16 show the measured survival probability as a function of retention time inside the cavity mode for the current cavity stabilization setup. Each point is the result of about 40 single-atom experiments. As a comparison, the squares show the result of similar measurement, performed with an old stabilization setup, where double in-

tegrator, cross-feedback, and the heating laser were not yet implemented. In the current configuration of the cavity stabilization setup the lifetime of atoms is more than a factor of 7 larger than in our former setup, indicating the improved stability of the cavity resonance with respect to the frequency of the lock laser.

1.3.3 Transmission detection

As discussed in Chapter 2 and 3, the transmission of the probe laser beam is an indicator of the strength and the dynamics of the atom-cavity interaction, and is also used to detect the atomic state. Since both the lock laser and the probe laser beams share the same TEM₀₀ transverse cavity mode profile, we need to separate them at the output of the cavity.

The sketch of the detection setup is presented in Figure 1.17. Both the stabilization and the lock laser beams are coupled out from the same optical fiber. They are in mutually orthogonal polarization states. The back reflection of the lock laser beam from the cavity is directed on a home-made APD, resonantly-amplified at the amplifier, tuned to the PDH modulation frequency of the lock laser. The detected lock laser power of about 250 nW results in an error signal with the signal-to-noise ratio of about 5.

A specially designed mode-matching telescope T allows us to couple both probe and lock laser into the mode of the resonator with a geometrical mode matching of about 40 %. At the output of the cavity we installed a removable beam splitter, which redirects one half of the transmitted light onto a CCD camera, allowing the identification of the relative occupation of different transversal modes of the resonator. The beams are then separated on a diffraction grating, which is installed almost at the blaze angle of 37° with respect to the beams. The measured dispersion of 1.5 mrad nm^{-1} allows us to separate the probe and lock beams by standard mirrors after at a distance of 40 cm from the grating. The reflection efficiency is equal to $\eta_{\text{grating}} = 45\%$ for the probe laser beam.

The lock laser beam is detected by an APD and a CCD camera, as it is depicted in Figure 1.17. From the transmission signal of the lock laser we deduce the relative fluctuation of the cavity resonance frequency with respect to the lock laser frequency.

The beam of the probe laser is filtered with an interference filter (Dr. Hugo Anders), which suppresses the light at 836 nm and 1030 nm wavelengths by a factor of 10^{-4} , and transmits $\eta_{\text{filter}} = 77\%$ of the probe light. We subsequently filter off the remaining scattered light by a pinhole.

For the detection of the probe beam transmission two different detectors are installed. Depending on the situation we choose one of them using a mirror on a flip mount. In order to tune the frequency of the lock laser to the probe frequency, we employ an avalanche photodiode detector (PerkinElmer, C30902S), followed by a home-made transimpedance amplifier (depicted as APD2 in Figure 1.17). For the very low probe power ($\sim 10 \text{ fW}$) we typically detect during the experiments, a fiber-coupled single photon counting module (SPCM, PerkinElmer, SPCM-AQR-12-F) is employed. It has a total measured quantum efficiency (including the transmission of the fiber) of about $\eta_{\text{SPCM}} = 18\%$ and the dark current rate of less than $500 \text{ Counts s}^{-1}$. The total detection efficiency of the probe light,

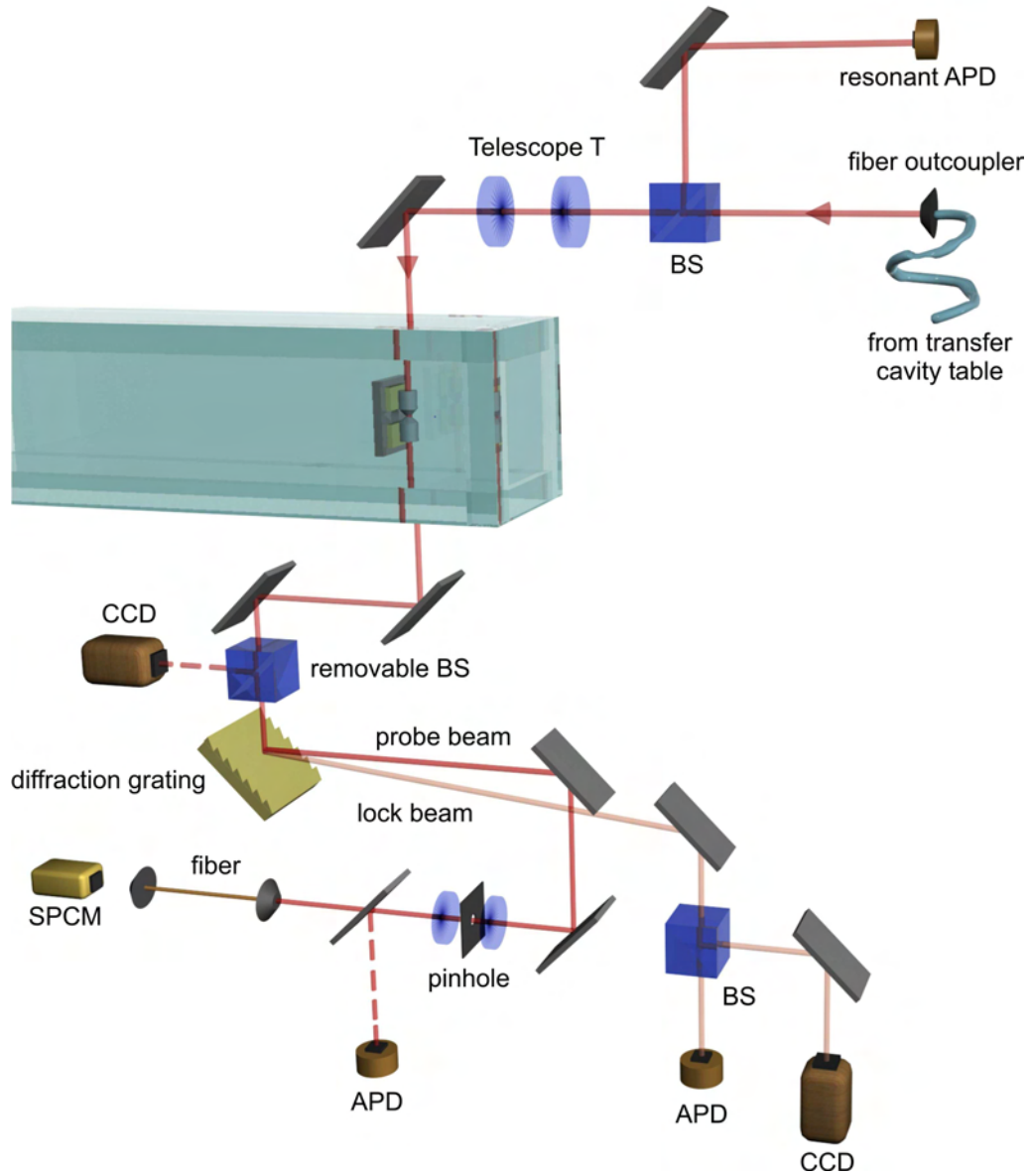


Figure 1.17: The sketch of the detection setup. The probe and the lock laser beams are coupled to the mode of the cavity using the telescope T1. We separate the probe and lock laser beams at the cavity output by the diffraction grating. With the APD and SPCM we detect the transmission of the probe laser beam. The CCD cameras allows to monitor and discriminate between different transversal modes of the cavity.

including the losses of the cavity mirrors, is equal to

$$\eta_{\text{total}} = \frac{T}{(T + A)} \cdot \eta_{\text{optic}} \cdot \eta_{\text{grating}} \cdot \eta_{\text{filter}} \cdot \eta_{\text{SPCM}} \approx 1.3\% , \quad (1.5)$$

where $\eta_{\text{optic}} = 90\%$ is the estimated transmission efficiency of the all optical elements⁹ in the beam path of the probe laser between the cavity output and the SPCM.

⁹Apart from interference filter and diffraction grating.

Chapter 2

Atom-cavity system in the strong coupling regime

The most basic example of light-matter interaction is a single atom interacting with a single photon. This single-atom-single-photon system permits the study of the effects of quantum electrodynamics at the fundamental level. Moreover, by gaining full control over such a system it might become conceivable to use them in the emerging fields of quantum information and quantum communication.

The essential requirement for these applications is the availability of strong atom-photon coupling. This can be achieved if a light field is confined inside the mode of a high-quality resonator. In this case a single atom, placed inside the mode, can coherently exchange energy with the mode field at a rate exceeding both the spontaneous decay rate of the atomic excited state, and photon leakage rate from the resonator mode. In this case the atom-cavity system is in the so-called strong coupling regime.

The first realization of strong coupling between a single atom and a resonator field was reported for flying Rydberg atoms interacting with the microwave field of the resonator cooled down to a cryogenic temperature [58]. Later, in the optical domain, strong atom-cavity interaction was realized with a dilute beam of atoms [59]. Since the development of single atom manipulation techniques [12, 60, 46], worldwide several groups have been able to strongly couple a single or several trapped atoms to the resonator mode [61, 62, 63, 64].

The theoretical background of such systems has been a subject of thorough investigation for the last six decades. In this chapter I will refer to the most relevant results, which are elaborately described in [35, 65, 66], without providing detailed derivations. I will start with the Jaynes-Cummings model, describing the basic physics of coherent atom-photon interaction. Further, dissipation of energy by the environment will be incorporated by expanding the dissipation-free situation to a so-called master equation model.

After providing the theoretical background, I will present experiments demonstrating deterministic coupling of a single and two atoms to the mode of the cavity field by means of an optical conveyor belt. The coupling strength between an atom and the cavity field is inferred using two different methods: On the one hand, the atom-field coupling is detected by observing the leakage of the light from the resonator. In an alternative method,

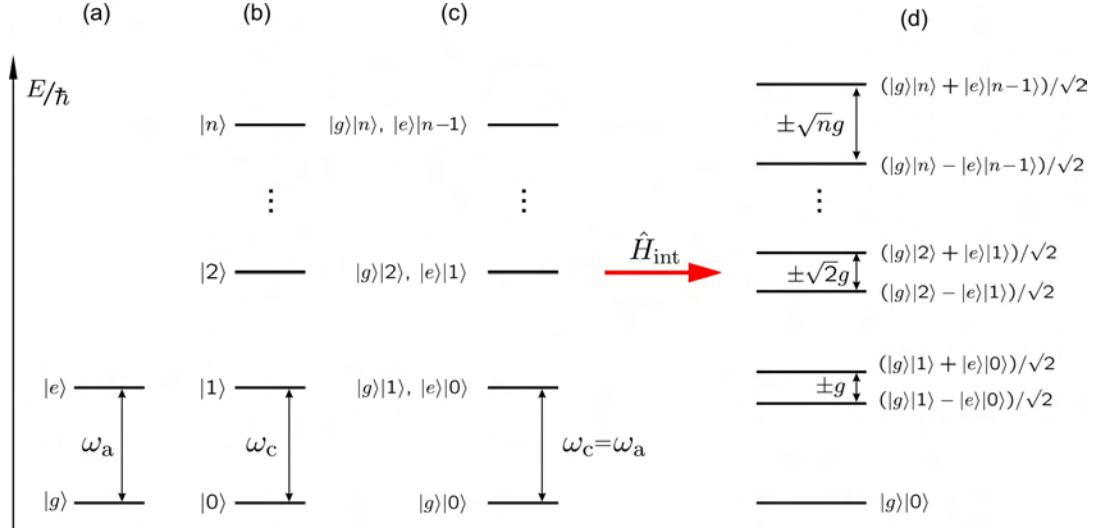


Figure 2.1: Energy levels in the Jaynes-Cummings model. Energy levels of: A free two-level atom (a), a quantized electromagnetic field (b), a non-interacting atom-field system (c), a coupled atom-field system (d).

presented in Section 2.4, the interaction is deduced from the final state of an atom after its interaction with the cavity field.

2.1 The Jaynes-Cummings model

The Jaynes-Cummings model provides a basic understanding of a system consisting of a two-level atom interacting with a quantized electromagnetic field of a cavity [67, 66]. Originally this model was developed to describe the interaction of an atom with a single mode of the electromagnetic field in free space, but without loss of generality it can be extended to the case of an atom interacting with an electromagnetic field enhanced by a resonator.

In this model the center-of-mass atomic motion is neglected and the atom, as well as the electromagnetic field, are assumed to be dissipation-free. The Hamiltonian of the interacting atom-cavity system can be decomposed into three parts

$$\hat{H}_{\text{JC}} = \hat{H}_{\text{a}} + \hat{H}_{\text{c}} + \hat{H}_{\text{int}},$$

where \hat{H}_{a} and \hat{H}_{c} are the contributions from a free atom and quantized electromagnetic field, respectively. \hat{H}_{int} denotes the atom-cavity interaction part of the Hamiltonian. The Hamiltonian of a two-level atom \hat{H}_{a} has the form

$$\hat{H}_{\text{a}} = \hbar\omega_{\text{a}}|e\rangle\langle e|,$$

where ω_{a} is the angular frequency of the atomic transition, and $|e\rangle$ is the excited state of the atom. The corresponding energy states of the atom are displayed in Figure 2.1 (a).

The Hamiltonian of the electromagnetic field reads

$$\hat{H}_c = \hbar\omega_c \left(\hat{a}^\dagger \hat{a} + 1/2 \right),$$

where ω_c is the angular frequency of the electromagnetic field, \hat{a}^\dagger and \hat{a} are the photon creation and annihilation operators, respectively. The corresponding energy states are presented in Figure 2.1 (b).

In the electric dipole approximation the interaction Hamiltonian between an atom and the field is given by the product of the atomic dipole operator $\hat{\mathbf{D}}$ and the field operator of the intracavity photons $\hat{\mathbf{E}}_c$: $\hat{H}_{\text{int}} = -\hat{\mathbf{D}} \cdot \hat{\mathbf{E}}_c$. The atomic dipole operator is equal to:

$$\hat{\mathbf{D}} = \vec{\mathbf{d}} (\hat{\sigma}_+ + \hat{\sigma}_-) \quad (2.1)$$

where $\vec{\mathbf{d}}$ is the dipole matrix element of the atomic transition, $\hat{\sigma}_+ = |e\rangle\langle g|$ and $\hat{\sigma}_- = |g\rangle\langle e|$ are the rising and the lowering operators, respectively. The operator of the electromagnetic field is given by

$$\hat{\mathbf{E}}_c = \sqrt{\frac{\hbar\omega_c}{2\epsilon_0 V}} \vec{\epsilon}_c (\hat{a}^\dagger + \hat{a}) \quad (2.2)$$

where ϵ_0 is the vacuum permittivity, V is the effective cavity mode volume and $\vec{\epsilon}_c$ is the polarization of the cavity field. Combining the expressions in Equation 2.1 and Equation 2.2, the interaction part of the Hamiltonian then reads

$$\hat{H}_{\text{int}} = \hbar g_0 (\hat{a} \hat{\sigma}_+ + \hat{a}^\dagger \hat{\sigma}_-).$$

Here the rotating wave approximation has been applied, eliminating highly improbable terms proportional to $\hat{a} \hat{\sigma}_-$ and $\hat{a}^\dagger \hat{\sigma}_+$. These terms violate energy conservation and contribute to the system dynamics by the virtual processes only, which have negligible contribution if $g_0 \ll \omega_c, \omega_a$. The coupling strength g_0 is defined as

$$g_0 = d \sqrt{\frac{\omega_c}{2\hbar\epsilon_0 V}}. \quad (2.3)$$

So far, the spatial variation of the electromagnetic field was neglected. Taking this into account, the coupling strength g of the Fabry-Perot resonator has the following form

$$g = g_0 \times \psi(x, y, z), \quad (2.4)$$

where $\psi(x, y, z)$ is taken from Equation 1.4, and x , y and z are the spatial coordinates inside the cavity mode. This equation considers the fundamental TEM₀₀ mode of the cavity, having a sin-like variation along the cavity axis (z axis), and a Gaussian transversal profile.

The eigenstates of the Hamiltonian \hat{H}_{JC} have the following form

$$\begin{aligned} |+\rangle &= \sin(\theta) |g, 1\rangle + \cos(\theta) |e, 0\rangle \\ |-\rangle &= \cos(\theta) |g, 1\rangle - \sin(\theta) |e, 0\rangle, \end{aligned}$$

where $|g, 1\rangle$ and $|e, 0\rangle$ denote the states of non-interacting atom-cavity system, i.e. with the atom in the ground state and one photon in the cavity field and an atom in the excited state and no photon inside the cavity, respectively. The mixing angle θ is defined as

$$\tan(2\theta) = -\frac{2 \cdot g}{(\omega_c - \omega_a)}.$$

The energy spectrum of the eigenstates of the total Hamiltonian differs from that of the bare states. Figure 2.1 (c) and (d) illustrates it for the resonant case, i.e. $\omega_a = \omega_c$. Due to the interaction term of the Hamiltonian \hat{H}_{int} the degeneracy of the bare states is lifted, and the corresponding splitting between the resulting dressed states is equal to $2\sqrt{n} \times g$, where n is the number of excitations inside the system.

Figure 2.2 shows calculated energies of the lowest doublet from Figure 2.1 (d) when the frequency of electromagnetic radiation is varied around the atomic resonance. For this example the coupling strength is equal to $g/2\pi = 1$ MHz.

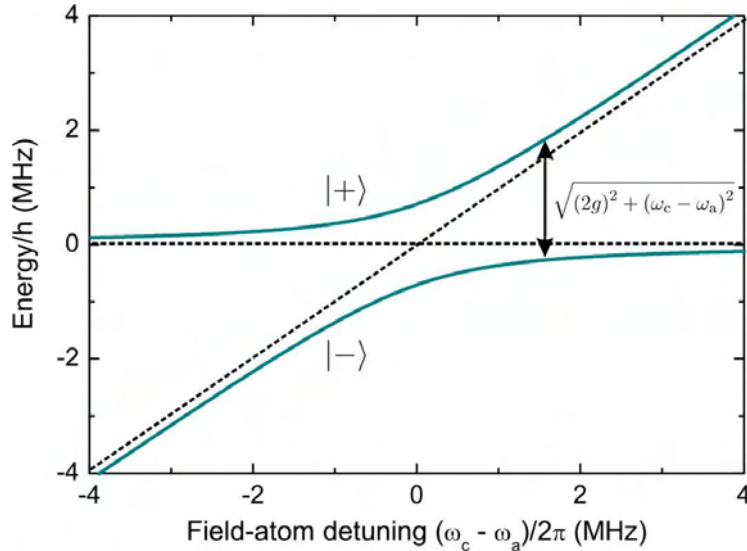


Figure 2.2: Energies of lowest-lying pair of states from Figure 2.1 (d). The corresponding uncoupled states are displayed by the dashed lines.

2.2 The master equation approach

The Jaynes-Cummings model gives a precise result for the energies of the emerged eigenstates of the interacting atom-cavity system. This model, however, neglects the dissipative interaction with the environment, i.e. the leakage of the cavity field due to imperfect mirrors and the spontaneous emission from the excited atomic state. In real physical systems, these dissipation channels cannot be neglected.

An appropriate formalism, accounting for the coupling of the atom-cavity system to the environment, is provided by the master equation. It predicts the dynamics of the system

and gives a precise information about the probability amplitudes of the corresponding dressed state of the coupled atom-cavity system.

Here we consider a single atom interacting with the cavity field and driven by the external laser, coupled into the cavity mode. The Hamiltonian of the coupled atom-cavity system interacting with the environment is given by

$$\hat{H}_{\text{tot}} = \hat{H}_s + \hat{H}_{\text{env}} + \hat{H}_{s+\text{env}},$$

where

$$\hat{H}_s = \hbar(\omega_a - \omega_p) \hat{\sigma}_+ \hat{\sigma}_- + \hbar(\omega_c - \omega_p) \hat{a}^\dagger \hat{a} + \hbar g (\hat{a} \hat{\sigma}_+ + \hat{a}^\dagger \hat{\sigma}_-) + \hbar \epsilon (\hat{a} + \hat{a}^\dagger),$$

acts on the system only. Here ϵ is the amplitude of the driving probe laser field and ω_p is the angular frequency of the probe laser. \hat{H}_{env} governs the evolution of the environment and $\hat{H}_{s+\text{env}}$ accounts for the interaction between the system and the environment. The total Hamiltonian \hat{H}_{tot} operates on the Hilbert space $\mathcal{H} = \mathcal{H}_s \otimes \mathcal{H}_{\text{env}}$, where \mathcal{H}_s (\mathcal{H}_{env}) denotes the Hilbert space of the system (environment).

The Heisenberg equation of motion for the density operator $\hat{\chi}$ of the total system reads

$$\frac{d}{dt} \hat{\chi} = \frac{1}{i\hbar} [\hat{H}_{\text{tot}}, \hat{\chi}].$$

Assuming that the environment is a collection of harmonic oscillators, each coupled weakly to the system, and applying the Born-Markoff approximation, which implies that the correlation time of the environment is much shorter than the timescales associated with the evolution of the system, the master equation can be derived which describes the evolution of the system's density operator $\hat{\rho}_s$. The system's density operator is obtained by tracing $\hat{\chi}$ over the states of the environment $\hat{\rho}_s = \text{tr}[\hat{\chi}]_{\text{env}}$. The derivation of the master equation is provided in Reference [65]. The result is given by

$$\frac{d}{dt} \hat{\rho}_s = \frac{1}{i\hbar} [\hat{H}_s, \hat{\rho}_s] + \hat{R}. \quad (2.5)$$

The first term on the right side describes the dissipation-free evolution of the density operator. The operator \hat{R} accounts for the interaction of atom-cavity system with the environment through the dissipation channels:

$$\hat{R} = \kappa \left(2\hat{a}\hat{\rho}_s\hat{a}^\dagger - \hat{a}^\dagger\hat{a}\hat{\rho}_s - \hat{\rho}_s\hat{a}^\dagger\hat{a} \right) + \frac{\Gamma}{2} \left(2\hat{\sigma}_-\hat{\rho}_s\hat{\sigma}_+ - \hat{\sigma}_+\hat{\sigma}_-\hat{\rho}_s - \hat{\rho}_s\hat{\sigma}_+\hat{\sigma}_- \right),$$

where κ is the cavity field decay rate and Γ is the decay rate of the excited state of the atom.

Figure 2.3 (b) shows the steady-state solution of Equation 2.5, i.e. $\frac{d}{dt} \hat{\rho}_s \equiv 0$, for a two-level atom interacting with the cavity field. The number of intra-cavity photons n_p is shown as a function of the cavity-atom detuning $\Delta_c = \omega_c - \omega_a$ and the probe-atom detuning $\Delta_p = \omega_p - \omega_a$ when a single atom is coupled to the cavity field.

For this calculation, the parameters reflecting our experimental conditions were used

$$(g_0, \kappa, \Gamma) = 2\pi \times (12, 0.43, 5.2) \text{ MHz},$$

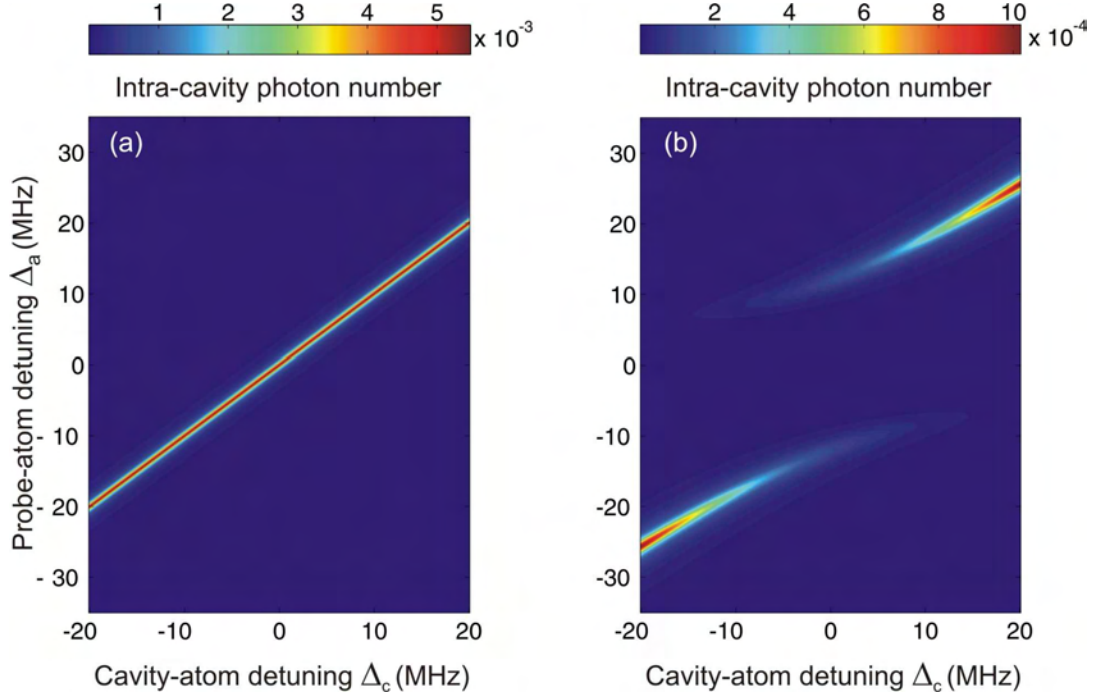


Figure 2.3: The calculated intra-cavity photon number as a function of the cavity-atom detuning Δ_c and the probe-atom detuning Δ_p for two different cases. (a) No atom is present inside the cavity. The non-zero photon number is observed for $\Delta_c = \Delta_p$ and has a half width at half maximum of κ along the cut $\Delta_c = \text{const}$. (b) The coupling of a single atom to the cavity mode causes two dressed states to occur. The splitting between the states (along the cut $\Delta_c = \text{const}$) is equal to $\sqrt{(\Delta_c)^2 + (2g)^2}$. In both cases the driving probe laser is weak, implying that the system is in the weak excitation limit.

where g_0 is the maximal expected coupling strength for the the π -transition $|F = 4, m_F = 4\rangle \rightarrow |F' = 4, m_{F'} = 4\rangle$, Γ is the natural linewidth of the Cs D₂-transition, and κ is the measured cavity field decay rate. The strength of the probe laser field is such that the system is in the weak excitation regime, i.e. the number of intra-cavity photons is much smaller than the saturation photon number $n_{\text{st}} = \Gamma^2/(8g_0^2)$. In this regime the response of the coupled atom-cavity system is linear with respect to the probe laser power, and the atomic scattering rate is much smaller than Γ .

The signature of the dressed states is visible in the map of the intra-cavity photon number. The splitting between the states at the fixed cavity frequency is equal to $\sqrt{(\Delta_c)^2 + (2g)^2}$. In the resonant case where $\Delta_c = 0$, the peaks of equal height are split by twice the coupling strength g and the full width at half maximum (FWHM) of each peak is equal to $\kappa + \Gamma/2$. This splitting is referred to in literature as vacuum Rabi or normal-mode splitting [13, 14]. In order to observe this splitting, the coupling strength g should exceed the spontaneous emission rate Γ and the cavity linewidth κ , $g > \kappa, \Gamma/2$. This implies that the system should be in the strong coupling regime, i.e. $g^2/\kappa\Gamma > 1$.

When the cavity is tuned out of resonance with the atomic transition, $\Delta_c \neq 0$, the

situation is different: The width and the height of the peaks of the photon number are determined by the ratio between contributions from the atomic and photonic part to the corresponding dressed state.

For comparison, Figure 2.3 (a) shows the calculated intra-cavity photon number when no atom is coupled to the cavity. In this trivial case, a single peak with the FWHM equal to 2κ is present for all cavity frequencies when the probe laser is tuned in resonance with the cavity. Note that color scale in Figure 2.3 (a) is more than a factor of five larger than that in Figure 2.3 (b) for the same intensity of the driving probe laser.

In order to detect the atom-cavity coupling in the experiment we typically measure the transmission of a weak probe laser driving the system. As was pointed out in Reference [25], in the case of a lossless cavity the photon count rate of the probe laser at the output of the cavity is equal $2\kappa \times n_p$, i.e. the change of the probe transmission signal implies the change of the intra-cavity photon number n_p .

2.3 Detection of atom-cavity coupling via cavity transmission

After introducing the theoretical background, here I will present the experimental characterization of the interaction between a single and two atoms and the cavity field via the cavity transmission.

2.3.1 Detection of a single atom inside the cavity

We first carry out the experiment with a single atom. The experiments start by preparing a single atom in the dipole trap using the number triggered loading technique, described in Reference [49]. We then image the atom fluorescence by illuminating it with three-dimensional optical molasses, tuned by several Γ to the red of the $F = 4 \rightarrow F' = 5$ transition. The position of the atom along the dipole trap axis is then determined from the fluorescence image with an uncertainty of 140 nm [12]. In the next step we transport the atoms along the dipole trap axis over 5 mm within 4 ms into the cavity.

In order to detect the atom-cavity interaction, we monitor the transmission of the probe laser while inserting the atom into the resonator. As it is outlined in Section 2.2, the presence of an atom in the cavity mode results in the drop of initially high transmission of the probe laser due to the interaction-induced normal mode splitting.

In all experiments, presented below, the cavity is tuned into resonance with the probe laser, i.e. $\Delta_c = \Delta_p$. Here, ω_a is the angular frequency of the AC-Stark shifted atomic $F = 4 \rightarrow F' = 5$ transition. The cavity and the probe laser are blue detuned from the atomic transition by $\Delta_c/2\pi \approx 24$ MHz. There exists theoretical work which predicts cooling in this regime, see Reference [68]. However, we found this particular value empirically by observing an increased lifetime of the atoms inside the cavity.

Figure 2.4 presents an example of a single experimental cycle. At time $t = 0$ the single photon counting module (SPCM), introduced in Chapter 1, is switched on. The background signal of about 1 counts/ms corresponds to the dark counts and the stray light detected by the SPCM. After 14 ms the probe laser beam is switched on, resulting in a photon count rate of 26 counts/ms, corresponding to a mean intra-cavity photon number of about 0.1.

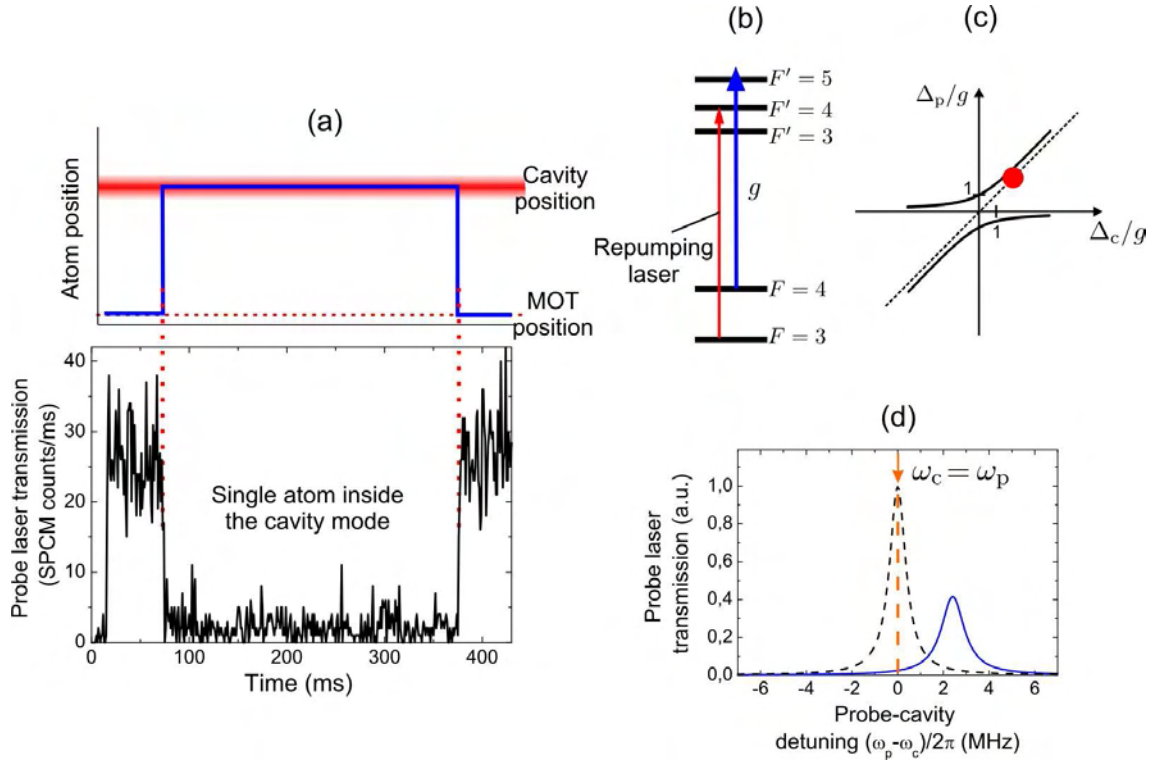


Figure 2.4: (a) Transmission signal versus time obtained in a single experimental run showing the case of continuous strong coupling. Upon placement of a single atom into the cavity mode the transmission drops to 5 % of its value for the empty cavity. After continuously observing the atom for 300 ms inside the cavity it is transported back to the position of the MOT. (b) Relevant energy states of the Cs D_2 line. (c) Schematic illustration of the energies of the coupled atom-cavity states (solid lines) and empty cavity state (dashed line). In this measurement the cavity resonance is blue detuned from the $F = 4 \rightarrow F' = 5$ transition by $\Delta_c/2\pi \approx 24$ MHz and $\Delta_p = 0$ which are shown as a red circle. (d) Calculated cavity transmission for empty cavity (dashed line), and for a single atom coupled to the cavity (solid line) as a function of probe-cavity detuning $\omega_p - \omega_c$ for our detuning Δ_c and $g/2\pi = 8$ MHz.

The saturation photon number for the maximal coupling strength $g/2\pi = 13$ MHz (see Section 2.3.2) is equal to $n_{\text{cr}} = 0.02$. However, for an empty cavity with the intra-cavity photon number of 0.1, the intra-cavity photon number and the scattering rate of an atom coupled to the cavity are smaller than n_{cr} and Γ , respectively, for any detuning Δ_c and any coupling strength g . This fact indicates that we are in the regime of weak excitation. At $t = 70$ ms the atom is inserted into the centre of the cavity mode, which causes the transmission of the probe laser to drop to 2 counts/ms. Subtracting the background count rate, the transmission drops down to approximately 5 % of its initial level. For our values of κ and Γ and the chosen value of Δ_c , the observed drop in the probe transmission indicates strong coupling of the atom to the field of the resonator mode. During the entire experimental cycle a repumping laser resonant with the $F = 3 \rightarrow F' = 4$ transition is

applied along the dipole trap axis. It transfers the atom back into the $F = 4$ state if it is off-resonantly pumped into the $F = 3$ state by the probe laser. The transmission remains at this level of 5 % while the atom resides in the cavity until we transport the atom back to the position of the MOT.

2.3.2 Simple model

In order to quantitatively analyze our measurements and to establish a relation between g and the observed average transmission, the physical system including a variation of g caused by internal and external dynamics of the atom is modelled. For this purpose the master equation of the coupled atom-cavity system is solved numerically [65]. All processes causing a variation of the coupling strength g are slow compared to the decay time $1/\kappa$ of the cavity field. Therefore, the cavity transmission at any moment is determined by the instantaneous coupling strength. Since g is time-dependent and the cavity transmission is a non-linear function of g , I simulate the measured average transmission level by first calculating the transmission levels corresponding to all possible values of g , and then computing the weighted average over these levels.

Internal dynamics

The internal dynamics of the atom is caused by its continuous scattering of photons while coupled to the cavity mode, which causes changes in the Zeeman sublevel occupation. Since the atom is not optically pumped into a specific m_F sublevel of the ground state $F = 4$, I assume a homogeneous distribution over all these states and average over the transmissions corresponding to the different m_F states.

As was discussed in Reference [25], our cavity mirrors feature a slight birefringence. Thus, the resonances show a polarization splitting of several linewidths and the cavity supports linear polarization modes only. For π -transitions from $F = 4$ to $F' = 5$ and for our parameters, the calculated coupling strength $g/2\pi$ ranges from 8 to 13 MHz for different m_F states. These values have to be compared to the dissipation rates of the coupled atom-cavity system. The field of the cavity decays at a rate of $\kappa/2\pi \approx 0.4$ MHz, and the excited state decay rate of a caesium atom is $\Gamma/2\pi = 5.2$ MHz. Since the condition $g \gg (\Gamma, \kappa)$ is satisfied the system operates in the strong coupling regime. The single atom cooperativity parameter $C_1 = g^2/(\kappa\Gamma)$, quantifying the coherent energy exchange versus dissipation rates, is expected to be on the order of 50.

External dynamics

The external dynamics is given by the motion of the atom in the trapping potential. A thermal Boltzmann energy distribution is assumed, which neglects modifications due to cavity QED effects, the multi-level atomic structure and technical noise which could lead to a non-thermal energy distribution [68]. Since our integration time is much longer than the heating and cooling timescales, our model allows to assign an effective temperature T corresponding to the time averaged energy $\langle E \rangle$ of the atom in the trap via $\langle E \rangle = 3k_B T$.

We take into account the variation of g and the variation of the AC-Stark shift, due to the dipole trap and the lock laser, caused by the oscillatory motion.

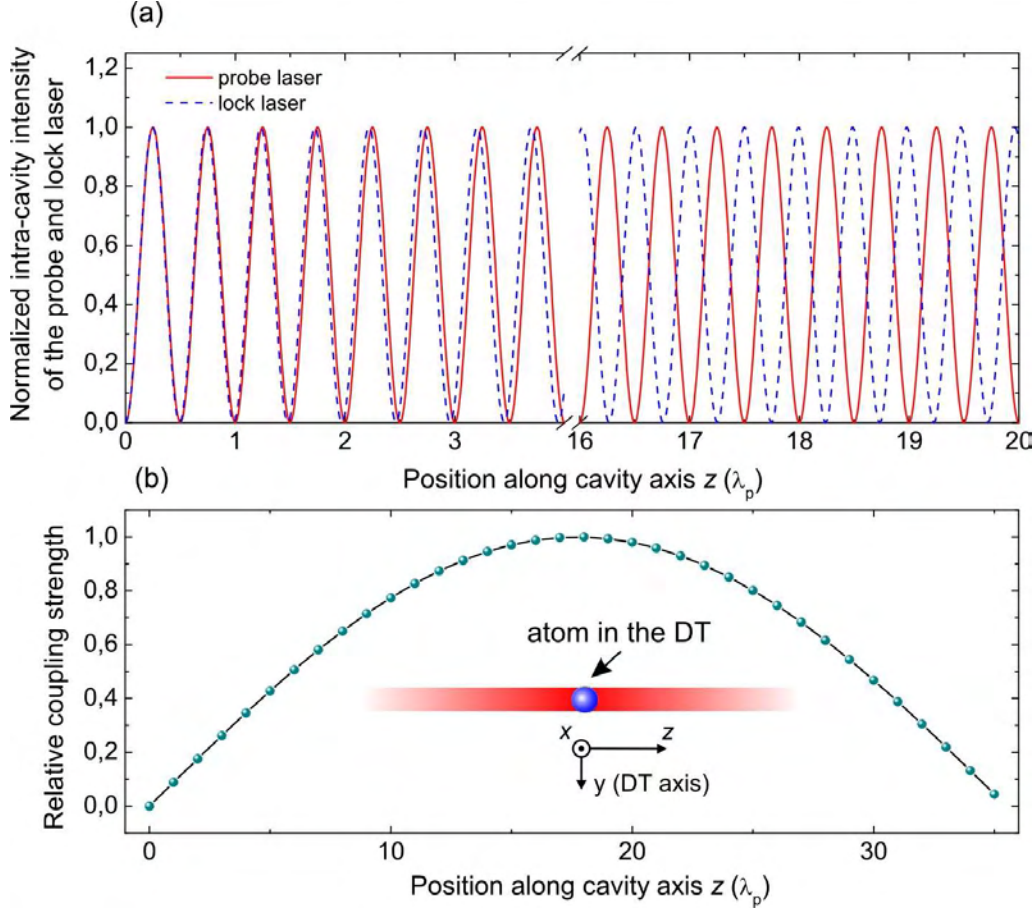


Figure 2.5: (a) Normalized probe (solid line) and lock laser (dashed line) intra-cavity intensities along the cavity axis (z axis). Due to different periodicities of the probe and lock laser standing waves, the coupling strength at the potential minima of the lock standing wave changes. (b) The calculated relative coupling strength as function of the position along the cavity axis. For this simple calculation the atom is assumed to have a zero temperature, residing at the nodes of the lock laser standing wave.

The spatial variation of the coupling strength g is identical to the spatial distribution of the probe laser field inside the cavity and is defined by the cavity mode profile, specified in Equation 2.4. The depth of the dipole potential due to the intra-cavity photon number of the probe laser in the case of the empty cavity ($n = 0.1$) is only about 30 μK at the centre of the cavity mode [69]. An atom coupled to the mode strongly reduces the photon number which further decreases this potential to values much lower than the atomic temperature and all other trapping potentials. I therefore neglect the effect of this potential.

The lock laser at $\lambda_l = 840$ nm, introduced in Chapter 1, which is used for the frequency stabilization of the cavity, forms a blue-detuned intra-cavity standing wave. Due to reso-

nant enhancement, the injected lock laser power of $0.4 \mu\text{W}$ creates a blue-detuned standing wave dipole potential with a height of about 0.3 mK , considerably higher than the atomic temperature. This potential depth corresponds to a maximum scattering rate of 40 s^{-1} . Since the lock and the probe laser share the same cavity mode, the transversal profile of the lock laser potential is almost the same as of the probe laser. In the longitudinal direction (along the z -axis), due to the difference in the wavelengths, the lock laser standing wave has different periodicity than the probe laser standing wave.

Figure 2.5 (a) shows the variation of normalized intra-cavity probe and lock laser intensities along the z -axis. Depending on the atomic position along the cavity axis, the coupling strength at potential minima of the lock laser standing wave changes from maximum to minimum over a length of $d_{\text{beat}}/2 = 15 \mu\text{m} (\approx 18\lambda_p)$. Figure 2.5 (b) shows the calculated relative coupling strength as a function of the lock laser potential well. For this simple calculation the atom is assumed to have a zero-temperature, i.e. a fixed position at the node of the lock laser standing wave. Note that the data presented in Figure 2.4 have been selected for strongest coupling and no hopping, i.e. the atom stays in the same potential well of the lock laser standing wave. In the model we the assumption is made, that the atom resides at a potential minimum coinciding with a maximum of g .

Along the x -axis, transverse to both dipole trap and cavity axis, the atom is weakly confined by the Gaussian profile of the dipole trap. Due to oscillations along this direction over several micrometers the atom experiences a variation of the AC-Stark shift and the coupling strength g . Along the z -axis the atom is well localized to several hundred nanometers by the lock laser standing wave with a potential height of $U/k_B \approx 0.3 \text{ mK}$. Along the dipole trap axis (y -axis) the variation of g is negligible and I consider the variation of the AC-Stark shift only.

In the numerical simulations the model temperature is used as a fit parameter. A temperature of about 0.17 mK reproduces our observed drop of the transmission to 5% . This result indicates a higher temperature than the typical 0.03 mK inside our dipole trap after molasses cooling, see Section 1.2.3, possibly due to different cooling and heating mechanisms inside the cavity.

2.3.3 Dynamics of the atom-cavity coupling strength

In the experiments we frequently observe strong variations of the transmission signal. A typical example is shown in Figure 2.6(a). We assume these variations are caused by hopping of atoms between different trapping sites along the cavity axis (z -axis): Due to the dynamic equilibrium between cooling and heating processes in the cavity, the atom can be heated out of one node of the blue-detuned lock laser standing wave and subsequently be cooled into a different node. Since the lock and probe laser standing waves have different periodicities, the coupling strength changes over a length of $d_{\text{beat}}/2 = 15 \mu\text{m}$, as discussed above and depicted in Figure 2.6(b). Therefore, the hopping of atoms along the z -axis can result in sudden strong changes of the atom-cavity coupling strength, leading to jumps of the transmission level.

We observe that the rate of these transmission variations seems to depend critically on a complex interplay between lock and probe laser intensities, probe-cavity detuning, and the

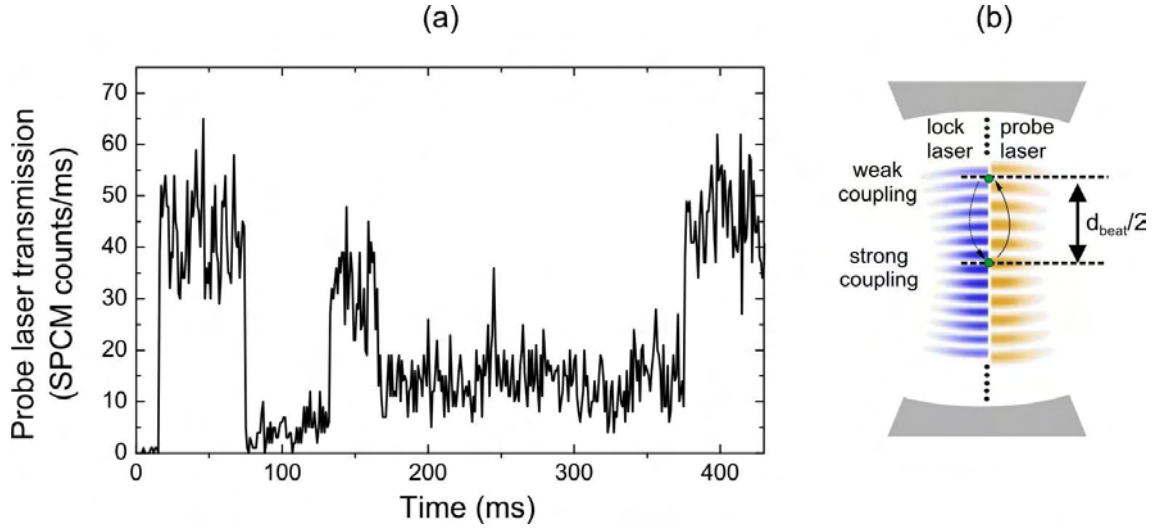


Figure 2.6: (a) Transmission signal of the probe laser beam through the cavity for the case of time-dependent coupling. (b) Due to jumps between different nodes of the repulsive lock laser standing wave, the coupling strength of the atom to the cavity changes.

initial insertion conditions, i.e. the coupling strength directly after insertion. We could not determine a systematic dependency on either of these parameters. Further examinations are required to clarify this phenomenon.

For the experimental records, exhibiting the coupling dynamics, we also observe the tendency to overall coupling reduction. In order to examine this behavior, we perform the same experiment as in Figure 2.6, but we hold an atom inside the cavity for a considerably longer timescale.

A single experimental record is presented in Figure 2.7 (a), where the transmission signal is monitored for 10 seconds. Note, that a break is introduced in the time scale of the figure, such that it displays the first and the last two 2 seconds of the transmission signal. Figure 2.7 (b) shows the average over 4 experimental records, where the transmission signal was subsequently binned over 4 ms, which is still shorter than the timescale of the dynamics of the transmission signal. Within the first 40 ms the transmission signal drops to 18% of the empty cavity transmission. Subsequently, for the next 1.5 seconds, the transmission signal exhibits abrupt variations, indicating the corresponding modifications of the effective coupling strength possibly caused by jumps of the atom along the cavity axis. Finally, the transmission signal stabilizes at a steady value of around 55% of the empty cavity transmission and stays constant for the remaining 8.5 seconds. The observation timescale exceeds by far the lifetime of the atom inside the cavity when the probe laser is switched off, see Figure 1.16, indicating a cooling action of the probe laser.

A possible explanation for the observed reduction of g is anticipated in [68]. There, it is shown theoretically that for the simplified two-level atom strongly interacting with cavity field and for the parameter regime used in our experiment, i.e. $\Delta_c > 0$ and $\omega_p = \omega_c$, the atom experiences optimal cooling by the probe laser at the lower coupling strengths.

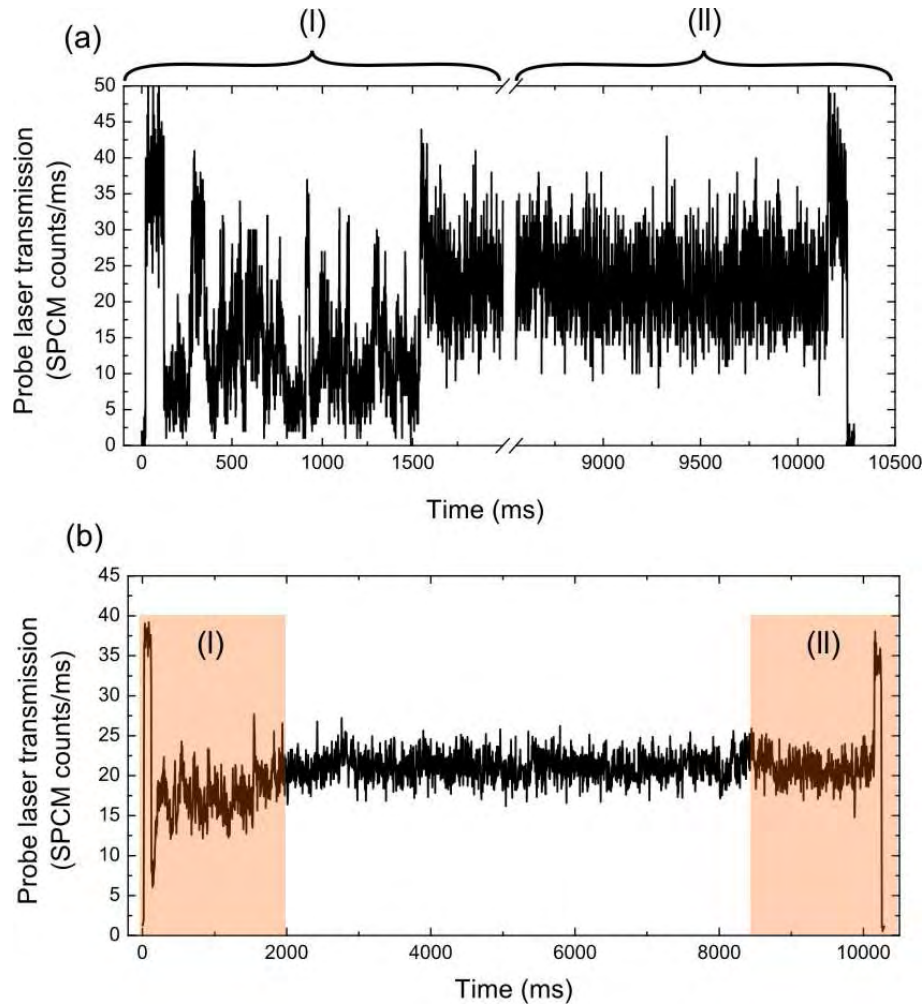


Figure 2.7: (a) Transmission signal of the probe laser while a single atom resides inside the cavity during 10 seconds. The signal shows the evolution from the time-dependent coupling strength (the first 1.5 sec) to its equilibrium level (the subsequent 8.5 sec). (b) The average over four such traces.

Figure 2.8 shows the sketch of the anticipated Sisyphus-type mechanism of the cavity cooling. Due to spatial modulation of the coupling strength along the cavity axis, the energies of the dressed states are modulated correspondingly. The coupled atom-cavity system is likely to absorb a photon at zero coupling strength. Emission of an energetically higher photon reduces the kinetic energy of the atom and therefore provides cooling. Although this model considers one-dimensional space, and does not take into account the effect of the AC stark shift induced by the lock laser and by the dipole trap, it provides qualitative explanation of our observations.

Since the temporal average of the coupling strength is determined by the atomic position and degree of its localization, the modification of the coupling strength is caused

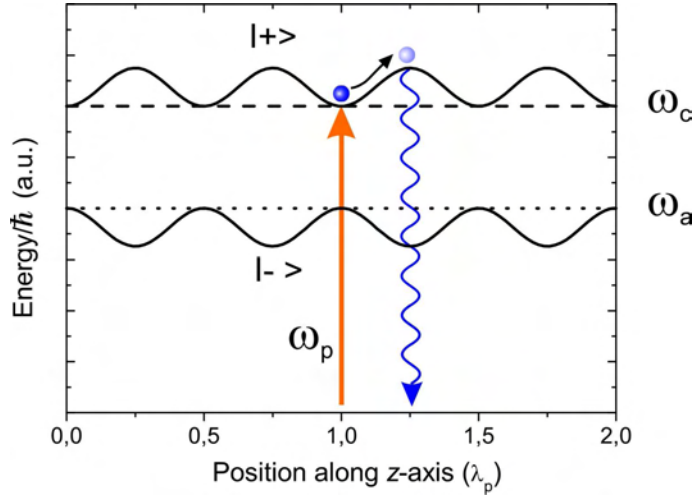


Figure 2.8: Sketch of the anticipated Sisyphus-type cavity cooling mechanism when $\omega_c > \omega_a$ and $\omega_p = \omega_c$. $|+\rangle$ and $|-\rangle$ are the dressed states of the coupled atom-cavity system. The photon is absorbed at the node of the probe laser standing wave, where $g = 0$, and energetically higher photon is emitted at a large coupling strength g , reducing the kinetic energy of the atom and thus enabling cooling.

by varying atomic position. As discussed above, the initial dynamics of the transmission signal is possibly caused by jumps of the atom along the z -axis. What remains in question is where the atom locates when the coupling reaches its equilibrium value. Here three possible scenarios are provided:

- (a) The atom jumps along the cavity axis (z -axis) until it gets confined in one of the potential minima of the lock laser, and at the same time, the corresponding coupling strength is small, where cooling is optimal.
- (b) Due to interplay of the cooling and heating processes, the atom is pushed in the radial direction of both cavity mode and the dipole trap (x -axis) such that the confinement by the lock laser is suspended, and the atom undergoes radial oscillations in the dipole trap along the z -axis over a distance corresponding to several lock laser potentials. During these oscillations the atom averages over the full range of coupling strengths, leading to an effective reduction of the coupling strength compared to the case when the atom is confined along the cavity axis by the lock laser potential. Since the period of radial oscillations is smaller than the integration time of the SPCM, the detected transmission signal is an average over the full range of transmission signals, and therefore, aside from shot noise, has a nearly constant level.
- (c) The atom jumps along the dipole trap axis (y -axis) over the distance comparable with the cavity mode radius w_0 and resides at a weaker coupling.

We exclude the scenario (c) by transporting the atom back to the position of the MOT after observing the transmission signals. At the MOT position we take a second picture, which confirms that the position in the standing wave dipole trap has not changed.

As has been reported in [56, 15], the observation of temporal variation of the cavity transmission can be used in order to track intra-cavity atomic trajectories. Although in the current state of our experiment the exact trajectories cannot be extracted, it might become feasible by gaining additional information about the atomic motion. For example, this could be achieved by recording the transmission signal with a much higher temporal resolution and analyzing the recorded data using autocorrelation functions. In this way it should become possible to extract the oscillation frequency of the atom and discriminate between above mentioned scenarios (a) and (b). Moreover, by coupling more than one atom to the cavity mode, it might become possible to observe and examine the collective effects, predicted in [70].

2.3.4 Controlling the coupling strength

Applications of cavity QED in quantum information experiments with a string of atoms usually require control over the coupling strengths for different atoms. This can be achieved e.g. by suitably positioning them inside the cavity mode profile. Here an experiment is presented, where we map out the spatial distribution of the coupling strength transverse to the cavity axis by continuously observing the cavity transmission while transporting a single atom slowly through the mode. Similar observations are reported in [60, 63].

In the experimental procedure, we first shuttle the atom to the edge of the mode $50\ \mu\text{m}$ from the mode centre, where g is negligible. As it is depicted in Figure 2.9, by slowly transporting the atom over $100\ \mu\text{m}$ across the cavity mode within 150 ms, we observe a continuous variation of the transmission caused by a variation of g . After a waiting time the direction of the slow transport is reversed. For both transportation directions the average transmission drops to about 20 % of its maximum level in the centre of the cavity mode, and the shape of the transmission is almost identical.

The drop to about 20 % is less than the reduction in the previous single shot experiment. This is a result of averaging over 19 shots, selected only for the presence of the atom during the complete transportation in both directions, and of a larger blue detuning of $\Delta_c/2\pi \approx 44\ \text{MHz}$. Due to thermal oscillations along the z -axis inside the dipole trap, the atom enters the cavity field in different nodes of the lock laser standing wave, thus causing the coupling strength and the reduction of the transmission to have different values for each transport through the cavity mode.

I have compared our observations with the prediction of the simple model by performing a numerical simulation. With the temperature as a single fit parameter, the simulations are in good agreement with the measured data by assuming a temperature of about 0.13 mK.

2.3.5 Atom-number dependent coupling strength

When coupling N atoms simultaneously to the cavity mode the effective collective coupling strength g_N ideally scales as $g\sqrt{N}$ for the case of weak excitation, where g is the coupling strength of a single atom.

In Figure 2.10 we compare the cavity transmission when sweeping either one or two atoms slowly through the cavity mode. In the case of two atoms their separation is below

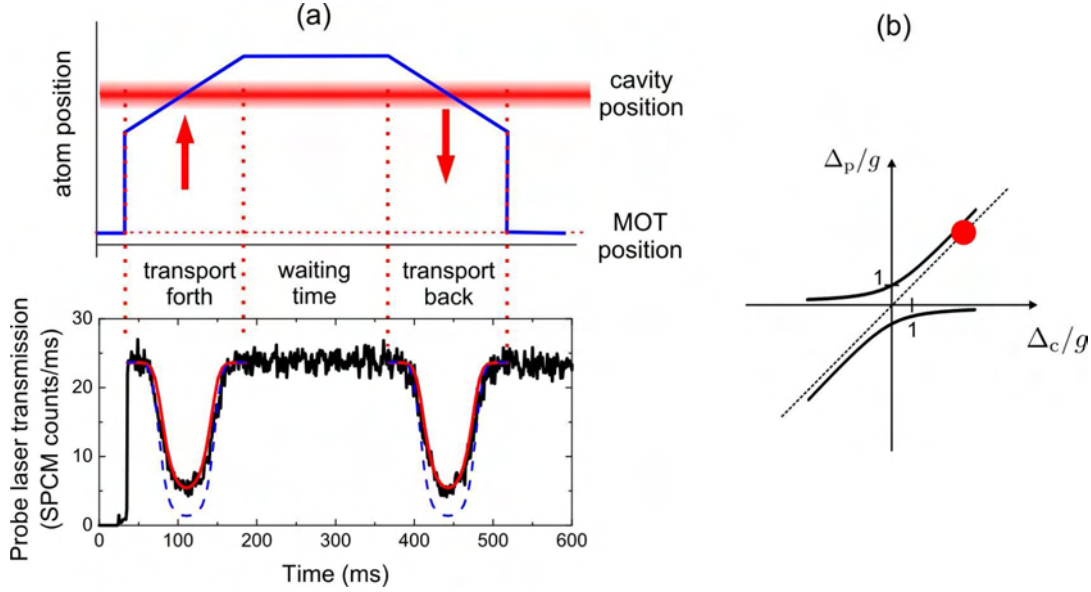


Figure 2.9: (a) Transmission of the probe laser beam as an atom is slowly swept forth and back across the cavity mode over a distance of $100 \mu\text{m}$ within 150ms . The trace is an average over 19 experimental runs. The measured data are in a good agreement with the numerical simulation (solid line in red). The probe laser is blue-detuned with respect to the $F = 4 \rightarrow F' = 5$ atomic transition by $\Delta_c/2\pi \approx 44 \text{MHz}$. The dashed blue line indicates the cavity transmission assuming no thermal motion and strongest coupling along the cavity axis. (b) Schematic illustration of the energies of the coupled atom-cavity states (solid lines), our detunings Δ_c and Δ_p are shown as a red circle.

$1.5 \mu\text{m}$, which is small compared to the waist of the cavity mode. We therefore assume that the two atoms are interacting with the cavity mode simultaneously at the same position. The data in Figure 2.10 are single experimental runs and are selected for strongest coupling along the z -axis, as discussed in the previous section. In the central region of the cavity already a single atom almost completely blocks the transmission of the probe laser. However, at the outer regions of the cavity mode two atoms cause a significantly stronger drop in transmission than a single atom.

In analogy to the previous paragraph, I have performed a numerical simulation, assuming that the intra-cavity temperature of the atoms is the same as in the experiment presented in Figure 2.4¹. The case of two atoms is approximated here by a single atom coupled to the cavity with a strength $g \times \sqrt{2}$. The numerical simulation agrees well with the measured data for the central region of the cavity. In the outer regions, both measured transmission levels are slightly higher than the calculated ones. This deviation is to be expected, as the model assumes constant confinement of the atom by the blue-detuned lock-laser standing wave independent of the position along the dipole trap axis. However, this confining potential decreases towards the edge of the cavity mode, and at some point the atom is no longer confined by the lock laser standing wave. As a result, the atom

¹In this experiment the detuning Δ_c is the same as in the observation presented in Figure 2.4.

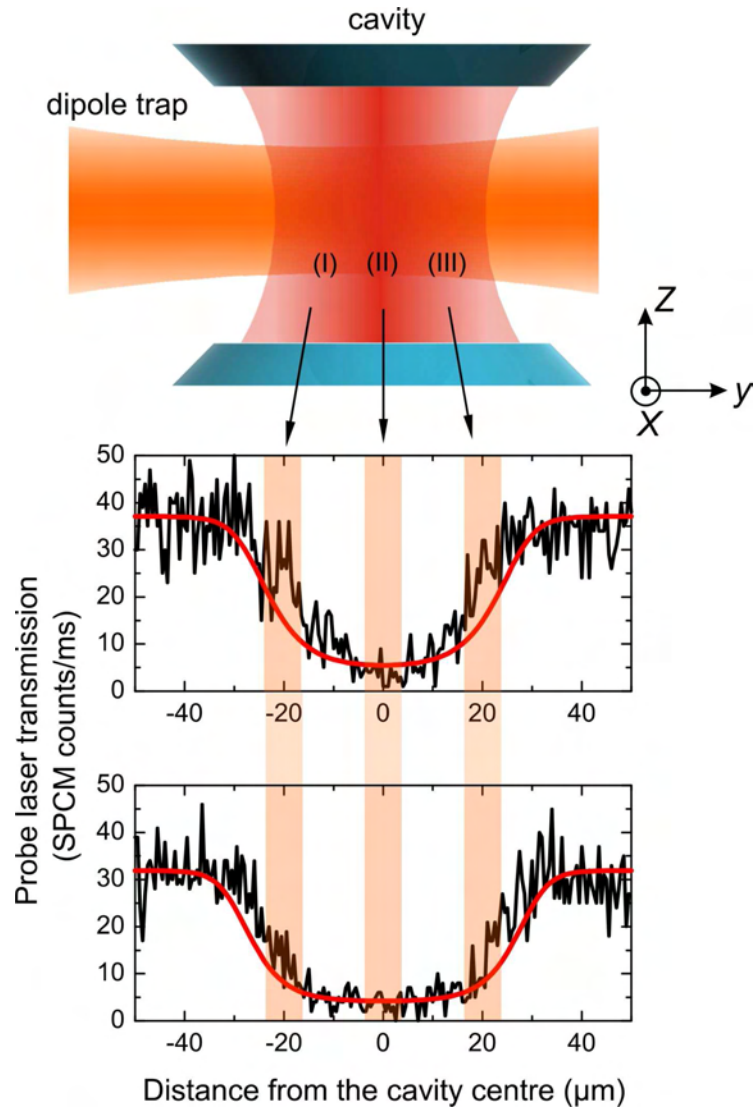


Figure 2.10: Transmission of the probe laser beam as a single atom (on the top) and two atoms (below) are swept across the cavity mode. For the latter case the width of the transmission dip is notably larger, indicating a stronger coupling strength. The probe laser is blue-detuned with respect to the $F = 4 \rightarrow F' = 5$ atomic transition by $\Delta_c/2\pi \approx 24$ MHz. The measured data agrees reasonably well with the numerical simulation (solid red lines) for one and two atoms in the upper and lower graph, respectively.

oscillates freely along the z -axis and experiences on average a weaker coupling strength, thus increasing the transmission level.

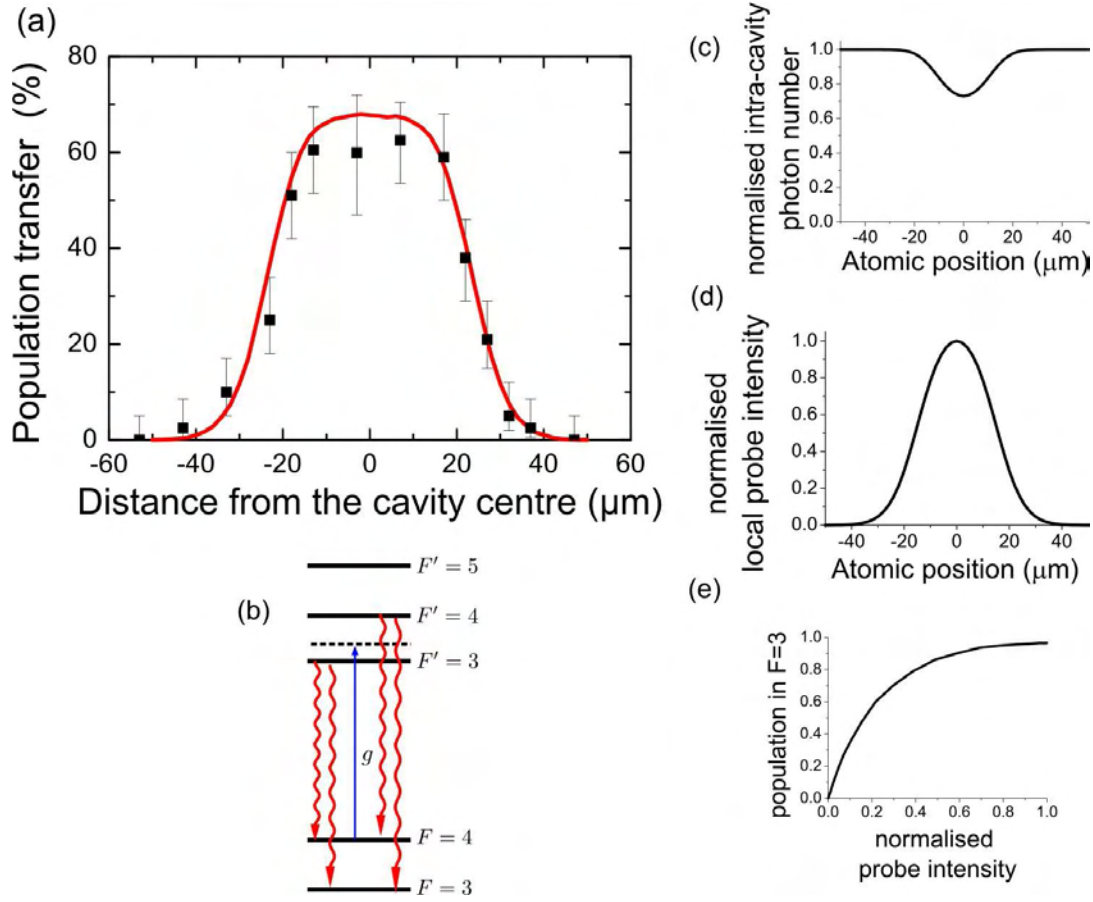


Figure 2.11: (a) Measurement of the final state of the atom after it has interacted with the field of the cavity mode. Each point is the result of about 40 experimental runs with a single atom. Model for an atom in the state $|F = 4, m_F = 1\rangle$: (c) intra-cavity photon number and (d) local probe laser intensity as a function of the atomic position and (e) pumping efficiency as a function of local probe laser intensity.

The solid red line in (a) is then obtained by taking the composition of (d) and (e), performing these calculations for each state $|F = 4, m_F\rangle$, and averaging subsequently. (b) The probe laser is blue detuned from the $F = 4 \rightarrow F' = 3$ transition by 40 MHz and is red detuned from the $F = 4 \rightarrow F' = 4$ transition by 160 MHz.

2.4 Detection of atom-cavity coupling via the atomic state

In this section I will present a different method to extract information about the coupled atom-cavity coupling. It is based on the detection of the internal atomic state after an atom has interacted with the field of the resonator. In the microwave domain this method is already used in cavity QED experiments, which are performed in the group of S. Haroche [71].

In this experiment we map out the spatial distribution of the cavity field via the detection of the atomic state. For this measurement, we prepare a single atom in the dipole trap

in the hyperfine ground state $F = 4$ by illuminating it with the MOT repumping laser. We then transport the atom to the cavity mode and subsequently inject the probe laser beam into the cavity. In this experiment the cavity is blue detuned by about 40 MHz from the $F = 4 \rightarrow F' = 3$ transition and is red detuned by 160 MHz from the $F = 4 \rightarrow F' = 4$ transition. During the interaction time of 1 ms the injected probe laser power corresponds to about 0.04 photons inside the cavity, much less than what was used in the previous experiments presented above. The atom is pumped into the uncoupled $F = 3$ ground state with a probability proportional to the intra-cavity probe light intensity, after scattering a few photons only. We retrieve the atom from the cavity and subsequently detect its final state with an efficiency close to unity by applying a “push-out” laser [72]. This laser is resonant with the $F = 4 \rightarrow F' = 5$ transition and removes the atom from the trap if it is in $F = 4$. Subsequent transfer of the atom back to the MOT reveals its presence if it is in $F = 3$. In order to ensure the efficient operation of the push-out laser we reduce the depth of the dipole trap after transporting the atom back to the MOT position, which limits the overall survival probability of the atoms in $F = 3$ to 77^{+7}_{-9} %.

For each position of the atom inside the cavity mode we take an ensemble average of about 40 repetitions. By varying the atomic position across the cavity mode, we map out the optical pumping rate due to the probe laser beam inside the cavity, see Figure 2.11(a). We observe a peak in population transfer corresponding to the transverse cavity mode profile with a maximum transfer efficiency of about 60 %. In this experiment an atom interacts dispersively with the cavity field and has only a small effect on the intra-cavity photon number. Therefore this photon number still weakly depends on the distance of the atom from the cavity mode centre and on the initial m_F state of the atom. As an example, Figure 2.11(c) shows the calculated normalized photon number as a function of atomic distance from the cavity centre in the case of an atom occupying the state $|F = 4, m_F = 1\rangle$. The resulting probe laser intensity, shown in Figure 2.11(d), is slightly broader than the Gaussian intensity profile in the absence of an atom. Compared to Figure 2.11(d), the transfer efficiency curve is further broadened due to the nonlinear dependence of the transfer efficiency on the probe light intensity. I have modelled this dependence, shown in Figure 2.11(e), for each initial m_F state by performing Monte-Carlo simulations and taking thermal motion into account, as was described in section 2.3.2. The holding time of an atom inside the cavity was divided into 10 μs -intervals, short compared to the average scattering rate. In each of these intervals the atom is assumed to be either excited with a probability determined by the local probe laser intensity and the corresponding Clebsch-Gordan coefficient and then to decay to the hyperfine state $F = 4$ or $F = 3$ with the corresponding branching ratios; or it remains in the state $F = 4$. The result of this simulation for the initial state $|F = 4, m_F = 1\rangle$ is shown in Figure 2.11(e). It is used to compute the spatial variation of the population transfer from the probe intensity distribution of Figure 2.11(d). I again assume a homogeneous distribution over different m_F states and average the population transfer over these states. Since the simulation shows only a very slight dependence on temperature, the intra-cavity photon number is used as a single fit parameter. The resulting photon number of 0.02 equals 60 % of the expected photon number estimated from the transmission. This deviation are attributed to systematic uncertainties of our model and inaccuracies of our measurement.

The theoretical curve in Figure 2.11(a) is obtained by normalizing the simulated averaged population transfer to the survival probability of 77 % and fits well to the observed data.

2.5 Conclusion

In this chapter two different methods to detect the atom-field interaction have been presented. Both might have decisive applications in future experiments.

In the measurement method, based on the detection of a weak probe laser, the atom-field coupling strength is monitored continuously. We observe a position-dependence and atom-number dependence of the coupling strength by sweeping one and two atoms through the cavity field. By improving the localization of a single atom, it should become possible to gain a full control over the coupling strength. Moreover, this method could be used to detect the intra-cavity motional dynamics of a single atom. By extending this method to multiple atoms, it might become feasible to observe cavity-induced motional collective effects [70].

A different method to observe the atom-field interaction, based on the measurement of the final hyperfine atomic state, allows us to detect interaction with the cavity field, and at the same time avoid the heating of atoms during the interaction. Moreover, the measurement of the final atomic state is an essential ingredient of the detection of entangled and multi-atom correlated states. Together with our ability to selectively initialize and manipulate the internal state of individual atoms [17], we are approaching our ultimate goal – the entanglement of two atoms.

Chapter 3

Quantum jumps and normal mode splitting

3.1 Introduction

The ability to experiment with individual quantum-mechanical objects makes possible to observe a number of interesting effects, which are completely hidden while experimenting with a large ensemble of identical quantum-mechanical objects. In particular, the observation of *quantum jumps* – dynamic projection of a quantum-mechanical system on its eigenstates, is enabled. Quantum jumps have been demonstrated on a variety of systems: The fluorescence of single trapped ions or of single molecules ceases and reappears abruptly, caused by quantum jumps to and from a “dark” metastable state [73, 74, 75, 76]. A single electron has been shown to reveal quantum jumps between Fock states of oscillatory cyclotron motion [77]. Recently, the dynamics of the number of microwave photons trapped in a superconducting cavity has been measured, using the Ramsey phase shift of Rydberg atoms crossing the cavity field [71, 78].

Here, I will present the quantum nondemolition (QND) measurement of the internal state of an individual neutral atom strongly coupled to the cavity field. As will be discussed in Section 3, this QND measurement method facilitates the observation of quantum jumps between the hyperfine ground states of single atoms, visible in the telegraph signal of the cavity transmission. Analysis of the telegraph signal as well as quantum jump correlations using second order correlation function discloses the dynamical and statistical properties of quantum jumps, which will be discussed in Section 3.2.3.

In Section 3.3 the adoption of the QND detection method for measuring of the excitation spectrum of a strongly interacting atom-cavity system will be presented. The latter shows a signature which is known as vacuum Rabi splitting or normal-mode splitting [14]. Although the observation of normal-mode splitting for the case of single-atom-cavity system has been reported from several groups [79, 51], so far it has been measured via the state of the output light field. Here, I will present the first observation of the normal-mode splitting detected via the atomic state.

3.2 Quantum jumps

3.2.1 Intra-cavity quantum nondemolition (QND) detection of the atomic state

Our atom-cavity system provides a unique opportunity to detect the hyperfine state of a single atom without losing the atom, and ideally without changing its hyperfine state. In principle, this method formally fulfills the requirement of a QND measurement [80, 81].

There exist two classes of QND measurements - projective measurements and weak measurements. Generally, a projective QND measurement of an observable A of a quantum-mechanical system fulfills the following criterion [80, 82, 83]: The result of each measurement of A yields a result identical to the first measurement, i.e. $[\hat{A}(t_i), \hat{A}(t_j)] = 0$ for different times t_i and t_j . Moreover, if t_i and t_j are chosen arbitrarily, then the measurement is called a continuous projective QND measurement. In contrast, a so-called discrete QND measurement can only be performed at strictly defined moments of time [80].

The requirement that the observable \hat{A} must be preserved during the measurement and the evolution between successive measurements imposes the following conditions:

1. The observable A must be a constant of motion, meaning that its operator should commute with the Hamiltonian of a freely evolving system.
2. The probing meter measuring A must not depend on the conjugate operator of \hat{A} , i.e. \hat{A} should commute with the interaction Hamiltonian.

Due to the Heisenberg uncertainty principle, which sets a lower bound on the product of uncertainties of conjugate observables, a projective QND measurement completely erases the information about the observable conjugate to A . For example, measuring the momentum of free particle makes its position completely unpredictable after the measurement.

In contrast, a weak QND measurement probes an observable A such that only partial information about its state is obtained, each time imposing the minimal perturbation on the conjugate variable allowed by the Heisenberg uncertainty principle. Consecutive repetition of a weak QND measurement will eventually project the measurement observable onto one of its eigenstates. Thus, repetitive application of a weak QND measurement is equivalent to exertion of a single projective measurement. A weak QND measurement was applied on atomic ensembles to nondestructively record Rabi oscillations between atomic hyperfine states [84, 85]. In a different experiment the coherent state of the intra-cavity microwave field was gradually collapsed to a well-defined photon number state by measuring the phase of velocity-selected beam of Rydberg atoms traversing the cavity field [78].

Here I report on a continuous projective QND measurement of the spin state of a single atom. It is directly inferred from the cavity transmission signal. As discussed in Section 2.3.1, an atom in the $F = 4$ state strongly couples to the cavity field tuned close to the $F = 4 \rightarrow F' = 5$ transition, and therefore inhibits the transmission of the resonant probe laser due to the induced normal mode splitting. In contrast, an atom in the $F = 3$ state is detuned by 9 GHz from the cavity resonance, which is much larger than the atom-cavity coupling strength g . Therefore it does not couple to the cavity, leaving

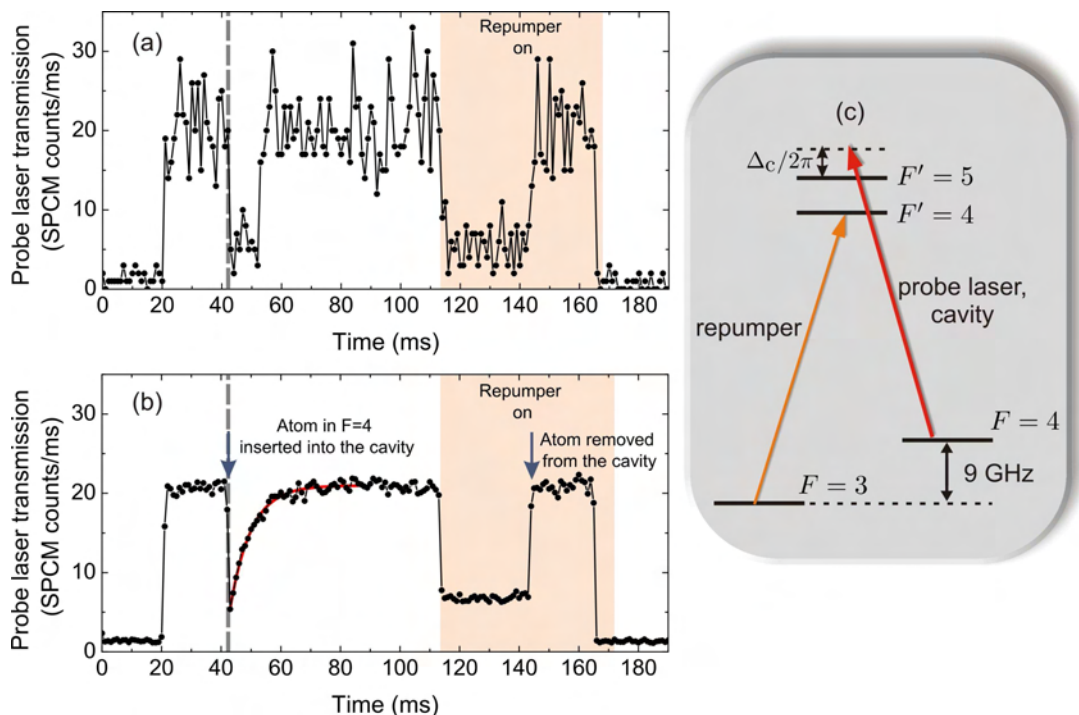


Figure 3.1: Detection of the atomic spin state using the cavity transmission. (a) Cavity transmission as an atom in the $F = 4$ state at time $t = 43$ ms is inserted into the centre of the cavity mode, while the cavity mode is filled with probe laser light only. In order to verify the presence of the atom after the state detection the repumping laser is switched on after $t = 113$ ms. (b) The cavity transmission averaged over 69 experimental runs. The transmission is fitted with an exponential decay (solid red line) with an average dwell time in the $F = 4$ state of $\tau_{\text{tr}} = (7 \pm 0.3)$ ms. (c) Schematics of the relevant energy states. The cavity resonance is blue detuned from the $F = 4 \rightarrow F' = 5$ transition by $\Delta_c/2\pi \approx 44$ MHz.

it's transmission unaffected. Thus, the intensity of the transmitted probe laser gives a direct indication of the atomic state. This method has also been reported in the group of H. Kimble for single measurements but has not been applied continuously [86].

Figure 3.1(a) shows a single experimental trace of the probe laser transmission as a function of time while a single atom in the $F = 4$ state is coupled into the cavity field. The cavity-atom detuning is $\omega_c - \omega_a \approx 44$ MHz and the probe-cavity detuning is $\omega_p - \omega_c = 0$. As expected, the insertion of the atom at $t = 43$ ms results in an abrupt drop of the transmission, in this case to about 21% of its initial level. After 9 ms the transmission signal jumps to the initial transmission level, caused by the pumping of the atom into the “dark” $F = 3$ state, which is a quantum jumps from $F = 4$ to $F = 3$ (see next section). This transfer happens in the following way: The probe laser, tuned close to the $F = 4 \rightarrow F' = 5$ transition, can off-resonantly excite an atom into the $F' = 4$ state. This happens after on average 10^2 scattering events. From the $F' = 4$ state the atom decays with comparable probabilities to both of the ground states, and therefore will be eventually

transferred to the dark $F = 3$ state.

As the high transmission of the probe laser can also indicate the absence of the atom, we need to distinguish loss of the atom from transfer to the $F = 3$ state. This is done by switching on the repumping laser at about 113 ms. If the atom is still inside the cavity, the repumping laser transfers the atom back in the $F = 4$ state, and the transmission signal reveals the presence of the atom inside the cavity. Finally, at $t = 143$ ms the atom is transported out of the cavity and the transmission rises to the level of the empty cavity.

Figure 3.1(b) shows the result of averaging over 69 such experimental traces, selected for survival of atom. The exponential form of the transmission signal is explained by simple statistical argumentation: According to Poisson distribution, the probability for an atom to remain in the $F = 4$ state is equal to $P_{F=4} = \exp(-t/\tau_{\text{tr}})$, where τ_{tr} is the average transfer time from the $F = 4$ state to the $F = 3$ state. Consequently, the probability for an atom to be transferred to the $F = 3$ state is equal to $P_{F=3} = 1 - \exp(-t/\tau_{\text{tr}})$, which determines the form of the averaged transmission signal.

The exponential fit yields a transfer time of $\tau_{\text{tr}} = (7 \pm 0.3)$ ms, which is determined by the intra-cavity probe field intensity. Hence, the measured state is changed by the measurement process. This sets a limitation on the detection efficiency: At a given transmission count rate, the level of erroneous detection is determined by the ratio between the decay time and time which is used to determine the atomic state. For instance, at the current value of τ_{tr} detecting the atomic state for 1 ms would change its hyperfine state in about 13% of the cases. The erroneous detection could be suppressed by improving the photon detection efficiency, which for current experiments is equal to about 1.3%, see Section 1.3.3. This will allow us to use a lower probe laser power at the same transmission level, resulting in an increase of the transfer time τ_{tr} .

The presented method to detect the atomic state formally fulfills the requirement of a projective QND measurement. Using our method we can detect the atomic spin state almost without changing it. The imperfection of our atomic state measurement method is that it induces transitions from the $F = 4$ state to the $F = 3$ state at the rate, which is however significantly smaller than the inverse of our current detection time. It seems feasible to suppress photon scattering by improving the photon detection efficiency and operating in an even deeper dispersive regime, i. e. by tuning the cavity further away from the atomic transition.

3.2.2 A random telegraph signal of quantum jumps

The QND measurement method, presented above, enables the observation of quantum jumps between two spin states of an atom: Since the cavity transmission yields the state of the atom, its changes can be monitored continuously by observing the transmission signal.

Figure 3.2 shows a random telegraph signal revealing the dynamics of the spin state of a single atom kept inside the cavity for about 400 ms. The atom-cavity detuning and the probe-atom detuning are the same as for the measurement in Section 3.2.1. As discussed above in the previous section, the probe laser light induces transitions from the $F = 4$ state to the $F = 3$ state. In order to depopulate the $F = 3$ state, a weak repumping laser

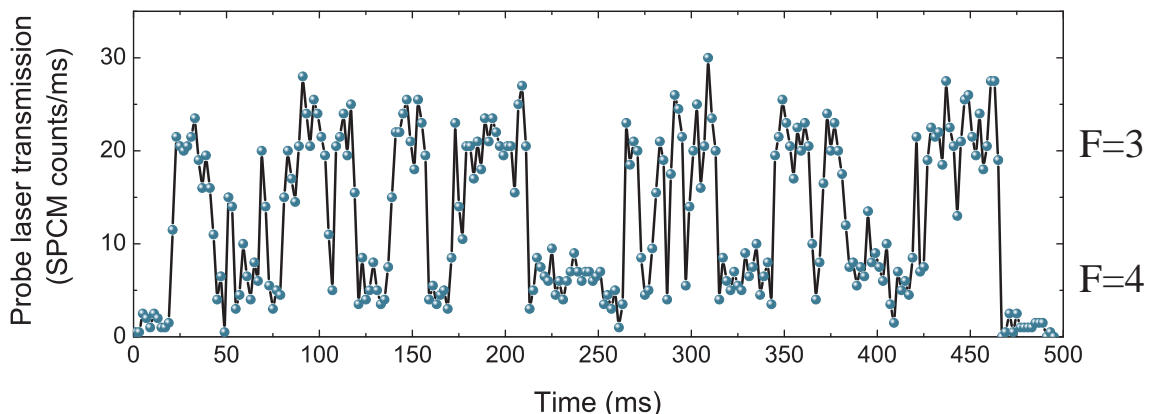


Figure 3.2: Quantum jumps of a single atom between the ground states $F = 3$ and $F = 4$, revealed in a telegraph-like cavity transmission signal. A weak repumping laser is applied along the dipole trap, bringing the atom at a low rate back to the $F = 4$ state.

is shined in along the dipole trap axis, tuned close to the $F = 3 \rightarrow F' = 4$ transition, and transfers the atom to the $F = 4$ state. The intensity of this laser is adjusted carefully to ensure that the rate of $F = 4 \rightarrow F = 3$ transitions is comparable to jumps from $F = 3$ to $F = 4$. The time resolution of the telegraph signal is determined by the photon counter binning time of $t_{\text{bin}} = 2$ ms.

3.2.3 Characterization of quantum jumps

In order to identify quantum jumps, partially masked by the statistical and technical noise, I have analyzed the acquired data with an algorithm, allowing to extract the temporal evolution of atomic spin states from the random telegraph signal.

Statistics of atomic state detection

Figure 3.3 shows the histogram of the transmission levels extracted from 163 experimental traces. It displays two peaks, corresponding to the cavity transmission for the atom in the $F = 4$ and $F = 3$ states. For each peak a fit with a Gaussian function is shown. The dotted line is the sum of both Gaussians. As a comparison the dashed line stands for the calculated distribution, taking into account only the Poisson shot noise of the transmission signal and adjusted to the height of the corresponding peaks of the histogram. The measured distributions are noticeably broader than the Poisson distributions. This is essentially caused by the variation of the atom-cavity coupling strength for the left peak and by the imperfections of the cavity frequency stabilization servo loop for the right peak. On the one hand, variation of g results in variation of the corresponding transmission levels. On the other hand, cavity frequency variations result in the mismatch between its frequency and the probe laser frequency, causing the broadening of the empty cavity transmission signal. Notably, the peaks corresponding to the states $F = 4$ and $F = 3$ partially overlap, so that the state of the atom cannot be inferred directly from the telegraph signals without

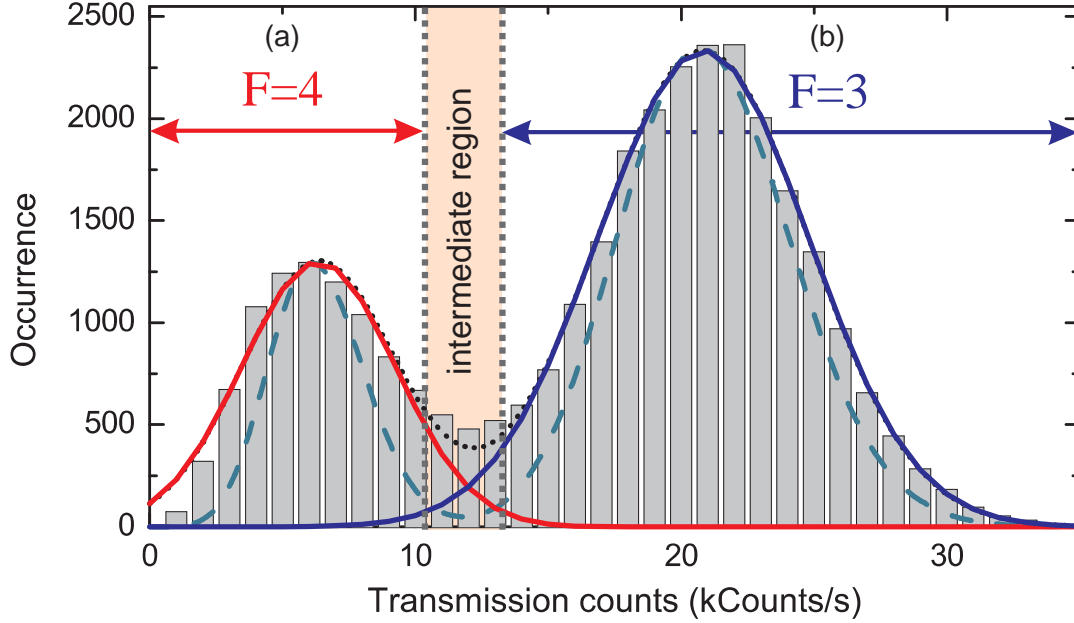


Figure 3.3: Histogram of transmission counts within 2 ms bins, evaluated from 163 quantum jumps records, each circa 400 ms long. Peaks of the histogram, fitted with Gaussian distributions, correspond to the $F = 4$ (red line) and $F = 3$ (blue line) states. The black dotted line shows the sum of these Gaussians. The dashed line indicates the ideal case of pure statistically limited Poisson distribution. The transmission counts in the region (a) and (b) correspond to the state $F = 4$ and $F = 3$, respectively.

additional analysis.

Digitization of quantum jumps

From the distribution of the transmission histogram in Figure 3.3, the intervals are defined which are used to assign the atomic spin state to each transmission level of the telegraph signal.

The region of transmission values corresponding to the $F = 4$ state, see Figure 3.3 (a), is defined such that only 1% of the values for an atom in $F = 3$ lies in this region. Vice versa, the region (b) Figure 3.3 is chosen to contain only 1% of the transmission values related to the $F = 4$ state and is therefore used to indicate $F = 3$. In the overlap region, which contains about 4% of all time bins, the transmission level cannot be assigned to any of the states. In this case the algorithm compares previous and subsequent transmission values (see Figure 3.4). If they correspond to the same state (Figure 3.4 (a)), then the current value is interpreted as noise, since the probability of two consecutive quantum jumps is considerably smaller than the probability for the transmission signal to be in the intermediate range¹. If the previous and subsequent value correspond to different

¹The probability of two consecutive quantum jumps is equal to $t_{\text{bin}}^2 / (2\tau_{F=4}\tau_{F=3}) = 0.9\%$, where $\tau_{F=4}$ ($\tau_{F=3}$) is the dwell time in the $F = 4$ ($F = 3$) state, defined in Equation 3.2 (Equation 3.3)

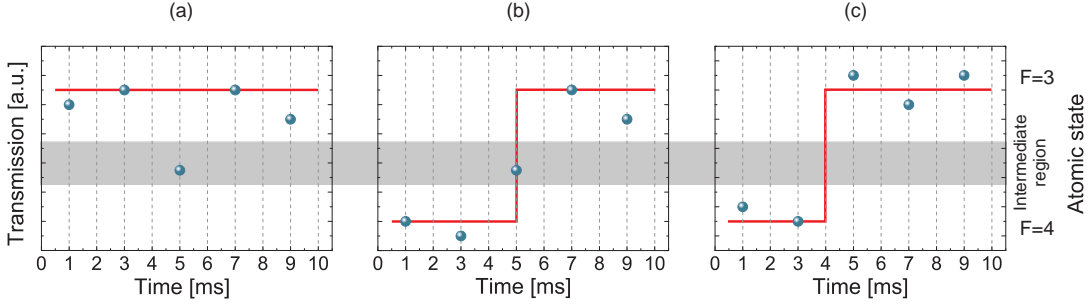


Figure 3.4: Schematic illustration of the algorithm. (a) If previous and subsequent values (green dots) of the transmission correspond to the same atomic state then the middle value, lying in the intermediate region, is interpreted as noise. (b) In the case when the previous and the subsequent value are different, the middle value is interpreted as a quantum jump. Note, that the resolution of the digitized signal is 1 ms comparing to 2 ms binning time of the recorded traces. Therefore, as it is displayed in (c), when consecutive transmission levels correspond to different spin states (at $t = 3$ ms the state is $F = 4$, and at $t = 5$ ms the state is $F = 3$) the quantum jump is interpreted to happen in between, i. e. at $t = 4$ ms.

states (Figure 3.4 (c)) then the middle value is interpreted as a quantum jump. Note, that the digitized signal has the 1 ms time resolution, whereas the telegraph signals are recorded with 2 ms bin size. It allows to discriminate between the situations displayed in Figure 3.4 (b) and Figure 3.4 (c), where in the latter case two consecutive transmission values correspond to different spin states. This algorithm enables the reconstruction of the evolution of the atomic state from the recorded transmission signal reasonably well.

Figure 3.5 illustrates typical examples of the algorithm operation. The connected dots are the experimental traces and the red solid line is the output of the algorithm with two discrete states: low ($F = 4$) and high ($F = 3$).

Second-order correlations of the random telegraph signals

A powerful tool to characterize the dynamics of quantum jumps is the second-order correlation function $g^{(2)}$. It is defined as [87]

$$g^{(2)}(\tau) = \frac{\langle I(t) I(t + \tau) \rangle}{\langle I(t) \rangle^2}, \quad (3.1)$$

where $I(t)$ in our case is the intensity of the cavity transmission signal. Here angle brackets stand for temporal averaging. The $g^{(2)}(\tau)$ function evaluates the degree of correlation in the telegraph signal for different times τ and allows to directly extract the average dwell times in either of the spin states. Figure 3.6 shows the second order correlation, evaluated from 163 digitized telegraph signals. The solid line is an exponential fit with a decay time of $\tau_{\text{cor}} = (6.7 \pm 0.1)$ ms.

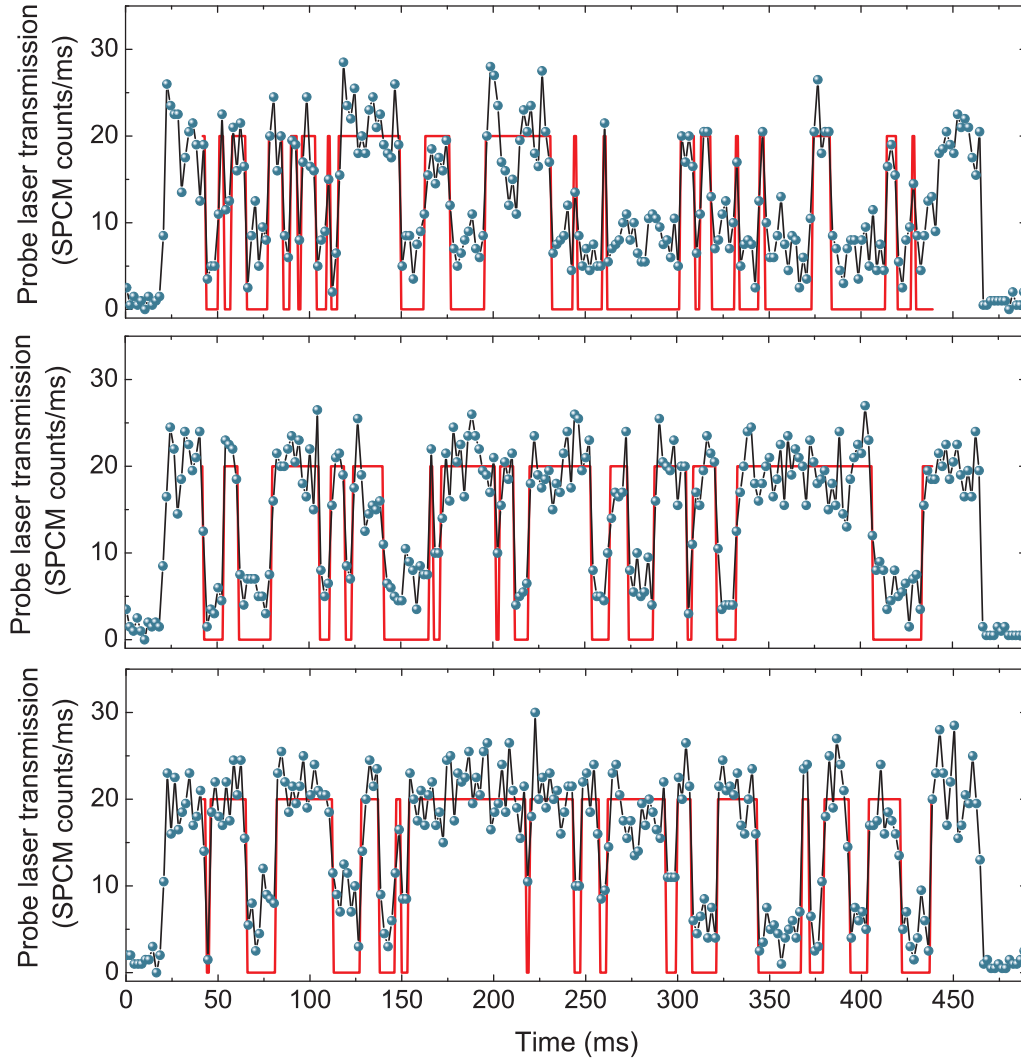


Figure 3.5: Typical examples of quantum jumps records and their digitization (red line).

Dwell times

Using the second-order correlation function the average dwell times, i. e. the average durations an atom spends in the corresponding spin state can be extracted from the digitized telegraph signals [88]. In principle, the dwell times can be directly extracted from the recorded telegraph signal. However, the variation of the transmission levels due to statistical and technical noise, and varying coupling strength, can distort the correlation function and hence falsify the resulting dwell times².

For the digitized telegraph signal, jumping between zero and one, the expression for

²Statistical noise leads to overestimation of $g^{(2)}(0)$, whereas technical noise may lead to appearance of the local maxima in the shape of $g^{(2)}(\tau)$ which are not reflecting the dynamics of the atomic internal state.

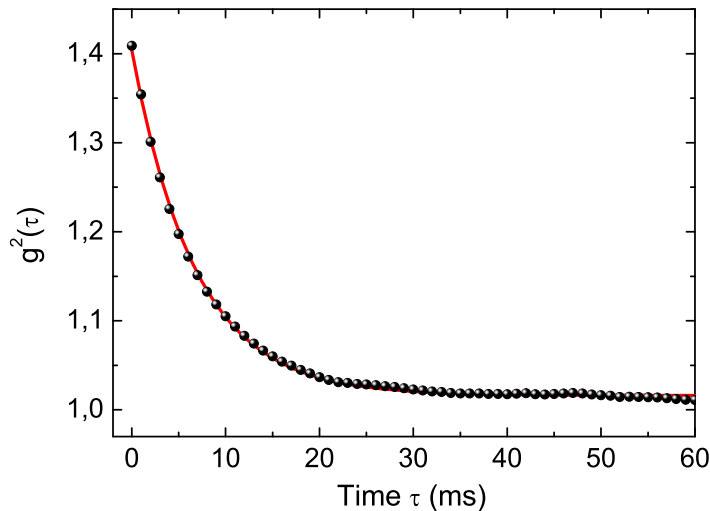


Figure 3.6: Second-order correlation function evaluated from 163 digitized traces of quantum jumps. The solid line in red is an exponential fit with a time constant of $\tau_{\text{cor}} = (6.7 \pm 0.1)$ ms.

the average dwell times in the $F = 4$ state $\tau_{F=4}$ and in the $F = 3$ state $\tau_{F=3}$ is given by

$$\tau_{F=4} = g^{(2)}(0) \tau_{\text{cor}} = (9.4 \pm 0.1) \text{ ms}, \quad (3.2)$$

$$\tau_{F=3} = \frac{g^{(2)}(0)}{g^{(2)}(0) - 1} \tau_{\text{cor}} = (23.5 \pm 0.4) \text{ ms}. \quad (3.3)$$

The average dwell time in the $F = 4$ state $\tau_{F=4}$, extracted from the correlation function through Equation 3.2, is notably larger than the τ_{tr} obtained from the exponential in Figure 3.1. A qualitative explanation is provided by the following consideration: For data in Figure 3.1 the observation of the atomic spin was limited to a single quantum jump which took place on a timescale of several ms, immediately after inserting an atom into the cavity mode. In contrast, for the telegraph signal the total observation time was as long as 400 ms. During this macroscopic time interval the atom is subjected to competitive cooling and heating mechanisms, which, as argued in [68] can cause the atom to reside in a region of a weaker coupling and, in addition, modify its temperature. Due to this fact both intra-cavity photon number and the local probe laser intensity change at the position of the atom, which in turn alters the scattering rate by the atom.

As comparison, the average dwell times in either of the states can be directly extracted from the digitized telegraph signal. The histograms of dwell times are presented in Figure 3.7. The linear fit implies $\tau_{F=4}^* = (9.1 \pm 0.3)$ ms and $\tau_{F=3}^* = (20.6 \pm 0.8)$ ms. Both dwell times agree reasonably well with the values extracted from $g^{(2)}$ in Equation 3.2 and Equation 3.3.

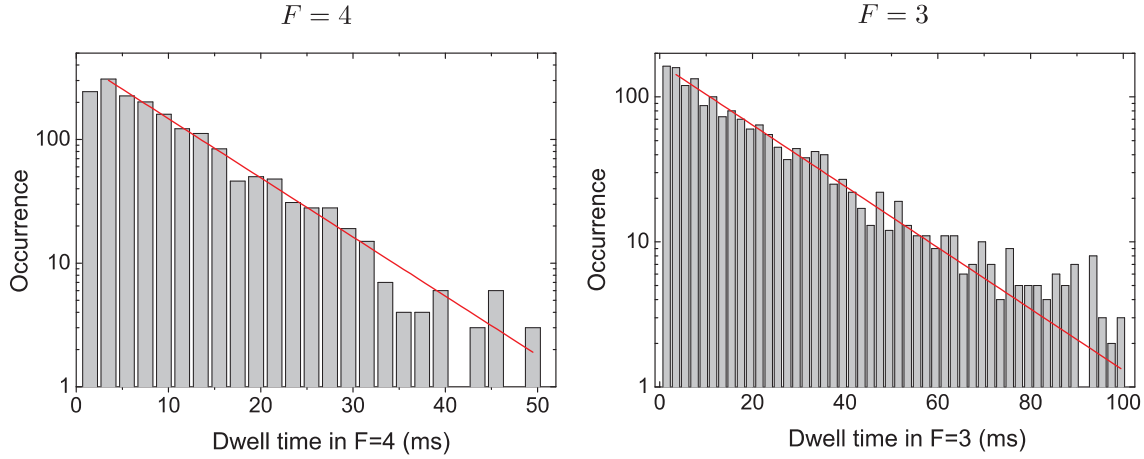


Figure 3.7: Histograms of the dwell times in the $F = 4$ and in the $F = 3$ states on logarithmic scale. The average dwell times $\tau_{F=4}^* = (9.1 \pm 0.3)$ ms and $\tau_{F=3}^* = (20.6 \pm 0.8)$ ms are extracted from a linear fit.

Antibunching of quantum jumps

A remarkable attribute of quantum jumps exhibited by a single atom is the antibunching in their occurrence. Immediately after a single atom experienced a quantum jump the probability to undergo the next such jump in the same direction vanishes, because the atom should be pumped back to its original state in the first place. In contrast, this phenomenon disappears when experimenting with an ensemble of atoms. Since each atom undergoes quantum jumps at uncorrelated and random moments of time, the ensemble-average atomic state would ideally exhibit a continuous variation.

In order to quantify this phenomenon, I have evaluated the second-order correlation function of quantum jumps from $F = 4$ to $F = 3$ (from $F = 3$ to $F = 4$) $g_{4 \rightarrow 3}^{(2)}$ ($g_{3 \rightarrow 4}^{(2)}$) from the digitized telegraph signals. It is analogous to the intensity correlation, defined in Equation 3.1, but here $I(t)$ is the intensity of the corresponding quantum jumps: For the quantum jumps from $F = 4$ to $F = 3$, $I(t) = I_{4 \rightarrow 3}(t)$ is equal to one whenever the atom undergoes a jump from $F = 4$ to $F = 3$, and zero otherwise. In analogy, the $I_{3 \rightarrow 4}(t)$ is defined.

The resulting correlation functions of $I_{4 \rightarrow 3}(t)$ and $I_{3 \rightarrow 4}(t)$ are presented in Figure 3.8. As expected, both $g_{4 \rightarrow 3}^{(2)}$ and $g_{3 \rightarrow 4}^{(2)}$ are approaching zero when τ goes to zero, providing a clear indication of antibunching. As τ increases the correlation function increases exponentially towards the value of one. It is interesting to note that the timescale of the exponential increase for both cases is defined by the same expression $\tau_{F=4}\tau_{F=3}/(\tau_{F=4} + \tau_{F=3})$, derived in [88]. The equality of both timescales can be understood by a simple symmetry argument: after an atom jumped from the $F = 4$ state to the $F = 3$ state it should be first transferred back to the $F = 4$ state before the next $F = 4 \rightarrow F = 3$ jump can take place, and vice versa for the $F = 3 \rightarrow F = 4$ jumps. Thus, the average duration between two consecutive jumps is the same for both jump directions.

The solid lines are the exponential fits of the form $1 - \exp(-\tau/t_{\text{anb}})$, where the

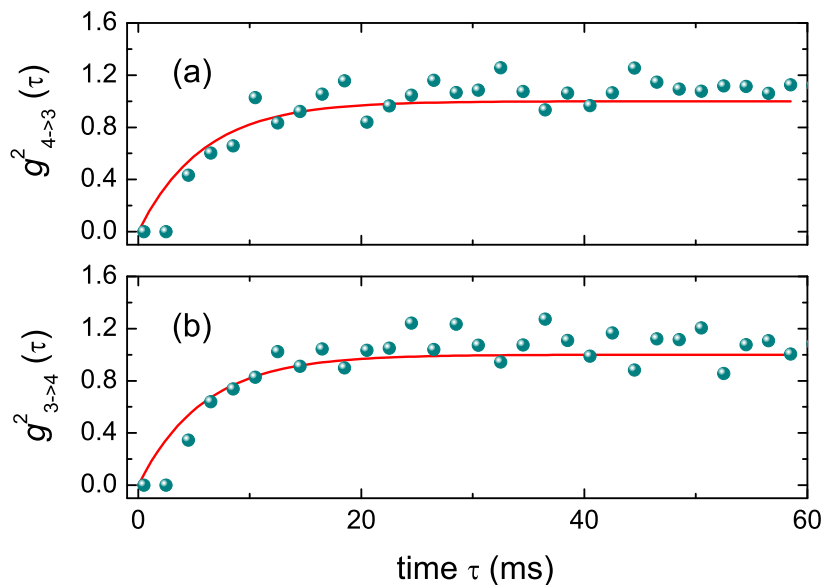


Figure 3.8: Second-order correlation $g^2(\tau)$ for quantum jumps for (a) the $F = 4$ to the $F = 3$ state, and vice versa from the $F = 4$ to the $F = 3$ state (b). The solid lines in red are the results of the exponential fit of the form $1 - \exp(-\tau/t_{\text{anb}})$. The exponential decay time is $t_{\text{anb}} = (6 \pm 1)$ ms in both cases.

outcome of the fit $t_{\text{anb}} = (6 \pm 1)$ ms is in good agreement with directly calculated $(\tau_{F=4}\tau_{F=3})/(\tau_{F=4} + \tau_{F=3}) = (6.7 \pm 0.1)$ ms, where $\tau_{F=3}$ and $\tau_{F=4}$ are the values calculated in Equation 3.2 and Equation 3.3.

3.2.4 Towards quantum jumps with more than one atom

The experiments described in this Chapter so far demonstrate the observation of quantum jumps of a single atom in the cavity. In the following, I would like to present an experiment where we simultaneously couple two atoms to the cavity field and observe conditional dynamics of their spin states.

The implementation of quantum gate operations using neutral atoms requires the availability of strong coherent coupling. Unlike the case of ions, where long-range Coulomb-like interaction is naturally available, neutral atoms interact only very weakly, and an additional effort has to be made in order to induce strong interaction in controlled manner. In cavity-QED experiments, the interaction is realized by coupling the atoms to the field of the resonator, which mediates the interaction between them. This can be described as an effective atom-atom coherent collision with the size of the collision cross-section enlarged to the size of the cavity mode.

In the case of two atoms simultaneously coupled to the resonator, each atom modifies the light field intensity in the resonator, which in turn affects the interaction of the other atom with the field. The dynamics of this conditional atom-cavity interaction can be

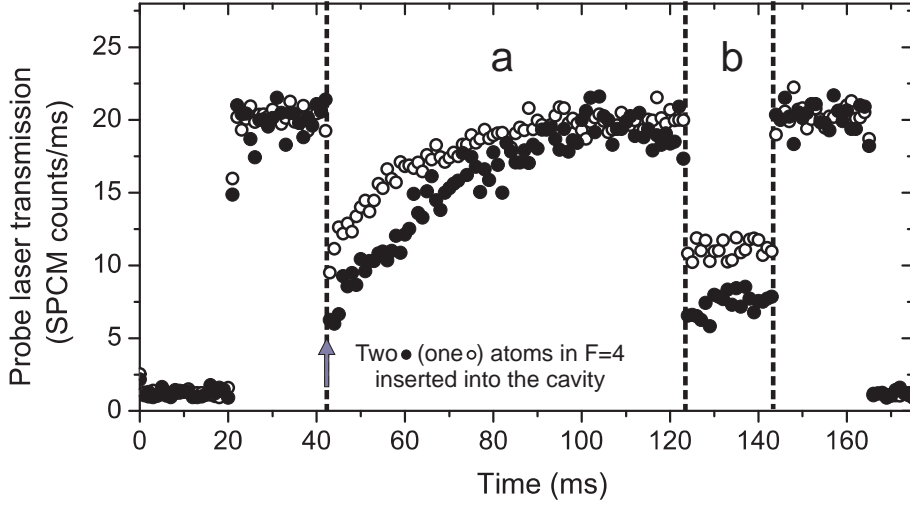


Figure 3.9: Averaged cavity transmission for one (\circ , averaged over 69 repetitions) and two atoms (\bullet , averaged over 23 repetitions) simultaneously coupled to the cavity. In the region (a) atoms are inserted while the repumping laser is switched off. By comparing the initial transmission levels the average dwell time $\tau_{2:F=4}$ for each atom in $F = 4$ in the case of two inserted atoms can be calculated. In order to check the atom survival in the region (b) the repumping laser is switched on.

visualized by observing the cavity transmission while coupling two atoms in the $F = 4$ state to the resonator: Since only atoms in the $F = 4$ state couple to the resonator, the probability of a quantum jump to occur from $F = 4$ to $F = 3$ depends on the number of atoms in $F = 4$. This process schematically visualized in Figure 3.10 (d), where two, one, and no atoms in the $F = 4$ state correspond to different cavity transmission levels, determining the atomic scattering rate from the intra-cavity probe light and the resulting probability of a quantum jump. Thus, the rate of quantum jumps becomes conditional on the state of both atoms.

In our experiment, we position two atoms in $F = 4$ at the edge of the cavity mode, about $15 \mu\text{m}$ away from the cavity axis. We select only those events where the distance between the atoms was below $8 \mu\text{m}$. At the edge of the mode the intra-cavity photon number depends significantly on the state of each atom. We monitor the probe laser transmission for about 80 ms while the repumping laser is switched off. The dots in Figure 3.9 show the result of an ensemble averaging over 23 of such traces. As a comparison, the open circles are obtained by averaging over 69 traces where a single atom in the $F = 4$ state was positioned at the edge of the resonator. The resulting average dwell time for a single atom is $\tau_{1:F=4} = (15 \pm 1)$ ms.

The dynamics of the transmission signal for the case of two atoms is well explained by a simple model without free parameter, which assumes that the rate of quantum jumps depends on the state of both atoms. When both atoms are in $F = 4$, the average dwell time for each atom $\tau_{2:F=4}$ is extracted by comparing the initial transmission levels for one and two coupled atoms (see Figure 3.9), which are inversely proportional to the dwell times.

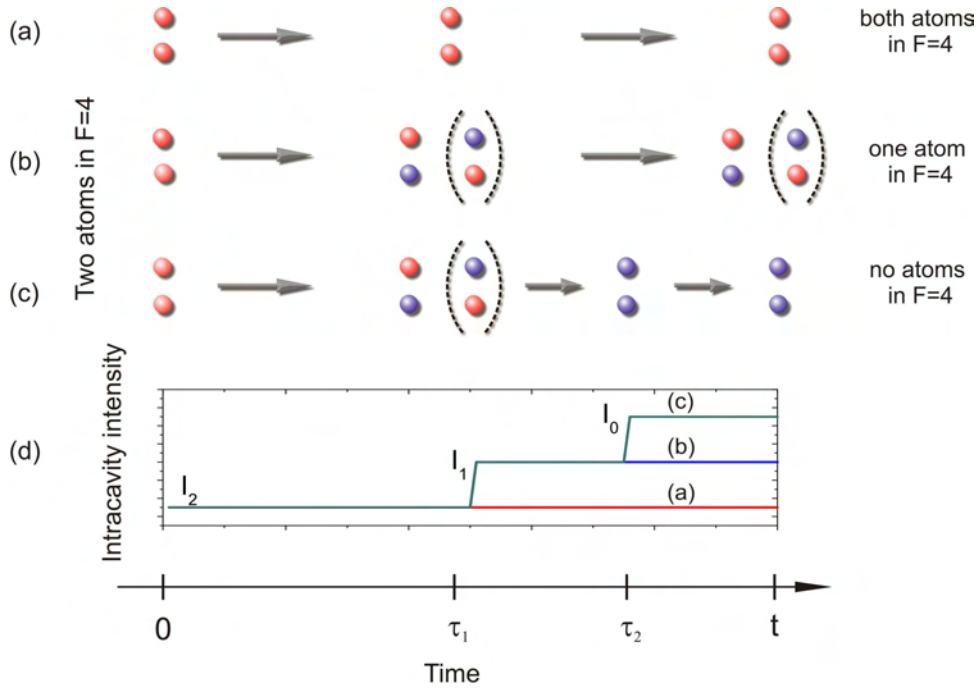


Figure 3.10: Simple model, describing the quantum jumps of two atoms with a three different scenarios: After duration t (a) both atoms remain in $F = 4$; (b) one atom is pumped into the state $F = 3$ or (c) both atoms are transferred in $F = 3$ state. As it is sketched in (d), the intracavity probe intensity depends on the number of atoms in the $F = 4$ state.

This yields $\tau_{2:F=4} = (24 \pm 1)$ ms.

Based on the knowledge of the average dwell times for both the one and the two-atom case, I have evaluated a simple stochastic process governing the temporal evolution of the transmission. In Figure 3.10 three possible scenarios of the spin evolution during an observation interval of duration t_{obs} are presented, where two atoms have initially been prepared in $F = 4$: (a) Both atoms remain in $F = 4$, (b) one of the atoms is transferred to $F = 3$, or (c) both atoms are flipped to the $F = 3$ spin state. The probabilities of these processes as a function of time are calculated in order to obtain the theoretical time evolution of the cavity transmission.

(a) This is the simplest case, having the following probability evolution

$$P_2(t) = \exp\left(-\frac{2t}{\tau_{2:F=4}}\right).$$

(b) This scenario can be calculated in the following way: Both atoms stay in the state $F = 4$ until time $t' < t$, which has the probability of $P_2(t')$. Then one of the atoms is transferred to the $F = 3$ state within the infinitesimal interval dt' with the probability $2dt'/\tau_{2:F=4}$. For the remaining duration of $t - t'$ the other atom stays in $F = 4$ and

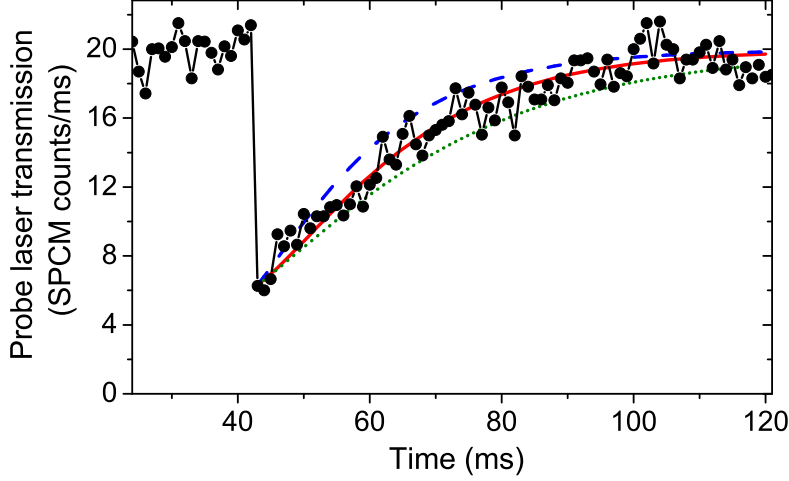


Figure 3.11: Averaged transmission of the probe laser as two atoms in the $F = 4$ state are coupled to the edge of the resonator mode (same data as in Figure 3.9). The solid line is the expected theoretical dependence for conditional dynamics of two atoms. For comparison, the dashed (dotted) line assumes an atom number independent average dwell time τ , yielding a transmission signal of the form given in Equation 3.6, where $\tau = \tau_{1:F=4}$ ($\tau = \tau_{2:F=4}$). They form an upper (lower) bound for the rate of quantum jumps.

the average dwell time in $F = 4$ is reduced to $\tau_{1:F=4}$. The corresponding probability is $\exp[-(t-t')/\tau_{1:F=4}]$. Thus, the probability that after duration t one atom has been transferred (at time t') to the $F = 3$ is

$$dP_1(t) = \exp\left(-\frac{2t'}{\tau_{2:F=4}}\right) \frac{2 dt'}{\tau_{2:F=4}} \exp\left(-\frac{t-t'}{\tau_{1:F=4}}\right). \quad (3.4)$$

And the expression for the probability of the process in Figure 3.10 (b) is obtained by integrating Expression 3.4 over all possible $0 < t' < t$

$$\begin{aligned} P_1(t) &= \frac{2}{\tau_{2:F=4}} \int_0^t \exp\left(-\frac{2t'}{\tau_{2:F=4}}\right) \exp\left(-\frac{t-t'}{\tau_{1:F=4}}\right) dt' \\ &= \frac{2\tau_{1:F=4}}{\tau_{2:F=4} - 2\tau_{1:F=4}} \left[\exp\left(-\frac{2t}{\tau_{2:F=4}}\right) - \exp\left(-\frac{t}{\tau_{1:F=4}}\right) \right] \end{aligned}$$

(c) In analogy to the case (b), the probability for both atoms being transferred to the $F = 3$ state after the duration t is given by

$$\begin{aligned} P_0(t) &= \frac{2}{\tau_{2:F=4}} \int_0^t \exp\left(-\frac{2t'}{\tau_{2:F=4}}\right) \left[1 - \exp\left(-\frac{t-t'}{\tau_{1:F=4}}\right) \right] dt' \\ &= 1 - \frac{\tau_{2:F=4}}{\tau_{2:F=4} - 2\tau_{1:F=4}} \exp\left(-\frac{2t}{\tau_{2:F=4}}\right) + \frac{2\tau_{1:F=4}}{\tau_{2:F=4} - 2\tau_{1:F=4}} \exp\left(-\frac{t}{\tau_{1:F=4}}\right). \end{aligned}$$

Taking this into account, the theoretical transmission dependence is equal to

$$I(t) = P_0(t)I_0 + P_1(t)I_1 + P_2(t)I_2, \quad (3.5)$$

where I_0 , I_1 , and I_2 are the respective transmissions corresponding to the empty cavity (both atoms in $F = 3$), one atom in $F = 4$ and two atoms in $F = 4$, which are extracted from Figure 3.9. This dependence is depicted as red solid line in Figure 3.11. The experimental data in this figure are for the two atom case, the same as in Figure 3.9. For comparison, the dotted and dashed lines assume an atom number independent average dwell time throughout the observation. In this case, by setting $\tau_{2:F=4} = \tau_{1:F=4} = \tau$ in the Equation 3.5, the transmission signal has the form

$$I(t) = I_0 \left[1 - \exp\left(-\frac{t}{\tau}\right) \right]^2 - 2I_1 \left[\exp\left(-\frac{2t}{\tau}\right) - \exp\left(-\frac{t}{\tau}\right) \right] + I_2 \exp\left(-\frac{2t}{\tau}\right). \quad (3.6)$$

The dashed line is calculated using $\tau = \tau_{1:F=4}$ and for the dotted line $\tau = \tau_{2:F=4}$ is used. In order to quantify the degree of consistency with experimental data, the χ^2 for all three cases is evaluated. The resulting value of χ^2 is a factor of 2 smaller for the case of atom-number dependent model than in the cases where the average dwell time is assumed to be atom-number independent. The transmission calculated from our model fits better to the measured data, providing the indication of conditional dynamics of the atomic spins.

3.3 Measuring the normal mode splitting via the atomic state

The most elementary example of interaction between matter and light is a single atom interacting with a single photon. A consequence of strong, coherent atom-light interaction is the occurrence of dressed states, appearing as a normal-mode splitting. It allows not only to gain a sophisticated understanding of atom-field coupling and to control spontaneous emission [89, 90, 91], but also forms the basis for many proposals, which could allow the basic steps of quantum information processing to be realized.

The technological advances in the recent decade has allowed the observation of normal-mode splitting in numerous systems, ranging from a quantum well coupled to a semiconductor microcavity [92] to transmission line resonators interacting with a superconducting qubit [93]. In systems involving the interaction of a single neutral atom with a high finesse optical resonator, the normal-mode splitting so far has been observed by monitoring the excitation spectrum of coupled atom-cavity system via photons leaking from the cavity [51, 79]. Here, I will present a measurement of the normal-mode splitting for the first time observed via the detection of atomic state.

3.3.1 Experimental sequence

The experimental procedure to measure the normal-mode splitting via the atomic state involves two major parts: First, the mapping of the atomic excitation onto the atomic state is induced. Secondly, the final state of the atom is detected by performing a nondestructive measurement.

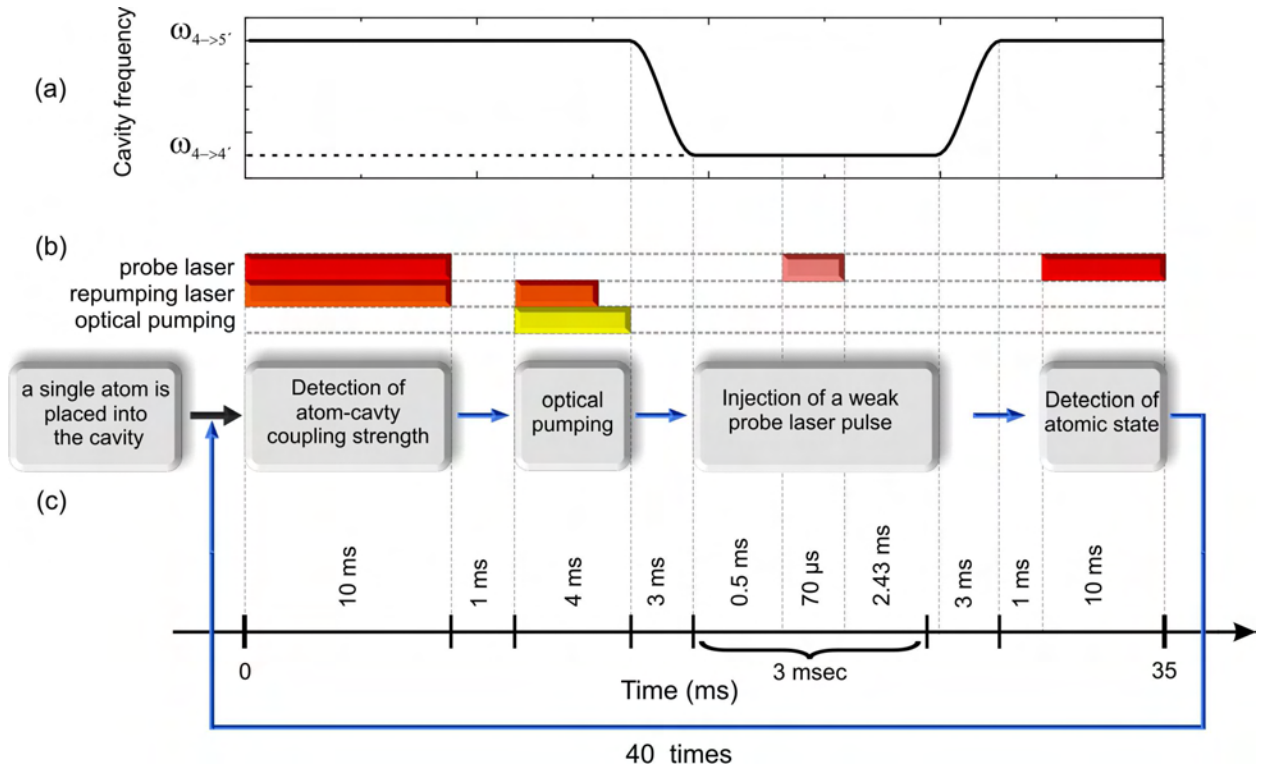


Figure 3.12: Normal-mode splitting measurement sequence. (a) The cavity resonance frequency and (b) the sequence of laser pulses as a function of time. (c) Flow diagram shows the succession of the experimental steps.

In order to map the atomic excitation on the atomic state, the cavity is tuned in resonance with the $F = 4 \rightarrow F' = 4$ transition. The excitation of coupled atom-cavity system is shared between the photonic excitation of the cavity field and the atomic excitation, i. e. the population of the $F' = 4$ state at this cavity frequency. From this state atom decays to either ground state with comparable probability. Therefore, the measurement of the final atomic state gives a direct indication of the population in $F' = 4$, i. e. the atomic excitation. In order to detect the atomic state we need to tune the cavity resonance close to the $F = 4 \rightarrow F' = 5$ transition, as discussed earlier in the Section 3.2.1. Therefore, the experimental procedure for the measurement of the normal-mode splitting involves the deterministic sweep of the cavity resonance.

The experiment starts by transporting a single atom into the center of the cavity mode. The order of the subsequent experimental steps, see Figure 3.12, is given below:

1. The presence of the atom is detected and the atom-field coupling strength is measured by observing the cavity transmission with its resonance frequency tuned about 44 MHz blue from the $F = 4 \rightarrow F' = 5$ transition. The coupling strength is extracted by averaging over 9 ms of the transmission signal.
2. In order to minimize the variation of the coupling strength during the map-

- ping of the normal-mode splitting, the atom is optically pumped into the outermost Zeeman sublevel $F = 4, m_F = 4$. For the corresponding π -transition $F = 4, m_F = 4 \rightarrow F' = 4, m_F = 4$ the expected maximum coupling strength equals 12 MHz.
3. In order to map the atomic excitation onto the atomic hyperfine state we first tune the cavity resonance about 10 MHz blue with respect to the $F = 4 \rightarrow F' = 4$ transition. The fast sweep of the cavity resonance stresses the cavity stabilization loop and can cause fluctuations of the cavity frequency, and thus fluctuations of the intra-cavity lock laser intensity. We therefore introduce an additional waiting interval of 0.5 ms duration, sufficient for the cavity frequency fluctuations to decay. Second, the probe laser pulse with a variable frequency around the cavity resonance is injected for $70 \mu\text{s}$ ³. It is linearly polarized along the quantization axis and therefore can induce π -transitions and excite the atom to the $F' = 4, m_F = 4$ state, from which it can decay to either ground state.
 4. In order to read out the final atomic spin state the cavity frequency is shifted back to its initial value, 44 MHz blue detuned from the $F = 4 \rightarrow F' = 5$ transition. The transmission of the resonant probe laser is monitored for 10 ms while the repumping laser is switched off. The atomic state is determined from the first 2 ms of the probe laser transmission.

In order to reduce the data acquisition time and suppress unwanted effects caused by the drifts of experimental parameters, the procedure listed above is performed repeatedly with each single atom. For a fixed number of repetitions the speed-up of the data acquisition is determined by the ratio between the preparation duration of a single atom inside the cavity field and the duration of subsequent experimental cycle. Whereas the total time required to place a single atom inside the cavity is on the order of 4 s, a single cycle to measure the normal-mode splitting as outlined above lasts only 35 ms. Therefore, the speed-up almost equals to the number of repetitions. The upper limit on this number, however, is determined by the survival of the atom during the experimental sequence. Thus, the number of repetitions is chosen as a tradeoff between achieving maximal speed-up and avoiding repetitions where the atom has already been lost, and equals to 40 for the current experiments.

3.3.2 Stability of the coupling strength

As discussed in Chapter 2, the atom-cavity coupling strength among other things depends on the relative position of the dipole trap along the z -axis with respect to the cavity mode, see Figure 2.5. We ensure maximum possible atom-cavity coupling by adjusting the dipole trap position in a preparatory experiment. Moreover, since the mapping of the normal-mode splitting and the read out of the atom-field coupling strength are performed

³To simplify the analysis of the data, the sequence duration has been kept constant. Since the duration of the probe laser pulse had to be adjusted during the experiment, we reserved the interval of 2.5 ms for its variation.

at different cavity frequencies, we have to verify the stability of the coupling strength with respect to the shift of the cavity resonance.

Controlling the coupling strength along the cavity axis

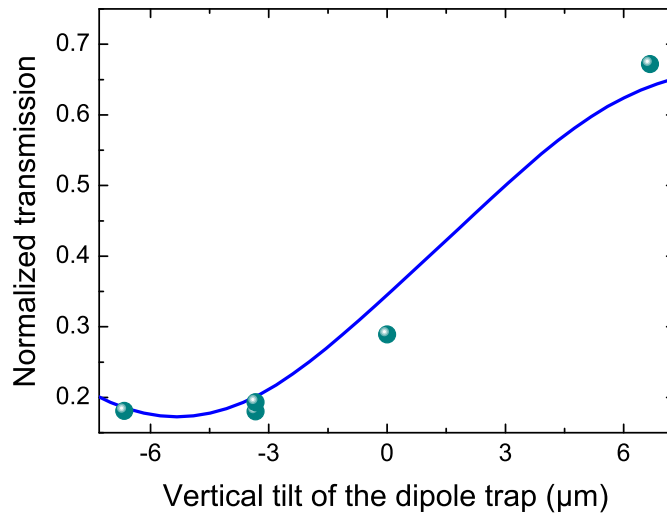


Figure 3.13: Scanning the atom cavity coupling strength along the cavity axis. The dots show the normalized cavity transmission as a function of displacement of the vertical dipole trap along the cavity axis. Each data point is averaged over 33 to 36 single atom experiments. The solid blue line is the result of a simple numerical model, taking into account the change in the transmission caused by the modulation of the difference in wavelengths between the lock and the probe laser standing waves.

In order to maximize the atom-cavity coupling strength along the z -axis, we shift the vertical position of the dipole trap by tilting its mirrors with PZTs, see Figure 1.10 in Chapter 1, and for each position observe the transmission of the cavity while coupling a single atom to the center of the cavity mode.

Figure 3.13 shows the transmission while atom resides inside the cavity, normalized to the empty cavity transmission, as a function of the vertical position of the dipole trap. Each point of the graph is averaged over 33 to 36 experiments with a single atom. As expected, we observe a strong variation of the coupling strength over the beat length of the lock and probe laser standing waves, as already anticipated in Figure 2.5. The solid blue line is the result of simple model of the change in the transmission signal caused by the modulation of g due to the spatial beating between the lock and probe laser standing waves.

In principle, by scanning the position over the range exceeding a single beat length, it should be possible to observe a periodic oscillation of the transmission signal. However,

this observation was not possible due to the limited range of the PZTs of the dipole trap mirrors.

Verification of the coupling strength stability

In our measurement of the normal-mode splitting the detection of the coupling strength and the mapping of the splitting are separated by intermediate steps, such as the sweep of the cavity resonance, optical pumping, and switching off the probe laser. Each of these steps could cause heating and thus a reduction of the coupling strength.

We have investigated this phenomenon in preparatory experiments, where we have monitored the transmission of the cavity after inserting an atom into the cavity center, and again after performing all the intermediate steps. By comparing the transmission levels the stability of the coupling strength is monitored.

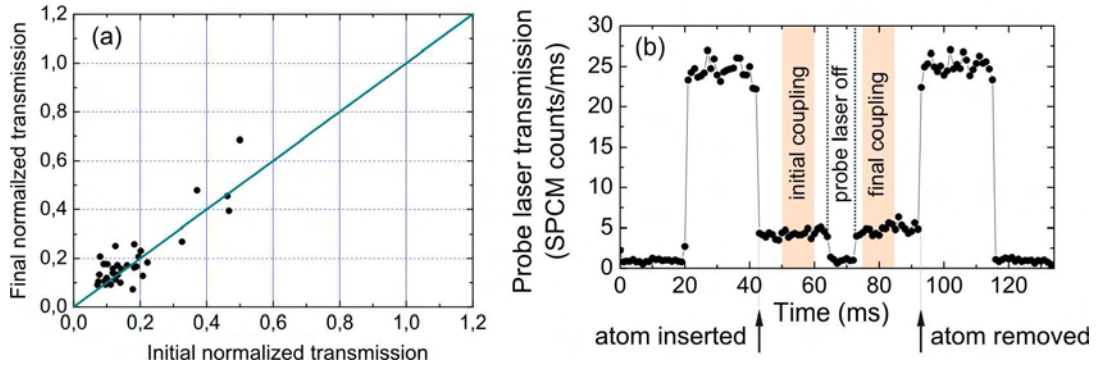


Figure 3.14: Coupling strength stability after switching off the probe laser. (a) The final normalized cavity transmission versus the initial transmission for the optimal vertical position of the dipole trap. (b) The transmission of the probe laser averaged over the traces, which are used for (a). The stripes represent the intervals over which the initial and final transmission are averaged.

Stability in absence of probe laser cooling In the first experiment we monitor the stability of the coupling strength in absence of the cooling action of the probe laser. As was discussed in References [25, 94], in absence of the probe laser an atom is exposed to the fluctuations of the intra-cavity lock laser standing-wave dipole trap, which may induce a parametric heating and delocalize the atom. In turn, this results in a decline of the effective coupling strength.

Although the measured lifetime of the atom inside the cavity in the absence of the probe laser is about 130 ms (see Figure 1.16 in Chapter 1), much larger than the interval in the experiment sequence of normal-mode splitting where the probe laser is off, we had to verify the stability of g in an independent experiment.

In this experiment we first place a single atom in the center of the cavity field and observe the cavity transmission for 20 ms (here denoted by initial transmission). Then the probe laser is switched off for the next 10 ms, as in the experimental sequence (see

Figure 3.12), followed by the second transmission observation for another 20 ms (final transmission). Figure 3.14 (a) shows the normalized averaged final transmission versus the normalized averaged initial transmission, each averaged over 10 ms interval as shown in Figure 3.14. The measurement is performed for the optimal position of the dipole trap along the z -axis, providing the maximum coupling strength. The transmission drops below 30% of the empty cavity transmission for the most of the cases and exhibits clear correlations.

Figure 3.14 (b) shows the transmission signal averaged over 35 experimental records, corresponding to the data in Figure 3.14 (a). The stripes represent the intervals over which the final and initial transmission are averaged. The average initial normalized transmission is 0.17, which is close the final normalized transmission of 0.19. Combining this with the observed correlation of the transmission signals, we have verified that the coupling strength changes only marginally in the absence of the probe laser cooling for 10 ms.

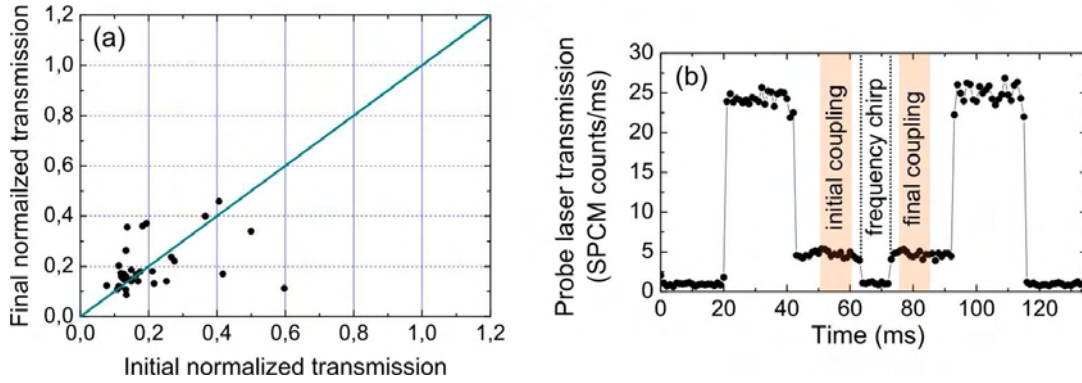


Figure 3.15: Stability of the coupling strength during the cavity frequency chirp. (a) The normalized cavity transmission after the frequency chirp of the cavity versus the normalized cavity transmission before the chirp. (b) The transmission of the probe laser averaged over the traces, which are used for (a). The stripes represent the intervals over which the initial and final transmission are averaged.

Stability with respect to the cavity frequency sweep The sweep of the cavity frequency from the $F = 4 \rightarrow F' = 5$ transition to the $F = 4 \rightarrow F' = 4$ transition within 3 ms corresponds to the sweeping rate of about 10^5 linewidths per second. Although this sweep is conducted adiabatically, i. e. by using a \sin^2 -like sweep form, it induces a significant strain on the cavity stabilization loop, which can cause fluctuations of the cavity resonance with respect to the lock laser frequency. Since the intra-cavity intensity of the lock laser depends on the match between its frequency and the cavity resonance, the relative frequency fluctuations would cause the intra-cavity lock laser intensity fluctuations. As discussed in the previous paragraph, this can cause the reduction of coupling strength g .

Figure 3.15 (a) shows the final cavity transmission versus initial transmission before and after a frequency chirp from the $F = 4 \rightarrow F' = 5$ transition frequency to the $F = 4 \rightarrow F' = 4$ transition and back. Remarkably, during this measurement we observe

a good correlation of the cavity transmission levels, indicating no significant change of the atomic position during the sweep of the cavity frequency. Figure 3.15 (b) shows the average over the transmission traces used for Figure 3.15 (a).

Variation of the atom-cavity coupling during a single experimental sequence

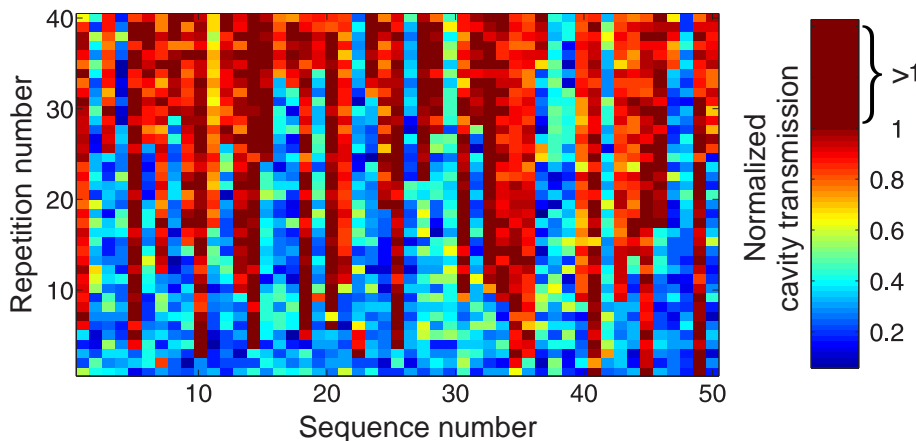


Figure 3.16: Dynamics of the coupling strength during the acquisition of a single data point of the normal-mode splitting. The color bar stands for the relative transmission (normalized to the empty cavity transmission) during the atom-field coupling strength detection stage. Blue areas indicate a large transmission drop. Red areas indicate the loss of the atom. Although for some experimental runs the atom survived all 40 repetitions, in most sequences it was lost by the end of the experimental run.

After completing these preparatory steps, it is important to retrieve the dynamics of the coupling strength during the execution of the entire experimental sequence of the normal-mode splitting measurement. In particular, at a certain stage of the sequence the probe laser is switched off and the detuning of the cavity frequency is performed at the same time. An additional possible distortion of the coupling strength is due to acoustic vibrations, caused by the shutters of the repumping lasers periodically switching on and off during the experimental procedure. These vibrations may affect the frequency stability of the probe laser, which is the first reference element of the cavity frequency stabilization servo loop.

We conduct the experiment according to the procedure, sketched in Figure 3.12. Figure 3.16 shows a typical distribution of the transmission acquired during the detection phase of the atom-cavity coupling, normalized to the empty cavity transmission. It shows 50 experimental sequences, each containing 40 repetitions of the experimental cycle. They were used to record a single point of the normal-mode splitting spectrum (see Section 3.3.3). For each data point of Figure 3.16 the transmission is averaged over 9 ms. The color bar goes from dark blue, denoting the transmission drop to zero, to red, where the transmission is the same as for the empty cavity. Whereas for some experimental runs the atom survived all 40 repetitions, in most of the cases the atom was lost by the end of a sequence.

Different transmission levels indicate the variation of the corresponding atom-cavity coupling strengths. Since our measurement of the normal-mode splitting is based on ensemble averaging, the splitting would be washed out when averaging over a broad range of coupling strength.

In order to circumvent the effect of this variation, for the evaluation only events where g exceeded certain value were post-selected. For this, we take into account only those events where the transmission dropped to below 30% of the empty cavity transmission before (initial transmission) and after (final transmission) performing the mapping of the normal-mode splitting. As each experimental run involves multiple repetitions of identical experimental cycles (see Section 4), the final transmission in each experimental cycle is the initial transmission of the next cycle.

Figure 3.17 (a) shows the final versus initial transmission for the data, presented in Figure 3.16. As in the preparatory experiments, a clear correlation of the transmission signals is also observed here. The data points with the normalized transmission exceeding 0.7 indicate the transmission of the empty cavity, i. e. the events where an atom was lost.

In order to quantitatively characterize the magnitude and the spread of the coupling strength during the entire measurement of the normal-mode splitting (see below), a histogram of the transmission signal during the coupling detection phase is constructed and shown in Figure 3.17 (b). Similarly to Figure 3.3 one sees two slightly overlapping peaks. However here, since the repumping laser is continuously switched on during the coupling strength detection phase, the right peak stands for empty cavity transmission and the left peak, as in Figure 3.3, is the distribution of the transmission during the atom-field coupling detection stage. The dashed green line is the result of a calculation taking into account the shot noise only and adjusted to the height of the corresponding peaks of the histogram. Notably, the right peak is considerably broader than the shot noise limit⁴. This is most probably caused by an imperfect setting of the cavity stabilization servo loop for this measurement. The broadening of the left peak is mainly caused by the variation of the coupling strength, originating from the variation of the insertion position along the cavity axis and the possible intracavity position dynamics of atoms, which is described in Chapter 2.

It is interesting to note that in contrast to the measurement, presented in Figure 3.14, here we observe a significantly smaller atom-cavity coupling strength, although the relevant experimental parameters were set the same. The possible explanation of this coupling deterioration is the sensitivity of the intracavity atomic temperature to the setting of the cavity servo loop. A higher atomic temperature leads to stronger delocalization, which reduces the effective coupling strength and therefore results in a higher average transmission signal.

3.3.3 Measurement of the normal-mode splitting via the atomic state

After showing all preparatory experimental procedures, here I will present the final result of the realization of the normal-mode splitting via the atomic state.

⁴Note that for this histogram, in contrast to that presented in Figure 3.3, the cavity transmission is averaged over 9 ms, resulting in a lower shot noise level.

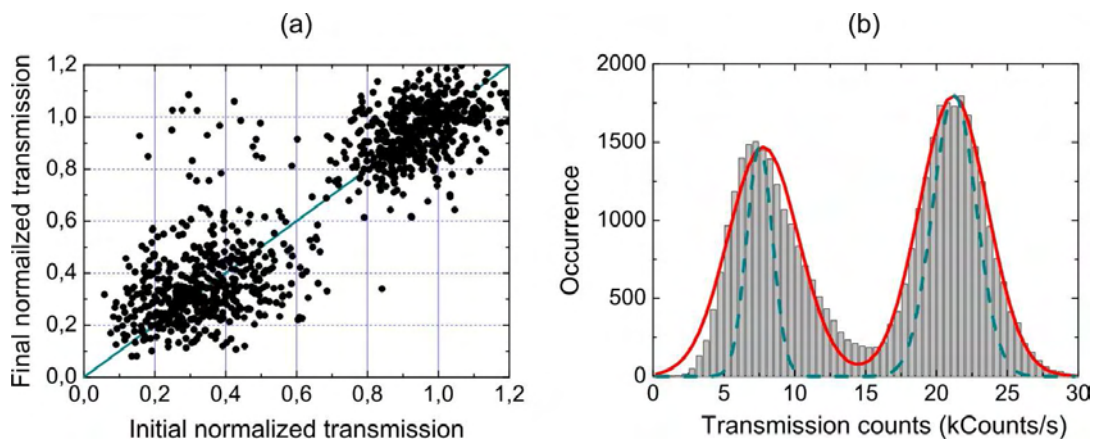


Figure 3.17: (a) The final normalized cavity transmission versus the initial normalized transmission for the data presented in Figure 3.16. Data points in the upper region (above 0.7) originate from those events where an atom was lost during the observation. (b) Histogram of the transmission signal during the coupling strength detection phase for all data points of the normal-mode splitting measurement. The two peaks are fitted with Gaussian functions (solid line): the left peak corresponds to the distribution of the transmission signal while an atom resides inside the cavity, while the right peak indicates the transmission distribution of the empty cavity. The dotted line shows the calculated distribution of the transmission signal taking into account the shot noise only.

Normal-mode splitting

Figure 3.18(a) shows the recorded final atomic population in the $F = 3$ state as a function of probe-cavity detuning during the experimental procedure described in Section 3.3.1. The double-peak structure of the recorded spectrum clearly manifests the interaction-induced normal-mode splitting. Each data point is obtained from 120 to 470 events. They are post-selected from the acquired data, considering only the events where g was within a definite range, see Section 3.3.2. The post-selected events correspond to 12% of the total number of recorded events, including those where atoms were lost.

The spectrum shows an asymmetry with the peak at positive $\omega_p - \omega_c$ being considerably higher and closer to the $\omega_p - \omega_c = 0$ line. This is in agreement with a theoretical calculation: Figure 3.18(b) shows the calculated atomic scattering rate⁵ as a function of $\omega_c - \omega_a$ and $\omega_p - \omega_c$.

The background of approximately 13% is caused by the erroneous detection of the atomic state during the 2 ms state detection time. This value is compatible with the probability of 18% of a quantum jump to occur during the detection interval, see Section 3.1.

Numerical Model

In order to analyze the process of this measurement, I have developed a simple model. In a first step, the atomic photon scattering rate as a function of the cavity-probe laser

⁵The details of the calculations are provided below.

detuning was estimated by numerically solving the master equation [65].

Using the obtained scattering rate a rate equation has been solved to model the non-linear population transfer to the $F = 3$ state during the $70 \mu\text{s}$ mapping pulse. For a rate equation a three-level system is assumed: the $F = 3$ and $F = 4$ ground states and the $F' = 4$ excited state. The population redistribution over Zeeman sublevels is neglected.

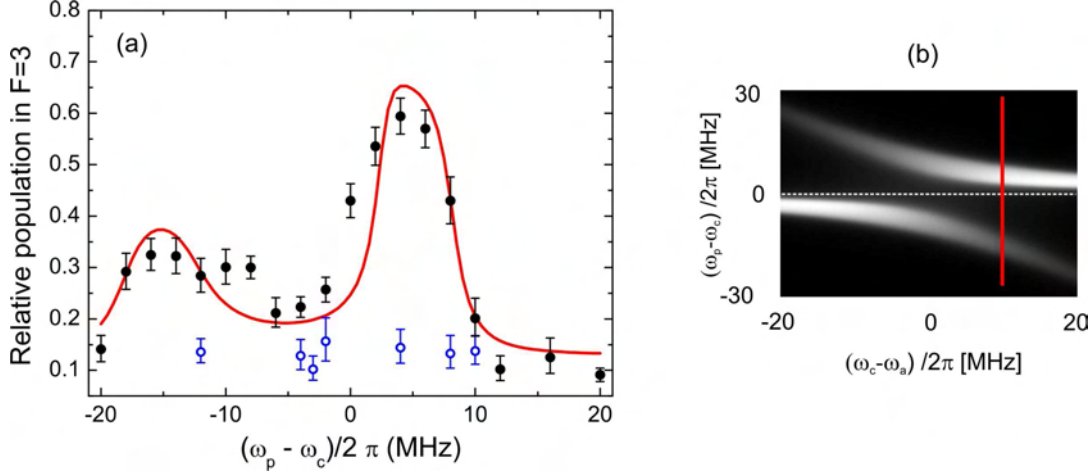


Figure 3.18: Normal-mode splitting. (a) Relative population in the $F = 3$ state as a function of probe-cavity detuning. Each data point (\bullet) is obtained from 120 to 470 experimental cycles. (\circ) Background, corresponding to the level of the erroneous detection of the atom in $F = 3$. The solid line indicates the result of the numerical model (see text). (b) The calculated atomic scattering rate for both dressed states.

Furthermore, the model assumes a homogeneous distribution of coupling strength of $g = 2\pi \times (6 \dots 12)$ MHz, which corresponds to the selected range of transmissions mentioned above. Here $g = 2\pi \times 12$ MHz belongs to a maximally coupled atom for the π -transition $F = 4, m_F = 4 \rightarrow F' = 4, m_{F'} = 4$. The two fit parameters are the cavity-atom detuning $\omega_c - \omega_{4,A'}$ and the intra-cavity photon number n_{ph} . Here $\omega_{4,A'}$ is the angular frequency of the AC-Stark shifted $F = 4 \rightarrow F' = 4$ transition. Fitting the model to the measured data yields $n_{\text{ph}} = 0.06$ and $\omega_c - \omega_{4,A'} = 2\pi \times 10$ MHz. An independent photon number measurement agrees with the fitted value and implies that we are in the weak excitation limit. The result of the calculation is presented as a solid line in Figure 3.18 and fits reasonably well to the measured data.

Figure 3.19 shows the calculated relative population in the $F = 3$ state as a function of number of scattering events. It is interesting to note that after scattering of less than two photons, on average 50% of the atomic population will be transferred to $F = 3$. This results in a negligible atomic heating of a few recoil photon energies, unlike in the experiments recording the normal-mode splitting by observing the leakage of photonic excitation from the cavity. There, an advanced cooling scheme had to be applied to compensate for the heating effects induced by the probe laser light at unfavorable probe-cavity detunings [51]. In our current experiment, the atomic temperature is limited by the equilibrium temperature during the detection phase of the coupling strength, i. e. given by probe laser

cooling. This step can be eliminated by preliminary cooling the atoms to their motional ground state. In this case, due to the much better localization of atoms, the spread of the atom-cavity coupling strength will be negligible. Thus, atoms ideally will couple to the cavity with maximal achievable coupling strength.

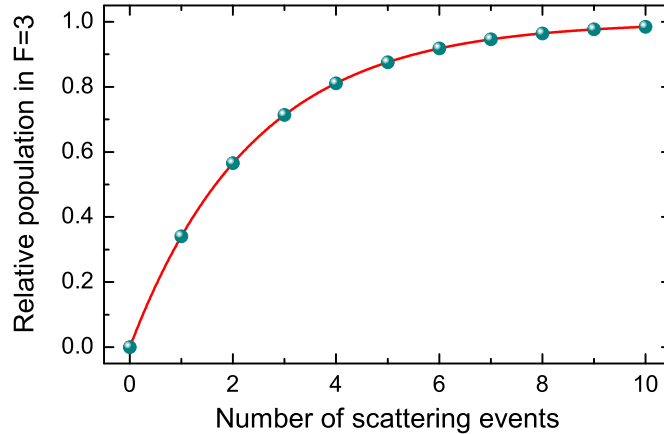


Figure 3.19: Calculated relative population of an atom in the $F = 3$ state, initially occupying the $F = 4$ state, as a function of number of scattering events from the probe laser tuned in resonance with the $F = 4 \rightarrow F = 4'$ transition. The solid line is the solution of the rate equation.

3.4 Conclusion

In this Chapter I have demonstrated a method to measure nondestructively the hyperfine ground state of a single atom, strongly coupled to the resonator field, via the cavity transmission. This measurement method formally fulfills the criteria of a projective QND measurement for the hyperfine state of a single atom. The imperfection of this method is that the measuring process changes the atomic state at a low rate. This could be suppressed by improving the efficiency of the cavity transmission detection.

Continuous measurement of the transmitted probe laser light while a single atom is inside the cavity field yields a random telegraph signal, originating from quantum jumps between the internal states of the atom. By means of second-order correlation functions, the dynamics of quantum jumps has been characterized from the recorded telegraph signals.

The excitation spectrum of a system consisting of a single atom, coherently and strongly interacting with the field of the resonator, was recorded for the first time via observation of the atomic state. The measurement was enabled by the nondestructive spin state measurement method, allowing a recycling of each atom placed in the cavity several tens times. This method constitutes an alternative to the commonly used approach, which is based

on the detection of photonic excitations and allows the measurement of the normal-mode splitting while inducing a negligible heating of atoms. Moreover, this method allows extensive applications, including the detection of the entangled or multi-atom correlated states in similar systems, where the detection of the final atomic state is an essential requirement.

To get one step closer to the ultimate goal of entanglement generation between two atoms, we have extended our experiment to the case of two atoms simultaneously coupled to the resonator field. Continuous observation of the cavity transmission yields the conditional dynamics of the spin states. Although for the current observations the spontaneous photon scattering was employed, the generation of entangled states requires the suppression of photon scattering. This can be achieved by operating in a deep dispersive regime, i. e. by detuning the cavity far from the atomic resonance. In this regime the outcome of the interaction between an atom and the cavity field can still be measured from the phase shift of the transmitted probe light [61, 85].

Summary and Outlook

In this thesis I have presented the realization and investigation of controlled and strongly interacting systems of one and two atoms in a cavity. With the progress we made, our systems approach the fulfillment of all five DiVincenzo requirements for quantum information processing.

Atom-cavity coupling

Since the dominance of the coherent atom-cavity coupling over the dissipation channels is the essential condition for future experiments in quantum information processing by cavity QED concepts, a part of this thesis has been dedicated to the characterization of atom-cavity coupling. For this purpose two different approaches have been used:

Transmission detection The detection of cavity transmission is used as standard method to quantify atom-cavity coupling in several groups worldwide [61, 62, 95]. Combining this method with our conveyor-belt technique we have controlled the coupling strength by deterministically placing an atom at a desired position inside the cavity mode.

Moreover, we have investigated the dependence of the coupling strength on the number of atoms, simultaneously placed inside the resonator mode. For this purpose we have intentionally placed one or two atoms at the edge of resonator mode, where the transmission signal is sensitive to the number of atoms. For two atoms placed inside the mode, we have observed an increase of g which fits well the prediction of our model.

Atomic state A different approach to extract information about atom-cavity coupling is based on the detection of the final atomic state. It is essential for the detection of atom-atom entangled and multi-atom correlated states, where quantum-state tomography has to be performed to infer the degree of correlation [96]. In the framework of this thesis, we have mapped a spectrum of the coupled single-atom-cavity system on to the atomic state, revealing the vacuum Rabi splitting and indicating that our system is in the strong coupling regime. In atom-cavity systems, this signature of a strong atom-field interaction has been observed in several other groups by recording the cavity transmission measurement, see References [79, 51]. However, so far its realization through the detection of the atomic state has been unexplored.

In the future, one could extend this experiment to two or more atoms, and measure the atom-number dependent normal-mode splitting for a well-defined number of atoms. The

limitation on the maximum number of atoms in our experiment originates from the finite size of the cavity mode and the resulting variation of g . Assuming that each lattice site of the DT is occupied by one atom each at a fixed position, and allowing 10% variation of g , the estimated maximum number of atoms is about 30.

Similar experiments have been performed by either using an atomic beam traversing the cavity mode [97], or atoms in a BEC coupled to the mode [98]. In these experiments, however, only the average number of atoms could be controlled.

Quantum jumps, conditional spin dynamics and its perspective

The observation of quantum jumps has been reported with different particles, such as single ions [73, 74, 75], electrons [77], molecules [76] and photons [71]. In this thesis, the first observation of quantum jumps between hyperfine states of single neutral atoms, strongly coupled to the cavity, has been observed by monitoring the cavity transmission. It allows us to detect continuously the spin state of the atom. Moreover, this method in principal fulfills the requirements of a projective quantum nondemolition measurement [81]. By extending this experiment to the case of two atoms, simultaneously coupled to the resonator field, we have observed conditional dynamics of their spin states, in agreement with the prediction of a simple parameter-free model.

Improving this measurement technique by suppressing photon scattering and increasing photon detection efficiency, it might become feasible to realize a weak quantum non-demolition measurement [85, 84] of the number of atoms in a certain spin state, which forms the basis of some probabilistic entanglement schemes [19].

In an alternative approach to generate entangled states, suggested in Reference [20], the system is brought into the desired state by unitary evolution, stimulated by carefully adjusted external fields. For ideal experimental conditions the estimated fidelity of such deterministic scheme is only 85%. In most deterministic schemes, the fidelity F scales as $1 - F \sim \sqrt{1/C_1}$. Therefore, the fidelity could be improved by increasing the cooperativity parameter $C_1 = g^2/(\kappa\Gamma)$. This could be done either by designing a resonator with a smaller mode volume or by suppressing κ .

Increasing the atom-cavity coupling

For all possible future applications, and in particular generation of entanglement states, it is essential to keep g stable and large, at the same time the fluctuation of g small. Our current observations have indicated a relatively high atomic temperature on the one hand, leading to a significant reduction of the average coupling strength, and an uncontrollable variation of g on the other hand.

The stability and the strength of the coupling could be improved by enforcing a better atomic localization. This could be achieved either by performing three-dimensional Raman side-band cooling to the motional ground state, in analogy to the experiment in Reference [86], or by modifying the geometry of the trapping potential such that it would provide a better confinement. In the latter case, for instance, one could superimpose our

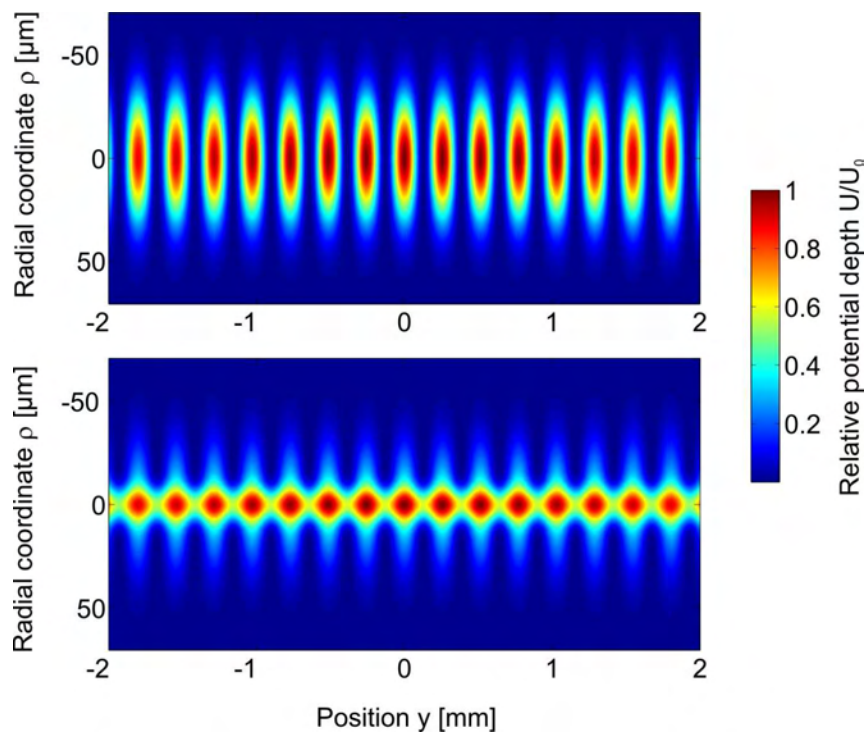


Figure 3.20: Simulated intensity distribution (in analogy to Figure 1.4) for the current standing-wave DT, (a). (b): The current standing wave DT superimposed with an additional running dipole trap DT, having a $1/e^2$ radius of $w_0 = 11 \mu\text{m}$ and a depth comparable to that of the standing wave DT. For illustrative purposes, the wavelengths of the standing wave DT and the running wave DT are stretched by a factor of 500.

current standing wave DT with an additional running wave DT with a smaller waist⁶. In this way, the localization of atoms will be improved in the direction transverse to the axis of DT, see Figure 3.20, reducing the variation range of g .

⁶The simulation with “OSLO” shows that the $1/e^2$ radius of $w_0 \approx 11 \mu\text{m}$ is attainable with commercial optical elements

Bibliography

- [1] D. Deutsch, *Quantum theory, the Church-Turing principle, and the universal quantum computer*, Proc. R. Soc. London **A400**, 97 (1985)
- [2] P. Shor, *Algorithms for quantum computation*, Proc. 35th IEEE FOCS 124 (1994)
- [3] P. Shor, *Polynomial-time algorithms for prime factorization and discrete logarithms on a quantum computer*, SIAM J. Comp. **26**, 1484 (1997)
- [4] L. Grover, *Quantum mechanics helps in searching for a needle in a haystack*, Phys. Rev. Lett. **97**, 325 (1997)
- [5] *QIPC, QUANTUM INFORMATION PROCESSING AND COMMUNICATION, Strategic report on current status, visions and goals for research in Europe, Version 1.4* (October 2007)
- [6] O. Mandel, M. Greiner, A. Widera, T. Rom, T. W. Hänsch, and I. Bloch, *Controlled collisions for multi-particle entanglement of optically trapped atoms*, Nature **425**, 937 (2003)
- [7] A. Gaëtan, Y. Miroshnychenko, T. Wilk, A. Chotia, M. Viteau, D. Comparat, P. Pillet, A. Browaeys, and P. Grangier, *Observation of collective excitation of two individual atoms in the Rydberg blockade regime*, Nature Phys. **5**, 115 (2009)
- [8] T. Pellizzari, S. A. Gardiner, J. I. Cirac, and P. Zoller, *Decoherence, continuous observation, and quantum computing: A cavity QED model*, Phys. Rev. Lett. **75**, 3788 (1995)
- [9] E. Hagley, X. Maître, G. Nogues, C. Wunderlich, M. Brune, J. M. Raimond, and S. Haroche, *Generation of Einstein-Podolsky-Rosen pairs of atoms*, Phys. Rev. Lett. **79**, 1 (1997)
- [10] A. Rauschenbeutel, G. Nogues, S. Osnaghi, P. Bertet, M. Brune, and S. Haroche, *Step-by-Step engineered multiparticle entanglement*, Science **288**, 2024 (2000)
- [11] S. Kuhr, W. Alt, D. Schrader, M. Müller, V. Gomer, and D. Meschede, *Deterministic delivery of a single atom*, Science **293**, 278 (2001)

- [12] I. Dotsenko, W. Alt, M. Khudaverdyan, S. Kuhr, D. Meschede, Y. Miroshnychenko, D. Schrader, and A. Rauschenbeutel, *Submicrometer position control of single trapped neutral atoms*, Phys. Rev. Lett. **95**, 033002 (2005)
- [13] G. S. Agarwal, *Vacuum-field Rabi splittings in microwave absorption by Rydberg atoms in a cavity*, Phys. Rev. Lett. **53**, 1732 (1984)
- [14] G. Raithel, C. Wagner, H. Walter, L. M. Narducci, and M. O. Scully, *Cavity quantum electrodynamics*, p. 57, Academic Press, New York (1994)
- [15] C. J. Hood, T. W. Lynn, A. C. Doherty, A. S. Parkins, and H. J. Kimble, *The atom-cavity microscope: Single atoms bound in orbit by single photons*, Science **287**, 1447 (2000)
- [16] H.-J. Briegel, W. Dür, J. I. Cirac, and P. Zoller, *Quantum repeaters: The role of imperfect local operations in quantum communication*, Phys. Rev. Lett. **81**, 5932 (1998)
- [17] D. Schrader, I. Dotsenko, M. Khudaverdyan, Y. Miroshnychenko, A. Rauschenbeutel, and D. Meschede, *Neutral atom quantum register*, Phys. Rev. Lett. **93**, 150501 (2004)
- [18] D. Schrader, *A neutral atom quantum register*, Ph.D. thesis, Universität Bonn (2004), available at http://hss.ulb.uni-bonn.de/diss_online/
- [19] A. S. Sørensen and K. Mølmer, *Measurement induced entanglement and quantum computation with atoms in optical cavities*, Phys. Rev. Lett. **91**, 097905 (2003)
- [20] L. You, X. X. Yi, and X. H. Su, *Quantum logic between atoms inside a high-Q optical cavity*, Phys. Rev. A **67**, 032308 (2003)
- [21] S.-B. Zheng and G.-C. Guo, *Efficient scheme for two-atom entanglement and quantum information processing in cavity QED*, Phys. Rev. Lett. **85**, 2392 (2000)
- [22] D. P. DiVincenzo, *The physical implementation of quantum computation*, Fortschr. Phys. **48**, 771 (2000)
- [23] W. Alt, *Optical control of single neutral atoms*, Ph.D. thesis, Universität Bonn (2004), available at http://hss.ulb.uni-bonn.de/diss_online/
- [24] S. Kuhr, *A controlled quantum system of individual neutral atoms*, Ph.D. thesis, Universität Bonn (2003), available at http://hss.ulb.uni-bonn.de/diss_online/
- [25] I. Donsenko, *Single atoms on demand for cavity QED experiments*, Ph.D. thesis, Universität Bonn (2007), available at http://hss.ulb.uni-bonn.de/diss_online/
- [26] E. L. Raab, M. Prentiss, A. Cable, S. Chu, and D. E. Pritchard, *Trapping of neutral sodium atoms with radiation pressure*, Phys. Rev. Lett. **59**, 2631 (1987)
- [27] H. J. Metcalf and P. van der Straten, *Laser cooling and trapping*, Springer (1999)

- [28] V. I. Balykin, V. G. Minogin, and V. S. Letokhov, *Electromagnetic trapping of cold atoms*, Rep. Prog. Phys. **63**, 1429 (2000)
- [29] V. G. Minogin Letokhov, V. S. and B. D. Pavlik, *Cooling and capture of atoms and molecules by a resonant light*, Sov. phys. JETP **45**, 698 (1977)
- [30] D. Wineland and W. Itano, *Laser cooling of atoms*, Phys. Rev. A **20**, 1521 (1979)
- [31] R. J. Cook, *Quantum-mechanical fluctuations of the resonance-radiation force*, Phys. Rev. A **44**, 967 (1980)
- [32] D. Haubrich, A. Höpe, and D. Meschede, *A simple model for optical capture of atoms in strong magnetic quadrupole fields*, Opt. Comm. **102**, 225 (1993)
- [33] C. Wieman and T. W. Hänsch, *Doppler-free laser polarization spectroscopy*, Phys. Rev. Lett. **36**, 1170 (1976)
- [34] R. Grimm, M. Weidemüller, and Y. B. Ovchinnikov, *Optical dipole traps for neutral atoms*, Adv. At. Mol. Opt. Phys. **42**, 95 (2000)
- [35] C. Cohen-Tannoudji, J. Dupont-Roc, and G. Grynberg, *Atom-photon interactions: Basic processes and applications*, Wiley, New York (1992)
- [36] G. A. Askaryan, *Effect of gradient of high-power electromagnetic field on electrons and atoms*, Sov. Phys. JETP **15**, 1088 (1962)
- [37] V. S. Letokhov, Pis. Zh. Eksp. Teor. Fiz. **7**, 348 (1968), engl. translation JETP Lett. **7**, 272
- [38] S. Chu, J. E. Bjorkholm, A. Ashkin, and A. Cable, *Experimental observation of optically trapped atoms*, Phys. Rev. Lett. **57**, 314 (1986)
- [39] N. Davidson, H. Jin Lee, C. S. Adams, M. Kasevich, and S. Chu, *Long atomic coherence times in an optical dipole trap*, Phys. Rev. Lett. **74**, 1311 (1995)
- [40] K.H. Yang, S.W. Stwalley, S. P. Heneghan, J. T. Bahns, and K. K. Wang T. R. Hess, *Examination of effects of TEM01-mode laser radiation in the trapping of neutral potassium atoms*, Phys. Rev. A **34**, 2962 (1986)
- [41] L. Allen N. B. Simpson, K. Dholakia and M. J. Padgett, *Mechanical equivalence of spin and orbital angular momentum of light: An optical spanner*, Opt. Lett. **22**, 52 (1997)
- [42] G. Agrawal, *Nonlinear Fiber Optics*, Academic Press (2001)
- [43] R.F. Guan, F.L. Zhu, Z.Y. Gan, D.X. Huang, and S. Liu, *Stress birefringence analysis of polarization maintaining optical fibers*, Opt. Fiber Technol. **11**, 240 (2005)
- [44] N. Caponio and C. Svelto, *A simple angular alignment technique for a polarization-maintaining-fiber*, IEEE Photonics Technol. Lett. **6**, 728 (1994)

-
- [45] D. W. Allan, *Statistics of atomic frequency standards*, Proc. IEEE **54**, 221 (1966)
- [46] Y. Miroshnychenko, W. Alt, I. Dotsenko, L. Förster, M. Khudaverdyan, D. Meschede, D. Schrader, and A. Rauschenbeutel, *Quantum engineering: An atom-sorting machine*, Nature **442**, 151 (2006)
- [47] Y. Miroshnychenko, W. Alt, I. Dotsenko, L. Förster, M. Khudaverdyan, D. Meschede, S. Reick, and A. Rauschenbeutel, *Inserting two atoms into a single optical micropotential*, Phys. Rev. Lett. **97**, 243003 (2006)
- [48] W. Alt, *An objective lens for efficient fluorescence detection of single atoms*, Optik **113**, 142 (2002)
- [49] L. Förster, W. Alt, I. Dotsenko, M. Khudaverdyan, D. Meschede, Y. Miroshnychenko, S. Reick, and A. Rauschenbeutel, *Number-triggered loading and collisional redistribution of neutral atoms in a standing wave dipole trap*, New J. Phys. **8**, 259 (2006)
- [50] M. Khudaverdyan, *Addressing of individual atoms in an optical dipole trap*, Master's thesis, Universität Bonn (2003)
- [51] A. Boca, R. Miller, K. M. Birnbaum, A. D. Boozer, J. McKeever, and H. J. Kimble, *Observation of the vacuum Rabi spectrum for one trapped atom*, Phys. Rev. Lett. **93**, 233603 (2004)
- [52] M. Brune, E. Hagley, J. Dreyer, X. Maître, A. Maali, C. Wunderlich, J. M. Raimond, and S. Haroche, *Observing the progressive decoherence of the "meter" in a quantum measurement*, Phys. Rev. Lett. **77**, 4887 (1996)
- [53] C. J. Hood, *Real-time measurement and trapping of single atoms by single photons*, Ph.D. thesis, California Institute of Technology, CA (2000)
- [54] C. J. Hood, H. J. Kimble, and J. Ye, *Characterization of high-finesse mirrors: Loss, phase shifts, and mode structure in an optical cavity*, Phys. Rev. A **64**, 33804 (2001)
- [55] W. Rosenfeld, *A high finesse optical resonator for cavity QED experiments*, Master's thesis, Universität Bonn (2003)
- [56] H. Mabuchi, J. Ye, and H. J. Kimble, *Full observation of single-atom dynamics in cavity QED*, Appl. Phys. B **68**, 1095 (1999)
- [57] R. Drever and J. Hall, *Laser phase and frequency stabilization using an optical resonator*, Appl. Phys. B **31**, 97 (1983)
- [58] D. Meschede, H. Walther, and G. Müller, *One-atom maser*, Phys. Rev. Lett. **54**, 551 (1985)
- [59] G. Rempe, R. J. Thompson, and H. J. Kimble, *Cavity quantum electrodynamics with strong coupling in the optical domain*, Phys. Scr. **67** (1994)

- [60] S. Nußmann, M. Hijlkema, B. Weber, F. Rohde, G. Rempe, and A. Kuhn, *Submicron positioning of single atoms in a microcavity*, Phys. Rev. Lett. **95**, 173602 (2005)
- [61] J. McKeever, J. R. Buck, A. D. Boozer, and H. J. Kimble, *Determination of the number of atoms trapped in an optical cavity*, Phys. Rev. Lett. **93**, 143601 (2004)
- [62] T. Puppe, I. Schuster, A. Grothe, A. Kubanek, K. Murr, P. W. H. Pinkse, and G. Rempe, *Trapping and observing single atoms in a blue-detuned intracavity dipole trap*, Phys. Rev. Lett. **99**, 013002 (2007)
- [63] K. M. Fortier, S. Y. Kim, J. G. Michael, A. Peyman, and M. S. Chapman, *Deterministic loading of individual atoms to a high-finesse optical cavity*, Phys. Rev. Lett. **98**, 233601 (2007)
- [64] M. Khudaverdyan, W. Alt, I. Dotsenko, T. Kampschulte, K. Lenhard, A. Rauschenbeutel, S. Reick, K. Schörner, A. Widera, and D. Meschede, *Controlled insertion and retrieval of atoms coupled to a high-finesse optical resonator*, New J. Phys. **10**, 073023 (2008)
- [65] H. Carmichael, *An open systems approach to quantum optics*, Springer, Berlin (1993)
- [66] Segio M. Dutra, *Cavity quantum electrodynamics. The strange theory of light in a box*, Wiley, J (2005)
- [67] E. T. Jaynes and F. W. Cummings, *Comparison of Quantum and Semiclassical Radiation Theory with Application to the Beam Maser*, Proc. IEEE **51**, 89 (1963)
- [68] Peter Domokos and Helmut Ritsch, *Mechanical effects of light in optical resonators*, J. Opt. Soc. Am. B **20**, 1098 (2003)
- [69] M. Brune, P. Nussenzveig, F. Schmidt-Kaler, F. Bernardot, A. Maali, J. M. Raimond, and S. Haroche, *From Lamb shift to light shifts: Vacuum and subphoton cavity fields measured by atomic phase sensitive detection*, Phys. Rev. Lett. **72**, 3339 (1994)
- [70] J. K. Asbóth, P. Domokos, H. Ritsch, and A. Vukics, *Self-organization of atoms in a cavity field: Threshold, bistability, and scaling laws*, Phys. Rev. A **72**, 053417 (2005)
- [71] S. Gleyzes, S. Kuhr, C. Guerlin, J. Bernu, S. Deléglise, U. Busk Hoff, M. Brune, J.-M. Raimond, and S. Haroche, *Quantum jumps of light recording the birth and death of a photon in a cavity*, Nature **446**, 297 (2007)
- [72] S. Kuhr, W. Alt, D. Schrader, I. Dotsenko, Y. Miroshnychenko, W. Rosenfeld, M. Khudaverdyan, V. Gomer, A. Rauschenbeutel, and D. Meschede, *Coherence properties and quantum state transportation in an optical conveyor belt*, Phys. Rev. Lett. **91**, 213002 (2003)
- [73] J. C. Bergquist, R. G. Hulet, W. M. Itano, and D. J. Wineland, *Observation of quantum jumps in a single atom*, Phys. Rev. Lett. **57**, 1699 (1986)

- [74] W. Nagourney, J. Sandberg, and H. Dehmelt, *Shelved optical electron amplifier: Observation of quantum jumps*, Phys. Rev. Lett. **56**, 2797 (1986)
- [75] T. Sauter, W. Neuhauser, R. Blatt, and P. E. Toschek, *Observation of quantum jumps*, Phys. Rev. Lett. **57**, 1696 (1986)
- [76] T. Basche, S. Kummer, and C. Brauchle, *Direct spectroscopic observation of quantum jumps of a single molecule*, Nature **373**, 132 (1995)
- [77] S. Peil and G. Gabrielse, *Observing the quantum limit of an electron cyclotron: QND measurements of quantum jumps between fock states*, Phys. Rev. Lett. **83**, 1287 (1999)
- [78] C. Guerlin, J. Bernu, S. Deléglise, C. Sayrin, S. Gleyzes, S. Kuhr, M. Brune, J.-M. Raimond, and S. Haroche, *Progressive field-state collapse and quantum non-demolition photon counting*, Nature **448**, 889 (2007)
- [79] P. Maunz, T. Puppe, I. Schuster, N. Syassen, P. W. H. Pinkse, and G. Rempe, *Normal-mode spectroscopy of a single-bound-atom-cavity system*, Phys. Rev. Lett. **94**, 033002 (2005)
- [80] V. B. Braginsky, Y. I. Vorontsov, and K. S. Thorne, *Quantum nondemolition measurements*, Science **209**, 547 (1980)
- [81] A. Lupascu, S. Saito, T. Picot, P. C. de Groot, C. J. P. M. Harmans, and J. E. Mooij, *Quantum non-demolition measurement of a superconducting two-level system*, Nature Phys. **3**, 119 (2007)
- [82] G. J. Milburn and D. F. Walls, *Quantum nondemolition measurements via quadratic coupling*, Phys. Rev. A **28**, 2065 (1983)
- [83] N. Imoto, H. A. Haus, and Y. Yamamoto, *Quantum nondemolition measurement of the photon number via the optical Kerr effect*, Phys. Rev. A **32**, 2287 (1985)
- [84] S. Chaudhury, G. A. Smith, K. Schulz, and P. S. Jessen, *Continuous nondemolition measurement of the Cs clock transition pseudospin* (2006)
- [85] P. J. Windpassinger, D. Oblak, P. G. Petrov, M. Kubasik, M. Saffman, C. L. Garrido Alzar, J. Appel, J. H. Muller, N. Kjaergaard, and E. S. Polzik, *Nondestructive probing of Rabi oscillations on the cesium clock transition near the standard quantum limit*, Phys. Rev. Lett. **100**, 103601 (2008)
- [86] A. D. Boozer, A. Boca, R. Miller, T. E. Northup, and H. J. Kimble, *Cooling to the ground state of axial motion for one atom strongly coupled to an optical cavity*, Phys. Rev. Lett. **97**, 083602 (2006)
- [87] R. Loudon, *The quantum theory of light*, Clarendon, Oxford (1983)
- [88] R. J. Cook and H. J. Kimble, *Possibility of direct observation of quantum jumps*, Phys. Rev. Lett. **54**, 1023 (1985)

- [89] H. Yokoyama, K. Nishi, T. Anan, H. Yamada, S. D. Brorson, and E. P. Ippen, *Enhanced spontaneous emission from GaAs quantum wells in monolithic microcavities*, Appl. Phys. Lett. **57**, 2814 (1990)
- [90] J. M. Gérard, B. Sermage, B. Gayral, B. Legrand, E. Costard, and V. Thierry-Mieg, *Enhanced spontaneous emission by quantum boxes in a monolithic optical microcavity*, Phys. Rev. Lett. **81**, 1110 (1998)
- [91] A. A. Houck, J. A. Schreier, B. R. Johnson, J. M. Chow, Jens Koch, J. M. Gambetta, D. I. Schuster, L. Frunzio, M. H. Devoret, S. M. Girvin, and R. J. Schoelkopf, *Controlling the spontaneous emission of a superconducting transmon qubit*, Phys. Rev. Lett. **101**, 080502 (2008)
- [92] C. Weisbuch, M. Nishioka, A. Ishikawa, and Y. Arakawa, *Observation of the coupled exciton-photon mode splitting in a semiconductor quantum microcavity*, Phys. Rev. Lett. **69**, 3314 (1992)
- [93] A. Wallraff, D. I. Schuster, A. Blais, L. Frunzio, R.-S. Huang, J. Majer, S. Kumar, S. M. Girvin, and R. J. Schoelkopf, *Strong coupling of a single photon to a superconducting qubit using circuit quantum electrodynamics*, Nature **431**, 162 (2004)
- [94] A. Stiebeiner, *Deterministische Kopplung eines einzelnen Atoms an die Mode eines Resonators hoher Finesse*, Master's thesis, Universität Bonn (2007)
- [95] M. Trupke, J. Goldwin, B. Darquie, G. Dutier, S. Eriksson, J. Ashmore, and E. A. Hinds, *Atom detection and photon production in a scalable, open, optical microcavity*, Phys. Rev. Lett. **99**, 063601 (2007)
- [96] C. F. Roos, G. P. T. Lancaster, M. Riebe, H. Häffner, W. Hänsel, S. Gulde, C. Becher, J. Eschner, F. Schmidt-Kaler, and R. Blatt, *Bell states of atoms with ultralong lifetimes and their tomographic state analysis*, Phys. Rev. Lett. **92**, 220402 (2004)
- [97] R. J. Thompson, G. Rempe, and H. J. Kimble, *Observation of normal-mode splitting for an atom in an optical cavity*, Phys. Rev. Lett. **68**, 1132 (1992)
- [98] F. Brennecke, T. Donner, S. Ritter, T. Bourdel, M. Kohl, and T. Esslinger, *Cavity QED with a Bose-Einstein condensate*, Nature **450**, 268 (2007)

Acknowledgements

An dieser Stelle möchte ich mich bei all denen, die mich während meiner Dissertation unterstützt haben, bedanken.

Herrn Meschede verdanke ich die Möglichkeit, überhaupt an einem so faszinierenden und anspruchsvollen Experiment mit voller Entscheidungsfreiheit forschen zu dürfen. Herrn Weitz möchte ich für die Übernahme des Zweitgutachtens danken.

Von der “alten” Generation der Doktoranden, Dominik Schrader, Yevhen Miroshnychenko und Igor Dotsenko, habe ich die Fundamente des “erfolgreichen Forschens” gelernt. Igor hat sich in der Charakterisierung des Resonators engagiert, seine Zusammenarbeit mit REO hat uns einen Resonator bester Finesse beschert. Mein spezieller Dank geht an Dominik für die Etablierung des Team-Geistes in unserem Experiment. Außerdem hat er uns dank seiner kulinarischen Vorlieben des öfteren vor der Mensa bewart. Mit Yevhen Miroshnychenko hatte ich sowohl im Labor als auch außerhalb jede Menge Spaß.

Der neuen Generation der Doktoranden, Sebastian Reick und Tobias Kampschulte, möchte ich für vielseitige Unterstützung danken. Sebastian Reick, das Organisationstalent, sorgte für Ordnung in unserer Experimentenplanung. Jedes Softwareproblem hat Sebastian prompt gemeistert. Tobias Kampschulte experimentierte unermüdlich an neuen Ansätzen zur Verbesserung der Elektronik des Resonatorstabilisierungsregelkreises und war der Ruhende Pol in selbst den stressigsten Situationen. Die Diplomanten Karim Lenhard, Karsten Schöner, und Alexander Thobe haben sich enthusiastisch in unserem Experiment engagiert.

Von unseren Postdocs Dr. Artur Widera und Dr. Wolfgang Alt habe ich in zahlreichen ergiebigen Diskussionen gelernt, physikalische Phänomene mit anderen Augen zu betrachten – sei es durch Arturs motivierenden Optimismus, der mich Alternativen in Betracht zu ziehen lehrte, oder das überirdische Gespür und Vorschläge zur Lösung von beliebigen technischen Problemen durch Wolfgang: Unter anderem hätte der FP-Versuch “Nuclear magnetic resonance” ohne seine Unterstützung nie repariert werden können. Dr. Arno Rauschenbeutel habe ich in früheren Stadien meiner Arbeit für viel Inspiration und kritischen Blick auf bevorstehende Probleme zu danken.

Ich möchte mich ganz herzlich bei jenen bedanken, die an der Korrektur meiner Arbeit mitgewirkt haben.

Die freundliche Unterstützung vom dritten Stock des IAP hat meine Arbeit wesentlich erleichtert. Dafür möchte ich mich bei Annelise Miglo, Fien Latumahina und Ilona Jaschke bedanken. Dietmar Haubrich, abgesehen von unzähligen Briefen an sämtliche Behörden, die er für mich erstellt musste, hat beim Einbau des Resonators in unsere Vakuumapparatur

mit seinem wertvollen Rat die Caesium-Oxidierung vermeiden geholfen.

Die Mechanikwerkstatt hat uns durch Bearbeitung all unserer eiligen Bitten den Rücken freigehalten: Insbesondere möchte ich mich bei Herrn Langen und Herrn Graf bedanken. Ebenso hilfsbereit war der Elektronikwerkstatt – Herr Krause, Herr Hoffmann, Herr Brähler, Herr Korte und Herr Kalb.

An die AG Meschede von heute und vor fünf Jahren, die viel zu groß ist um niemanden zu vergessen, geht mein großes Dankeschön für die spannende tolle Zeit in all diesen Jahren. Meinen Büro-Nachbarn Michael Haas und Michal Karski verdanke ich die Umwandlung unseres Büros in das unterhaltsamste des IAP.

Vielen Dank an alle Mitglieder des IAP für die freundliche Atmosphäre.

Schließlich möchte den Menschen danken, die mich außerhalb des wissenschaftlichen Bereichs in anderen, mindestens genau so wichtigen Seiten des Lebens selbst aus großer Entfernung motiviert haben.

Я хочу поблагодарить моих родителей, Олю и Ашота, за их разностороннюю поддержку и оптимизм, даже в самых тяжёлых ситуациях. Мои сёстры, Женя и Карина, своей жизнерадостью вдохновляли меня и способствовали моему положительному отношению к происходящему.

Meiner Freundin Diemut danke ich für ihre nette Unterstützung und grenzenlose Geduld, vor allem gegen Ende der Dissertation.